Stability Analysis of VSCs Connected to an AC Grid

Thesis submitted to

Cardiff University

For the degree of

Doctor of Philosophy

2021

Xiangyu Li

School of Engineering

To my family

Contents

Acknowledgement

The completion of this research work would have not been possible without the guidance and assistance of many kind people.

First and foremost, I would like to express my sincere gratitude to my brilliant supervisor Prof. Jun Liang for his continuous technical guidance throughout my PhD study. I would also like to thank Dr. Carlos E. Ugalde-Loo for his wise advice and support. I will remember the valuable instructions I obtained from them beyond the research.

I would like to thank my parents for their encouragement and unconditional support throughout my life.

I would like to thank Dr. Gen Li and Dr. Chuanyue Li for their help in the past years and his kind assistance on revising the writing of my PhD thesis.

I would like to thank Prof. Luis Sainz Sapera and Dr. Lluis Monjo Mur for their help in the modelling work.

I would like to thank Dr. Guanglu Wu from China Electric Power Research Institute, and Dr. Ren Li from North China Electric Power University for their help collaborations in my research work.

I would also like to thank all my colleagues and friends at Cardiff University. Especially to Dr. Rui Zheng, Dr. Sheng Wang and Dr. Tibin Joseph for all the motivation and inspiration.

Last but not least, I would like to acknowledge the financial support from the project of North China Electric Power University, which provided me the golden opportunity to explore and develop my career with valuable industry training and a variety of activities

Abstract

As a typical renewable energy resource, wind power has been extensively exploited in the past years. With the continuous growth of wind power installed capacity, power electronic devices are widely used due to their good control performances. However, the interaction between power electronic devices and the power grid will lead to power system stability problems. Subsynchronous interaction (SSI) between wind farms and AC grids, as one of the most severe power system stability problems, has aroused great concerns. Different from the SSI between wind turbine generator (WTG) controllers and fixed series compensation or between generators and high voltage direct current (HVDC) controllers, recently, a new type of SSI is detected which is caused by the interactions between power electronic devices of WTGs and weak AC grid. The work in this thesis focuses on the mechanism and characteristics of this new type of SSI.

A simplified system model with permanent magnet synchronous motors (PMSGs) connected to weak AC grids is established to investigate the new SSI. The linear impedance model of the studied system is conducted. The correctness of the proposed impedance model is validated by the comparison between the analysis in MATLAB and time-domain simulations in PSCAD/EMTDC.

In the model of a single VSC connected to an AC grid, the mechanism of the SSI is investigated. The characteristics of the studied system under various conditions are analysed. The effects on system stability of different factors have been studied including the number of connected WTGs line reactance, Phase-locked loop (PLL), feed-forward voltage low-pass filter, current loop and outer loop of the VSCs. Time-domain simulation results verify the correctness of the analysis.

An equivalent model of multiple VSCs connected to an AC grid is presented to investigate the characteristics when VSCs with different control systems and control parameters are connected to an AC grid. A new approach based on the Generalised Nyquist Criterion (GNC) is proposed to analyse the system stability. Compared to the existing traditional criteria, the new criterion has the advantages of better accuracy and simplicity. The new approach is validated in time-domain simulation.

The study of this research work contributes to the stability analysis of power systems in the subsynchronous frequency range.

Nomenclature

Acronyms

A	Ampere
AC	Alternating current
BF	Blocking filter
DFIG	Doubly fed induction generator
FACTS	Flexible AC transmission system
GNC	Generalised Nyquist criterion
GTSDC	Generator terminal subsynchronous damping controller
H	Henry
HVDC	High voltage direct current
IGE	Induction generator effect
kA	Kiloampere
kV	Kilovolt
kW	Kilowatt
kVA	Kilovolt ampere
PCC	Point of common coupling
PLL	Phase-locked loop
PMSG	Permanent magnet synchronous motor
PSS	Power system stabiliser
p.u.	Per-unit value
mF	Millifarad
mH	Millihenry
MW	Megawatt
MVA	Megavolt ampere
SCR	Short circuit ratio
SE	Self-excitation
SEDC	Supplementary excitation damping controller
SG	Synchronous generator
SSCI	Subsynchronous control interaction
SSDC	Subsynchronous damping controller

SSI	Subsynchronous interaction
SSR	Subsynchronous resonance
SSSC	Static synchronous series compensator
SSTI	Subsynchronous torsional interaction
SVC	Static var compensator
STATCOM	Static synchronous compensator
TA	Transient torque amplification
TCSC	Thyristor controlled series compensator
TI	Torsional vibration interaction
V	Volt
VSC	Voltage source converter
W	Watt
WTG	Wind turbine generator
WPP	Wind Power Plant
Ω	Ohm
μF	Microfarad
μH	Microhenry

Symbols

Δ	The small deviation at the initial operating point
θ_s	The angle of AC transmission newtwork voltage
θ_g	The angle of infinite grid
θ_{pll}	The angle of PLL
σ	Real-part of eigenvalue
ω	Frequency in rad/s
ω_b	Base frequency of the system
ω_{cc}	Bandwidth of current loop of VSC
ω_{dc}	Bandwidth of outer loop of VSC
ω_{pll}	Bandwidth of PLL of VSC
ω_{Hf}	Bandwidth of feed-forward voltage low-pass filter

i_{cd}, i_{cq}	The instantaneous current in the *d*-axis and *q*-axis of VSC
i_{cdr}, i_{cqr}	Reference value of current in the *d*-axis and *q*-axis of VSC
i_{sd}, i_{sq}	The instantaneous current in the *d*-axis and *q*-axis of AC grid
k_{p_cc}, k_{i_cc}	Proportional and integral term of P-I controller of the current loop
k_{p_dc}, k_{i_dc}	Proportional and integral term of P-I controller of the outer loop
k_{p_dc}, k_{i_dc}	Proportional and integral term of P-I controller of PLL
P_g	The grid power
P_{WTG}	The output power of the wind farm
$P_{WTG, rated}$	Rated output power of the wind farm in the base case
R_f, L_f	Resistance and reactance of VSC filter
v_{sd}, v_{sq}	The instantaneous voltage in the *d*-axis and *q*-axis at PCC
v_{cd}, v_{cq}	Output voltage in the *d*-axis and *q*-axis of outer loop of VSC
v_g	The instantaneous voltage of the infinite grid

Chapter 1

Introduction

1.1 Background

Subsynchronous resonance (SSR) is one of the power system stability problems.

The occurrence of the instability phenomenon can be followed back to the 1930s. When the generator is connected to a capacitive load, the terminal voltage rises continuously and is out of control which is a self-excitation problem. Under asynchronous conditions, it is also known as the induction generator effect (IGE), which only involves electrical system resonance [1]-[2]. In the 1970s, with the applications of series compensation transmission line, the torsional vibration interaction (TI) phenomenon appeared when large capacity thermal power was transmitted by series compensation transmission. Two serious torsional vibration accidents occurred in the Mohave power plant in the United States in December 1970 and October 1971, resulted in the damage of the generator shaft [3]. After that, it was found that the strong torsional vibration in the transient process may also be excited during system operation or fault states. This phenomenon is known as transient torque amplification (TA) [4]. The above three phenomena, which are all related to the L-C resonance of the electrical system, are called SSR. In 1985, the IEEE subsynchronous resonance (SSR) working group defined SSR as [5]:

An operation state in which a power system is disturbed and leads to the deviation of the working point. At this operation state, significant energy exchange occurs between the grid and the turbine generator at one or more frequencies lower than the system synchronous frequency. The global trend towards power generation through renewable energy sources has been raised over the last few decades due to significant advantages over coal- and fossil fuel-based power plants. The use of fossil fuels to meet the global energy demand has major drawbacks such as contributing to global warming and depletion of resources over time. These issues have given rise to the promotion of renewable energy solutions such as wind, solar PV, small hydro, biomass, geothermal, wave and tidal power [6]-[11]. For example, by end of 2020, the wind power production capacity was increased from 24GW to 650GW in the last 20 years [12]-[15]. With the development of wind power technology, government policy support and the reduction of investment cost per unit capacity, wind power generation capacity is expected to continue to rise in the future.

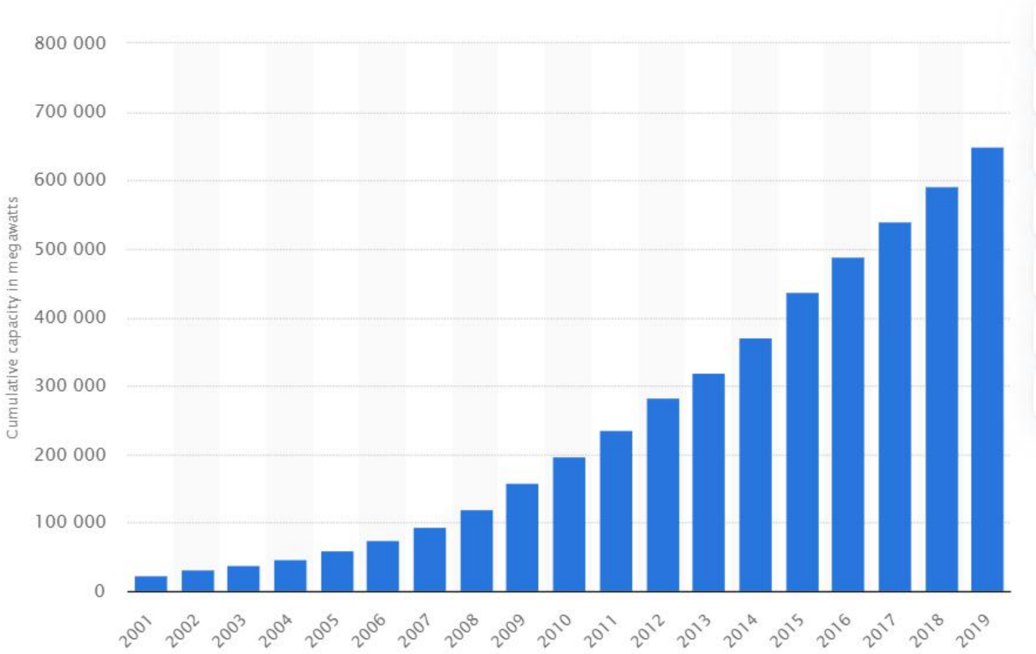

Fig.1.1 Global cumulative installed wind power capacity from 2001 to 2019 [12].

As wind power generation is increasing rapidly, it is necessary to transmit the generated power to the grids through reliable transmission networks [16]-[18]. To increase the power transfer capability and the stability of existing transmission lines, series capacitor compensation and HVDC have been generally utilised in power systems [19]-[24]. In addition, the variable speed wind turbine generators, including permanent magnet synchronous generator (PMSG), are widely used in wind farms connected to AC grids due to their excellent control characteristics [25]-[28].

However, series compensation and HVDC can cause subsynchronous interactions (SSI) with turbine generators [29]-[32]. The first WTGs-related SSI event occurred in October 2009 in Texas, USA. The event was caused by the interactions between the control of doubly-fed induction generators (DFIGs) and fixed series compensation [33]-[34]. Similar events also happened in 2010 in Hebei, China [35]-[36], which led to the drop-out of numerous WTGs and the damage of the crowbar circuits. Most of the previously reported SSI events in the last 10 years occurred with the connected WTGs, especially DFIGs, under the conditions of being integrated through series-compensated transmission systems [37]-[49].

Similarly, a newly found SSI in PMSG based wind farms that are connected to weak AC grids have been detected recently in China [50]-[51]. However, the difference is that there is no series-compensation in the PMSG connected weak grids where SSIs happened. This phenomenon has brought new challenges and concerns to the industry.

1.2 Research objectives

This thesis focuses on the analysis of the newly found SSI in VSCs connected to an AC grid. The main research objectives of this work include:

- To model the studied VSCs connected system and analyse the mechanism of the concerned SSI phenomenon.
- To investigate the system response characteristics when varying the system parameters in a single VSC and multiple VSCs connected to an AC grid respectively.
- To identify the limitations of existed methods and propose a new criterion to evaluate the stability in multiple VSCs connected to an AC grid.
- To validate the models of a single VSC and multiple VSCs connected system respectively, and to prove the correctness of the proposed criterion in multiple VSCs connected to an AC grid.

1.3 Thesis structure

The structure of the thesis is shown as follows:

Chapter 2 – Literature Review

The development of wind power technologies is overviewed. The challenges in AC grids with wind power integration are described. Some accidents caused by SSI are presented. Different opinions of the main factors on system stability are discussed. Moreover, the advantages and disadvantages of various existing analysis methods are compared with the consideration of different stability criteria.

Chapter 3 – System modelling and mechanism analysis of the new type of SSI

Mathematical models of the equivalent AC system with wind power integration are presented. Then the linear impedance model of the system is described and compared. The correctness of the developed impedance model is validated in time-domain simulations by PSCAD.

Chapter 4 – Oscillation modes analysis in a single VSC connected to an AC grid

The characteristics of a system modelled as a single VSC connected to an AC grid are analysed under various conditions. Different influence factors have been studied including feed-forward voltage low-pass filter, current loop, outer loop and phase-locked loop (PLL) of the VSC, and the number of connected WTGs as well as the line reactance in the AC grid. The mechanism of the new type of SSI is also investigated through the bode criterion. Then simulation results are presented to verify the correctness of the analysis.

Chapter 5 – Oscillation modes analysis in multiple VSCs connected to an AC grid

An equivalent system model of multiple VSCs connected to an AC grid is established. A new approach that reduces the order of the admittance-based system model matrix based on the Generalised Nyquist Criterion (GNC) is proposed. The comparisons of the new approach with traditional criteria are presented. Then the correctness of the analysis is validated through time-domain simulations.

Chapter 6 – Conclusions

The contributions of the thesis are concluded and summarised. Then the recommendations for future work are presented.

Chapter 2

Literature Review of Subsynchronous Interaction

2.1 Introduction

With the increasing penetration of renewable energy sources, especially the wind power generation, and broad applications of the power electronics based HVDC technology, electric power systems which consist of complicated AC/DC systems with multi-energy resources and multi conversions keep evolving [19]-[24]. Power electronic technology enhances the controllability and flexibility of power systems. However, it also leads to system instability problems. SSI, as one of the instability problems, attracts more concerns than previously [29]-[32]. As the understanding of SSI is extended gradually, various issues such as their causes, mechanism, impact, monitoring and damping measures bring more discussions around the world again.

This chapter provides an overview of SSI. The classifications of SSI are described, including SSR, SSCI, SSTI and the newly found SSI. Dominant SSI analysis methods are introduced and discussed. SSI damping methods in the literature are reviewed.

2.2 Classifications of SSI

Typical SSI can be divided into four main categories: 1) Subsynchronous Resonance (SSR) between synchronous generators and series capacitors; 2) Subsynchronous Control Interaction (SSCI) between controllers of wind turbine generator (WTG) and fixed series compensation; 3) Subsynchronous Torsional Interaction (SSTI) between generators and HVDC or SVC controllers; 4) The newly found SSI between power electronic devices and weak AC grid.

The research in this thesis mostly foucuses on the newly found SSI.

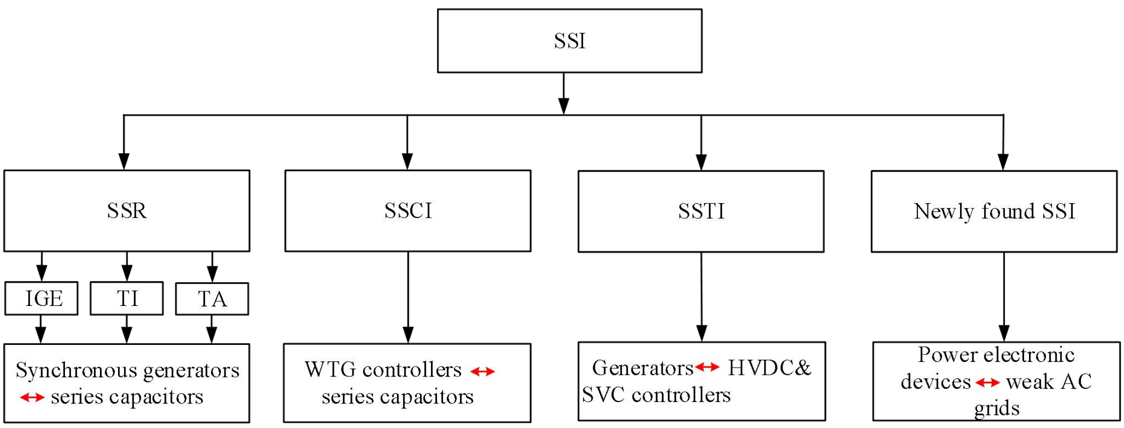

Fig. 2.1. Classifications of SSI.

2.2.1 Subsynchronous Resonance (SSR)

SSR is a kind of electromechanical oscillation phenomenon that occurs when the turbine generator connected with a series capacitor. It includes induction generator effect (IGE), torsional interaction (TI) and torque amplification (TA). The definitions of these three types of SSR are described as follows:

1) Induction generator effect (IGE)

The induction generator effect is caused by the apparent negative resistance of the rotor of a synchronous generator to the subsynchronous current component. It is assumed that the rotor of a synchronous generator rotates at a constant speed. Since the rotor speed is higher than that of the rotating magnetic field caused by the subsynchronous current component, the rotor resistance viewed from the armature terminals is negative at the subsynchronous frequency. When the value of the apparent negative resistance is more than the sum of the equivalent resistance of the armature and the power grid at the subsynchronous frequency, then the electrical self-excitation will occur, which is expected to result in excessive voltage and current [52]-[54].

2) Torsional Interaction (TI)

The shaft of a synchronous generator is composed of multiple components. When these components rotate as an entirety at the consistent synchronous frequency, they will also have relative torsional oscillations and these torsional oscillations modes have inherent natural oscillation frequency respectively. When the SSR caused by the effect of the induction generator occurs, the electromagnetic torque on the shaft which of the complementary frequency with series resonant frequency will be generated. If the natural oscillation frequency of the shaft is close to the frequency of the electromagnetic torque, the resonance between the electrical system and the mechanical system of the shaft will be produced, which is called Torsional Interaction [55]-[57].

3) Torque Amplification (TA)

When the system is subjected to a large disturbance, a severe transient transition will be produced and there will be an electrical component of large subsynchronous frequency. If the frequency of this component is complementary with the natural frequency of the shaft and the damping of the system is not large enough. Then a transient torque will be produced soon, which does fatal damage to the shaft. This phenomenon is called transient torque amplification [58]-[61].

2.2.2 Subsynchronous Control Interaction (SSCI)

SSCI is a type of oscillation caused by the interactions between the wind turbine controller and the fixed series compensation. SSCI is mainly determined by the parameters of the wind turbine controller and the transmission system and is independent of the torsional vibration frequency of the generator shaft. In addition, due to the independence of the mechanical system, the oscillating voltage and current diverge much faster than those of the conventional SSI [62]-[65].

2.2.3 Subsynchronous Torsional Interaction (SSTI)

SSTI is a type of oscillation caused by the interaction between the turbine generator shaft and the grid components. Initially, HVDC and its control system were found to be a reason for the torsional vibration of the turbine generator. Then some other active fast control devices such as power system stabiliser (PSS), static var compensator (SVC) and thyristor-controlled series compensator (TCSC) were also found to cause SSI of turbine generators in certain conditions. These devices have the characteristics of quick response and wide harmonic bands which are enough for the pass of SSR signal. As a result, they provide a closed-loop path for SSI of the shaft in turbine generators at torsional vibration mode [66]-[70].

2.2.4 Newly found SSI

The newly found SSI is a new type of oscillation between WTGs and their connected weak AC networks. As the installed capacity of wind generation increases rapidly in the Northern area of Xinjiang Uygur Autonomous Region, China, sustained power oscillations at subsynchronous frequency have been captured repeatedly by the wide-area measurement system since June 2014 [50]-[51]. These oscillations originated from those direct-drive PMSG based wind farms and spread far to the external power grids. The amplitude of the oscillatory power sometimes even exceeded that of the fundamental one. In a severe incident, such oscillation even stimulated intense torsional vibration in nearby turbogenerators, resulting in the trip of all generators in a power plant by its torsional protection system. Investigations of the system indicate that there is no series compensation nearby which is different from those previously reported SSIs.

2.3 Overview of dominant analysis methods for traditional SSIs

To investigate the SSIs, some major analysis methods are discussed as follows:

2.3.1 Time-domain simulation

The time-domain simulation method can be used to analyse the dynamic characteristics of the system after large disturbance and to verify the effectiveness of the linearisation analysis method. It can simulate electromagnetic and electromechanical transient processes of components from hundreds of nanoseconds to several seconds and reflect the trajectory of each signal with time [71]-[73]. However, time-domain simulation is time-consuming, and the internal parameters of each component need to be known when building the time-domain model of the target system. It is also difficult to analyse the mechanism of the SSI theoretically.

2.3.2 Frequency scanning method

The frequency scanning method is a useful method to analyse SSI. The research method is that when the system is in steady-state operation, a small signal disturbance with different frequencies is injected into the generator terminal where has the potential risk of SSI. According to the system response, from the wind turbine side to the grid-connected system, the equivalent impedance of other grid elements in the subsynchronous frequency range can be calculated and the curve of the subsynchronous impedance varying with frequency can be obtained. The real part and imaginary part are named equivalent resistance and equivalent reactance respectively. If at a certain subsynchronous frequency, the equivalent reactance of the whole system is close to zero, and the equivalent resistance is negative, then SSI may occur [74]-[79]. This method can effectively find wind turbines with the risk of subsynchronous oscillation. However, this method is not suitable for the calculation of nonlinear components such as power electronic devices. Besides, this method does not consider the operation mode of the system and the transient characteristics of the controller.

2.3.3 State-space small-signal analysis

The research method of state-space small-signal analysis is to linearise the studied system at the working point in the time domain. By calculating the eigenvalue of the coefficient matrix, system stability can be assessed by the positions of eigenvalues on complex planes [80]-[85]. Theory of the state-space small-signal analysis method is rigorous and the physical concept is clear. But with the increasing scale of power systems, the dimension of the state matrix of the linearised system will be very high, and this method requires detailed information for all elements in the system which is not always completely available.

2.3.4 Impedance analysis

The impedance analysis method is also a linearisation method, which uses the impedance model to characterise the external characteristics of the devices under small disturbance near the steady-state operation point, and then analyse the stability of the system. A sequence impedance model is proposed by Prof. J. Sun to assess the influence of the system parameters on SSI [86]. By applying small harmonic voltage disturbance on the device side, the harmonic current is derived, and the positive and negative sequence impedances of the device can be calculated. For most devices, the positive and negative sequence impedances are decoupled. But for power electronic devices, the coupling effect between positive and negative sequence impedances will be enhanced if considering the dynamic of PLL, which may provide inaccurate stability predictions [87]. A criterion based on the determinant-impedance characteristics of the system impedance matrix is recently proposed in [88] to overcome the drawbacks of the previous approaches, but the applicability of multiple VSCs connected system still needs to be studied. The impedance analysis method is more effective for the analysis of the SSI caused by electronic devices. It can evaluate the stability of the whole system with different system operation modes and suitable for large-scale systems. But it is not suitable for the analysis of the SSI caused by the transient torque amplification and difficult to investigate the influence of the system parameters on stability separately.

2.3.5 Amplitude and phase motion analysis

Amplitude and phase motion analysis method is proposed in [89] to analyse SSI. By applying this method, the control effects in VSC are considered based on the motion equation concept. The form of the model based on this method is similar with the rotor motion equation of synchronous generator (SG), which has been effectively used to analyse the rotor dynamics in conventional SG dominated power systems. This method can describe VSC's external characteristics independent of the power network, which makes it be easily extended to the modelling of multiple VSCs and suitable for power system analysis. But the concept of it is complicated and it is difficult to study the interactions among different VSCs.

2.4 Damping approaches of traditional SSIs

With the occurrence of SSIs, researchers have proposed many damping methods, and the suppression methods are various for different types of SSIs which are summarised in the following parts.

2.4.1 Suppression of SSR

The suppressing measures of SSR can be divided into four categories: 1) filtering and damping, 2) relay protection and monitoring protection, 3) system switch operation and removal of units, 4) reforms of units and power systems. Among these 4 measures, methods of filtering and damping occupy a great proportion in research and engineering recently as the main means to suppress SSR. Therefore, some methods of damping SSR by filtering and damping are introduced as follows:

1) Blocking Filter (BF)

BF is composed of inductance, capacitance and resistance in parallel with the high-quality factor of a three-phase filter. Using BF can be an effective method to mitigate the SSR problems of the affected generator. In [90], a BF design scheme is proposed which can meet the needs of suppressing Torsional Interaction (TI) and Transient Torque Amplification (TA problems. This method decoupled asynchronous self-excitation from TI and can be applied to the transmission system with a much higher degree of series compensation. Therefore, this BF design scheme is more convenient than the method of adding small resistance to the reactor circuit. However, when BF is utilised, unstable self-excitation (SE) may occur unexpectedly in engineering. In [91], the quality factor (Q) of BF reactors is discovered that it has a negative impact on system stability. By appropriately lowering the Q of BF reactors with supplemental resistors, an improved BF scheme is proposed to suppress the different types of SSR problems. The key of the improved scheme is to design a set of minimum supplemental resistors that could maximise its blocking effect while simultaneously stabilising SE modes. Finally, the effectiveness of the improved BF is verified with field tests.

2) Supplementary Excitation Damping Controller (SEDC)

As a countermeasure to SSR, SEDC provides electrical damping by modulating the excitation voltage at the rotor side based on the excitation control system. SEDC has the advantages of investment cost, land occupation, operational loss and flexibility [92]. However, limited by the capacity of the excitation system, the ability of SEDC to inhibit SSR cannot meet the need of power systems. Consequently, SEDC is used collaboratively with other control methods to deal with SSR problems generally. In [93], a combined mitigation scheme of SEDC and generator terminal subsynchronous damping controller (GTSDC) is proposed. SEDC provides electrical damping by modulating the excitation voltage at the rotor side. Meanwhile, GTSDC can damp SSR via injecting complementary supersynchronous and subsynchronous currents into the generator stator. This combined scheme could not only provide sufficient damping to the system, but also could decrease the capacity of the converters of GTSDC and the total investment cost.

3) Static Var Compensator (SVC)

SVC is a kind of applications in Flexible AC Transmission Systems (FACTS) to deal with voltage fluctuation. And SVC is a reactive power resource which can adjust quickly, improve the voltage stability and increase the capacity of transmission power. Historically, SVC had been applied to control bus voltage and to damp out low-frequency oscillations for many years. But in the meantime, SVC also has the ability to damp SSR in power systems by appropriate control strategies [94]. In [95], an SVC is installed in the high voltage side of the generator step-up transformer. By utilising extra voltage control and modal separation control, the SVC is controlled to output modal complementary frequency current of proper amplitude and phase and then generate the corresponding modal damping torque. The result of the time-domain simulation proves the validity of these two kinds of control schemes of effectively controlling SVC to suppress SSR. [96] presents an effective control method for an SVC to damp SSR in wind power plants. The controller uses an easily accessible input signal, and its gain is adaptive to the wind generation level. And the developed controller has proved to be effective for various wind generation levels and different operating conditions.

4) Thyristor Controlled Series Capacitor (TCSC)

TCSC is a FACTS device that consists of a series capacitor and a thyristor-controlled reactor in parallel. Generally, the functions of TCSC are to control the power flow, limiting short circuit current and providing stability enhancement of power system. In addition, TCSC can be also utilised to mitigate the SSR. In [97], a dynamic phasor-based impedance model for TCSC is proposed and TCSC's ability in damping SSR in Type-3 wind generator inter-connection systems is proved. The results are validated time-domain simulation in MATLAB. It is also reported in [98] that a TCSC with a closed-loop current control offers more resistance at increased levels of series compensation in the subsynchronous frequency when employed in a transmission system. This control mode is found to be effective in damping SSR both due to torsional interaction and induction generator effects.

5) Static Synchronous Series Compensator (SSSC)

SSSC is a serially connected synchronous voltage source connected in series which can change the effective impedance of transmission line by injecting voltage of an appropriate phase with line current. For the reason that SSSC can modulate the line reactance and resistance according to the oscillation characteristics of the line, SSSC has more potentialities than TCSC [99]. A controller of SSSC is proposed in [100] which consisting of two control loops. One is for reactive power control and another loop is for active power control. By using this control scheme, the amplitude and phase of the inserted ac compensating voltage can be rapidly adjusted so that the damping torque of the same phase with deviated angular velocity can be added to the electrical torque of the generator. Therefore, the effectiveness of SSSC to damp SSR has been confirmed. In [101], an SSSC based on a three-level 24-pulse VSC in a hybrid series compensated system is analysed. This SSSC improves the damping of all the critical torsional modes by the proposed subsynchronous current suppressor although the peak negative damping is decreased. As the electrical resonance condition is eliminated in the practical range of series compensation levels and the network resonant frequency is detuned, the risk of SSR is reduced.

6) Static Synchronous Compensator (STATCOM)

STATCOM is a type of parallel FACTS device. The utility model of STATCOM is a bridge converter which is composed of fully controlled power electronic devices to realise the dynamic emission or absorption of reactive current. In [102], as a three-phase fault close to the wind farm may cause oscillations in the point of common coupling (PCC) voltage, shaft torque and electromagnetic torque of the wind turbine generator, a STATCOM with voltage control is installed at the point of common coupling. And the potential of SSR both in steady-state and during faults is reduced. In [103], a detailed model of the study system and the design of the STATCOM controller are discussed, the DC voltage is uncontrolled while the reactive current is controlled by adjusting the angle. The simulations confirm that a STATCOM connected at the terminals of the wind farm can successfully damp out SSR.

2.4.2 Suppression of SSCI

Methods to suppress SSCI can be mainly divided into: Subsynchronous Damping Controller (SSDC), Flexible AC transmission system (FACTS) devices, instalment of blocking filter or bypass filter, arrangements for the operation of the system and the proportion of grid-connected wind turbines. The details of those methods are described as follows:

1) SSDC

Recently, research shows that the current controller at the rotor side of DFIG has more obvious impacts on SSCI than the controller at other sides. Therefore, adding SSDC to the controller at the rotor side can optimise the control of the DFIG and be more effective to damp SSCI [104]. A scheme designed to damp SSCI is proposed in [105]. In this scheme, an SSDC is added to the collection bus of wind farms. This SSDC operates nearly as pure resistance within the resonance frequency range and almost does not influence fundamental frequency components. Therefore, this SSDC can diverge resonance power and provide positive damping for SSCI. In [106], another SSDC is presented. The designed SSDC has a significant effect on mitigating SSCI and reducing the risk of wind generation tripping without the inclusion of expensive additional damping devices, such as FACTS or bypass filters.

2) FACTS devices

Using FACTS devices to suppress SSCI can be both relied on the main control functions of the FACTS device by additional control and the specialised SSCI damping control strategy. In [107]-[109], SVC, TCSC and GCSC are used to suppress SSCI respectively when the system is unstable. Using these FACTS has the advantages of fast response and good inhibition effect, while the investment is kind of uneconomical and the control scheme is complex.

3) Installment of blocking filter or bypass filter

Similar to the SSR in thermal units, utilising the blocking filter can block the flow of the resonant current in the transmission line, which can avoid the occurrence of SSCI. Moreover, the bypass filter can also suppress SSCI in fixed series compensation by adjusting the parameters of L, C, R to make the parallel resonance occurs at the power frequency state so the power current will not through the bypass filter. When there is a resonant current in the circuit, the bypass filter presents a small impedance and the resonant current flows through the bypass filter, which is equivalent to add a series of resistance in the system. As a result, the resistance of the system will increase [110].

4) Arrangements for the operation of the system and the proportion of grid-connected wind turbines

Most SSCI problems occur in the case that the wind power is sent only by fixed series compensation, and whether SSCI will occur is related to the operation of the system. Therefore, when planning the operation mode of the system, it is necessary to do the simulation and analyse the possibility of occurring SSCI under various operation modes and as far as possible to avoid the operation which may lead to SSCI [111].

2.4.3 Suppression of SSTI

SSDC is mostly used to suppress SSTI that has good applicability and reliability. SSDC is a controller that generating a control signal as an additional control signal of the HVDC control system. It can provide a proper electrical damping compensation for the turbine generator and finally achieve the purpose of inhibiting SSI. In the controller designed in [112], the rotation rate of the generator is used as the feedback signal and the oscillation components are obtained through the filter. The control signals of each oscillation component obtained by the gain and phase-shifting links are superimposed and attached to the control of reactive power. And this superimposed signal can generate a compensated current of the same frequency with oscillation components. Under the action of the magnetic field of the stator, the superimposed signal will generate a compensated electromagnetic torque increment which has a consistent frequency with the oscillation components. Finally, a positive damping torque is produced, and the purpose of suppressing SSI is achieved. Typically, SSDC is used to damp the SSI of HVDC on one or two lower range subsynchronous torsional modes. In [113], using one common SSDC structure to damp SSI of HVDC on five torsional frequencies within the torsional frequency range 5-20 Hz is evaluated. The contribution of proposed SSDC structures to subsynchronous damping of multiple lower range subsynchronous torsional oscillations is explained.

2.5 Investigation and suppression of the newly found SSI

The mechanism and characteristics of SSI are complex due to involving the complicated dynamic interaction between WTG converters and the power grid. The oscillation frequency of SSI presents time-varying characteristics and most of the oscillations start from a divergent small signal, and gradually becomes a nonlinear continuous oscillation. Paper [114] explains the instability mechanism of the VSC grid-connected system from the perspective of system damping and generalised impedance, which is helpful to understand the SSI between the VSC and HVDC control system. Paper [115]-[117] find that the interaction between PLL and current inner loop, PLL and outer loop has a significant impact on the stability of VSC grid-connected system. Paper [118]indicates that the "negative resistance effect" of PLL on the inner current loop will affect the stability of VSC grid-connected system. Although the above papers have made great contributions to the deep understanding of SSI, theoretically there was still no clear and common conclusion of the physical mechanism of the SSI.

Analysis methods of the newly found SSI are mainly divided into time-domain methods and frequency-domain methods. Time-domain analysis methods include the eigenvalue analysis method based on the state-space small-signal model and the time-domain simulation method based on the electromagnetic transient model. In the frequency domain, the impedance analysis method is mainly used. In [88], a small-signal state-space model and an electromagnetic transient model of direct-drive PMSG based wind farms connected to a weak AC grid system are proposed. The related factors affecting the system stability are analysed, including the number of WTGs connected to the system, the reactance of transmission line, the output power of WTGs and control parameters of WTGs. In [36], an equivalent model of DFIG based wind farms grid-connected system is established. The SSI modes are studied by calculating the eigenvalues and analysing the sensitivity of the system.

A sequence impedance model-based analysis is used to study the influence of grid and VSC control parameters on system stabilities [86]. By applying a small amplitude harmonic voltage disturbance at the device side, the harmonic current is derived, and the positive and negative sequence impedances of the device are obtained. For most devices, the positive and negative sequence impedances are decoupled. However, for the equipment with power electronic control, if considering the dynamic of PLL, the coupling effect between positive and negative sequence impedances will be enhanced, which cannot be neglected. Therefore, the impedance model in the *dq* coordinate system is widely used recently. By establishing the impedance model in the *dq* coordinate system, the Nyquist and Bode criteria are extensively utilised to analyse the closed-loop system in [119]-[121]. A criterion based on the determinant-impedance characteristics of the system impedance matrix is recently proposed in [88]. The positive-net-damping stability criterion is also currently arising as a powerful tool for system instability studies [122].

The main suppression methods of the newly found SSI are optimising system parameters or using SSDC. Paper [88] points out that reducing the number of WTGs connected to an AC grid or changing the grid structure to increase the strength of the AC grid can reduce the risk of SSI. However, reducing the number of WTGs connected to the AC grid will affect the consumption of wind energy, changing the grid structure will increase investment and the increment of grid strength is limited. The stability of SSI is also affected by many parameters of the VSC control system, therefore, optimising the parameters of the VSC can reduce the risk of SSI. Paper [123] analyses the optimisation design for phase-locked loop without considering the interaction with other loops. Paper [124] provides the stability region of each VSC parameter respectively for a single VSC connected to an AC grid, without considering the interaction between different VSC parameters stability regions. In [125], the stability region of the current loop of VSC in a single VSC connected weak AC system is analysed without considering the DC voltage link. However, the stability region of VSC parameters in a complete VSC control system still needs to be analysed. In terms of parameter optimisation of various links of multiple VSCs, [126]-[127] provides the stability region of VSC parameters for the oscillation problem in offshore wind farms based flexible HVDC transmission system, but the results are not suitable for the scenario of wind farms connected to AC system. [88] presented a simple but effective SSI mitigation scheme based on SSDC, the proposed SSDC is attached to the grid-side controller of a PMSG. It can pick out the concerned subsynchronous signal and flexibly adjust the magnitude and phase of the signal to achieve better control performance and improve system stability.

The above research on the newly found SSI in wind farms grid-connected systems has made some contributions. However, due to different grid-connected structures, different types of wind turbines and different control parameters, the mechanism of the newly found SSI is not the same, and the analysis methods still need to be improved. Challenges and prospects of the research on the newly found SSI are as follows:

1) Due to the complexity of the structure of the wind farms grid-connected system and different oscillation modes, the mechanism of the newly found SSI is complicated and still unclear.

2) Most of the research is to establish the equivalent model of a single machine infinite bus system to analyse the SSI problem. The interactions among different wind turbines are usually ignored and it is difficult to quantitatively analyse the system characteristics. However, there are dynamic interactions among different wind turbines, including the interactions among multiple converters and the interactions between converters and AC/DC power grid. Moreover, the control modes of wind farms grid-connected systems are various, resulting in complex factors affecting system stability and variable oscillation frequency.

3) It is necessary to improve the method to analyse the SSI characteristics of wind farms grid-connected systems with the participation of power electronic devices. The

linearisation methods are mostly used, while the research on the nonlinear characteristics of the newly found SSI.

4) Impedance analysis method, compared with the traditional methods, is more suitable for the analysis of large-scale systems and can adapt to the change of system operation mode because it focuses on the external characteristics of each subsystem and their correlations. It is more convenient to analyse the dynamic behaviour of the whole system. Besides, there are different stability criteria based on the impedance analysis method to study single machine infinite bus systems, but the stability criterion for multi-machine systems still needs to be investigated.

2.6 Summary

Different types of SSIs are reviewed in this chapter. Main SSIs founded in the past years can be classified as SSR, SSCI, SSTI and the newly found SSI. The definition of each type of SSI has been illustrated.

The main SSI analysis approaches to study the SSI characteristics of the system have been summarised including time-domain simulation, frequency scanning method, state-space small-signal analysis and impedance analysis. The principles of these methods are explained and the applicability of them are discussed when evaluating different systems. Each method has its own advantages and limitations in achieving different research purposes.

SSI damping approaches in order to reduce or eliminate the impacts of SSI on the systems are described. SSR suppression measures include filtering and damping, relay protection and monitoring protection, system switch operation and removal of units, reforms of units and power system. The effectiveness of BF, SEDC, SVC, TCSC, SSSC, STATCOM to damp SSR are presented respectively. The damping methods of SSCI are introduced, SSDC, FACTS devices, instalment of blocking filter or bypass filter, arrangements for the operation of the system and the proportion of grid-connected wind turbines are mainly used to suppress SSCI. Moreover, SSDC also has good performance to damp SSTI.

The investigation and suppression of the newly found SSIs are presented. The influence of different parameters on system stability is discussed including strength of AC system, the bandwidth of PLL, inner loop and outer loop of VSC. Time-domain and frequency-domain methods are discussed towards different SSI scenarios. Compared with the time-domain methods, the impedance analysis method in frequency-domain is more suitable both for single VSC connected AC system and multi VSCs connected AC system because it only focuses on the external characteristics and correlation of each subsystem, which is mainly used to analyse SSI characteristics in the following chapters. The main suppression methods of the newly found SSI are optimising system parameters or using SSDC. By optimising parameters of PLL, inner loop and outer loop of VSC or increase the strength of connected AC system, or attaching SSDC in VSC, the system stability can be improved effectively.

Chapter 3
Modelling of VSC connected to an AC grid

3.1 Introduction

The state-space model in the time domain and the impedance model in the frequency domain are the two most widely used modelling methods to analyse SSI nowadays. The state-space model can analyse the system stability through eigenvalue analysis. By linearising the system at the operating point, the eigenvalues and eigenvectors are calculated, and the damping and frequency of the system are obtained to assess system stability. By sensitivity analysis, the influence of network structure, operating conditions and component parameters on the SSI characteristics can be quantitatively studied.

The impedance model in frequency-domain can assess system stability by various criteria such as eigenvalue analysis, GNC, determinant-impedance criterion and so on. It generally establishes the models of the target network and the rest parts respectively to form a closed-loop interconnected model. This method can clearly analyse the characteristics of SSI and is useful to investigate the mechanism of SSI.

In this chapter, an equivalent system model of a single VSC connected to an AC system is established. State-space model and impedance model of the studied system are proposed and compared. An example of a studied system which corresponds to the SSI scenario in the actual installation is presented. Then the correctness of the linearised model is verified by time-domain simulations.

3.2 State-space model

This section established the mathematical model of the system described by ordinary differential equations and the linearisation model at the stable operating point. The derivation of mathematical and linearised models for the studied system are presented.

3.2.1 Mathematical Model

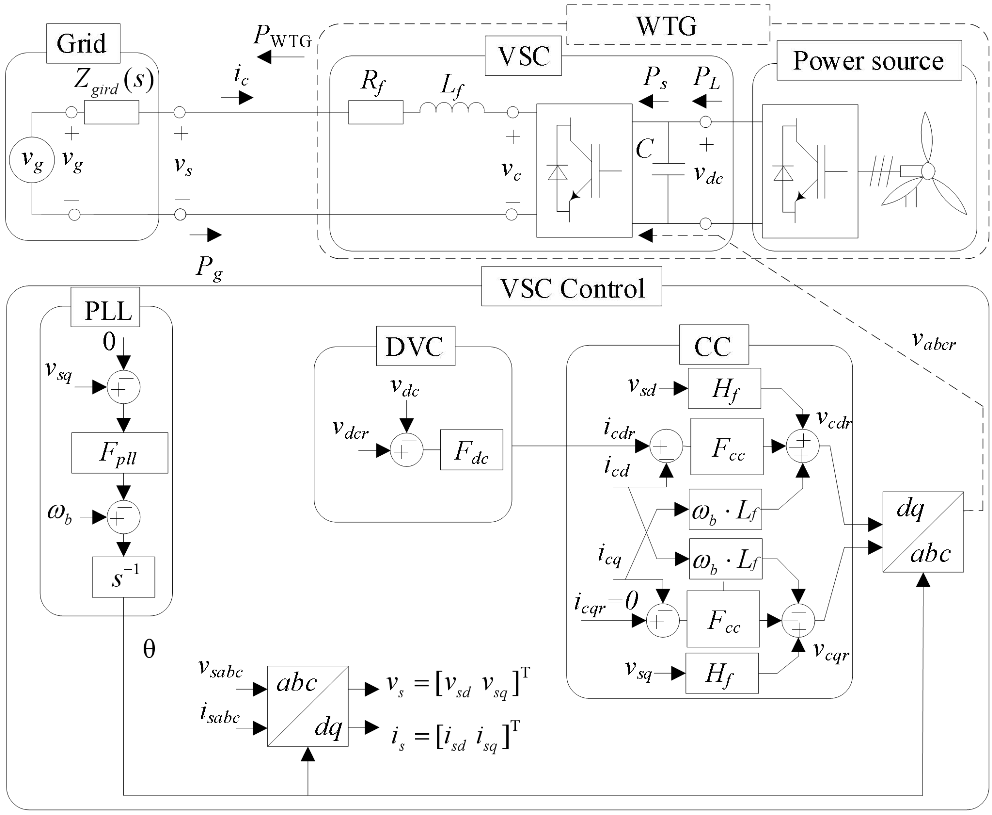

Fig. 3.1. System model of a single VSC connected to an AC grid.

The system model of a single VSC connected to an AC grid is proposed as shown in Fig. 3.1. WTG is equivalent to a VSC connected to a controlled current source. VSC control is represented with the inner current loop controller (CC), outer loop controller and PLL controller. A constant DC-link voltage control scheme is used in the outer loop, so it is named DC-link voltage controller (DVC) here. The DVC generates the *d*-component of the CC reference current i_{cdr} and the PLL drives the *q*-component of voltage v_{sq} on the point of common coupling (PCC) in the converter *dq* frame to zero providing the transformation angle *θ*. The *q*-component of the CC reference current i_{cqr} is set to zero by assuming that VSC is operating at unity power factor which is common in normal operating conditions.

1) AC grid

According to Fig. 3.1, the time-domain equation of the AC network dynamic process expressed by sinusoidal instantaneous value is

$$v_{s\_abc} - v_{c\_abc} = R_f i_{c\_abc} + L_f \frac{di_{c\_abc}}{dt} \tag{3-1-1}$$

For a more convenient design of the controller, the above dynamic process of AC network is usually expressed in the *dq*-frame by multiplying the equations with Park transformation matrix. Then the equations expressed in *dq*-frame are obtained as

$$\begin{cases} v_{sd} - v_{cd} = R_f i_{cd} + L_f \frac{\mathrm{d}i_{cd}}{\mathrm{dt}} - \omega_b L_f i_{cq} \\ v_{sq} - v_{cq} = R_f i_{cq} + L_f \frac{\mathrm{d}i_{cq}}{\mathrm{dt}} + \omega_b L_f i_{cd} \end{cases} \tag{3-1-2}$$

Where ω_b is the base frequency of the AC system, R_f and L_f are the resistance and inductance of the VSC filter. The active and reactive power at the output side of the converter are represented as

$$\begin{cases} P_s = v_{sd} i_{cd} + v_{sq} i_{cq} \\ Q_s = v_{sq} i_{cd} - v_{sd} i_{cq} \end{cases} \tag{3-1-3}$$

2) Control systems

The control system is mainly composed of PLL, inner current loop and outer loop. The design of the control system is based on the synchronization rotating frame (named ***c***), which is determined by the output phase of the phase-locked loop. The *d*-axis of the frame in the control system is usually synchronised with the orientation of the primary system voltage and the *dq*-frame of the primary system through PLL. The mathematical models of the relationship between different synchronization rotating frames and the components of the control system are presented in the following parts.

a) Transformation of frames

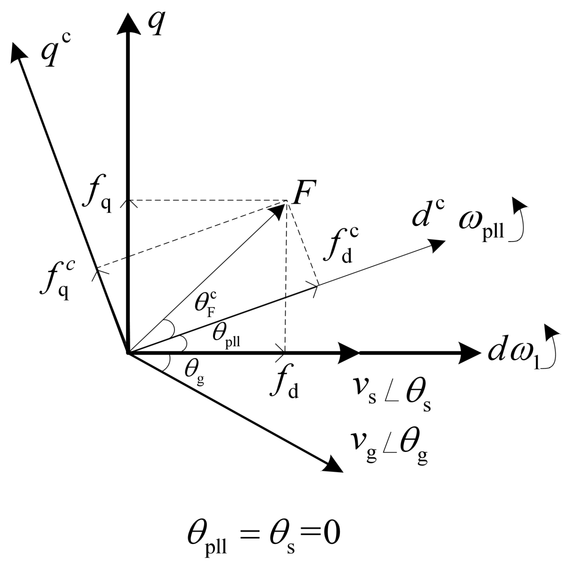

Fig. 3.2. Grid-connected VSC system model.

The relationship between the *dq*-frame in the control system and primary system is shown in Fig. 3.2. In this research, the control system of VSC is based on *dq*-frame, in which the d-axis is orientated to the grid voltage *vs* and *q*-axis is 90° ahead of the *d*-axis. And under this condition, θ_{pll}=θ_s=0. The relationship of Phasor *F* between the two coordinate systems can be expressed as

$$\begin{bmatrix} f_d \\ f_q \end{bmatrix} = \begin{bmatrix} \cos\theta_{pll} & -\sin\theta_{pll} \\ \sin\theta_{pll} & \cos\theta_{pll} \end{bmatrix} \begin{bmatrix} f_d^c \\ f_q^c \end{bmatrix} \tag{3-1-4}$$

$$\begin{bmatrix} f_d^c \\ f_q^c \end{bmatrix} = \begin{bmatrix} \cos\theta_{pll} & \sin\theta_{pll} \\ -\sin\theta_{pll} & \cos\theta_{pll} \end{bmatrix} \begin{bmatrix} f_d \\ f_q \end{bmatrix} \tag{3-1-5}$$

b) PLL

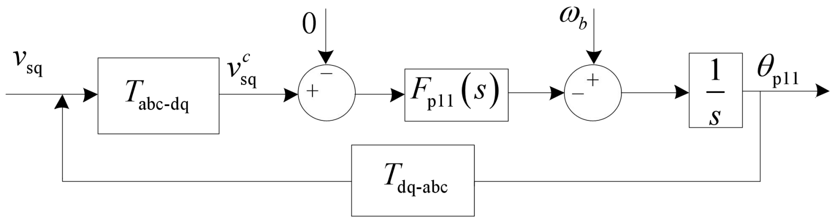

Fig. 3.3. Block diagram of PLL.

The block diagram of PLL is shown in Fig. 3.3, $T_{abc\text{-}dq}$ and $T_{dq\text{-}abc}$ represent the process of variables transferred from *abc*-axis to *dq*-axis and from *dq*-axis to *abc*-axis respectively. The deductions of $T_{abc\text{-}dq}$ and $T_{dq\text{-}abc}$ are presented in Appendix A. The transfer function shown in Fig. 3.3 can be described as follows

$$\theta_{pll} = (-F_{pll}(s)v_{sq}^c + \omega_b)\frac{1}{s} \tag{3-1-6}$$

where $F_{pll}(s) = k_{p\_pll} + k_{i\_pll}/s$ is the proportional-integral controller.

c) Inner current loop

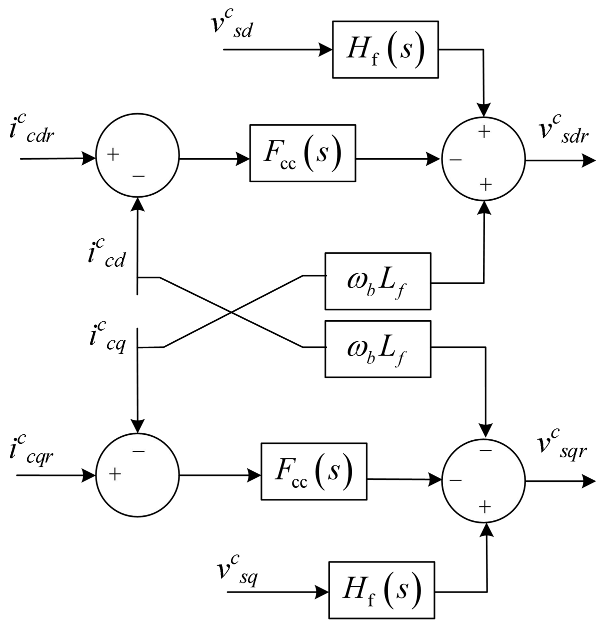

Fig. 3.4. Control scheme of inner loop control.

The diagram of inner current loop control is shown in Fig. 3.4. According to the control scheme, the expression of the inner loop control can be represented as

$$\begin{cases} v^c_{sdr} = H_f(s)v^c_{sd} - F_{cc}(s)\left(i^c_{cdr} - i^c_{cd}\right) + \omega_b L_f i^c_{cq} \\ v^c_{sqr} = H_f(s)v^c_{sq} - F_{cc}(s)\left(i^c_{cqr} - i^c_{cq}\right) - \omega_b L_f i^c_{cd} \end{cases} \quad (3\text{-}1\text{-}7)$$

Where $H_f(s)=\omega_f/(s+\omega_f)$ is the feed-forward voltage low-pass filter, $F_{cc}(s)=k_{p\_cc}+k_{i\_cc}/s$ is the proportional-integral controller of current loop.

d) Outer loop

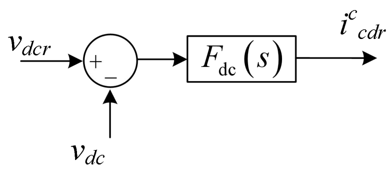

Fig. 3.5. Control scheme of inner loop control.

Outer loop control mainly consists of constant DC voltage control, constant active power control and active power open-loop control. As shown in Fig. 3.5, the constant DC voltage control is utilised in this study, the expressions for generating reference current are represented as

$$i^c_{cdr} = F_{dc}(s)(v_{dcr} - v_{dc}) \quad (3\text{-}1\text{-}8)$$

where $F_{dc}(s)= k_{p\_dc}+k_{i\_dc}/s$ is the proportional-integral controller of outer loop.

3.2.2 Linearised Model

The output disturbance of PLL caused by PCC voltage disturbance will cause the dq synchronous rotating coordinate system of the primary system and control system to be out of synchronization temporarily. But voltage and current of the primary system will be involved in the calculation of the d-axis and q-axis voltage of the converter after the dq transformation by using the PLL output phase. Then, the PLL output phase is used for the dq inverse transformation again to get the modulation signal of the converter control, and finally, form a closed-loop feedback to affect the primary system. The details of the linearised model are shown in the following sections.

1) AC grid

Linearised model of the dynamic process of AC network in the dq-frame after the transformation from time-domain mathematical model to s-domain can be expressed as

$$\begin{cases} \Delta v_{sd} - \Delta v_{cd} = (R_f + sL_f)\Delta i_{cd} - \omega_b L_f \Delta i_{cq} \\ \Delta v_{sq} - \Delta v_{cq} = (R_f + sL_f)\Delta i_{cq} + \omega_b L_f \Delta i_{cd} \end{cases} \tag{3-2-1}$$

The linearised model of power at grid side in s-domain can be described as

$$\begin{cases} \Delta P_s = v_{sd0}\Delta i_{cd} + v_{sq0}\Delta i_{cq} + i_{cd0}\Delta v_{sd} + i_{cq0}\Delta v_{sq} \\ \Delta Q_s = v_{sq0}\Delta i_{cd} - v_{sd0}\Delta i_{cq} + i_{cd0}\Delta v_{sq} - i_{cq0}\Delta v_{sd} \end{cases} \tag{3-2-2}$$

2) Control system

The linearised model of the control system consists of the transformation of the frame, linearisation of PLL, inner current loop and outer loop. The details of derivation are as follows:

a) Transformation of frame

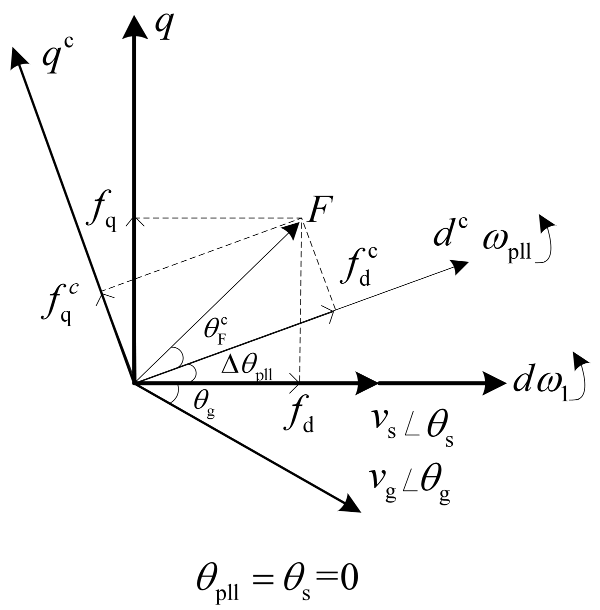

Fig. 3.6. Control scheme of inner loop control.

When the small disturbance appears in voltage *v*s, there is also a small disturbance in the output phase of PLL, which will lead to a migration between the *dq*-frame of the control system and primary system. The relationship between the two frames is shown in Fig. 3.6.

And transfer expressions between the small perturbation variables in two frames are as follows

$$\begin{bmatrix}\Delta f_d\\ \Delta f_q\end{bmatrix}=\begin{bmatrix}cos\theta_{pll0} & -sin\theta_{pll0} & (-sin\theta_{pll0}f^c_{d0}-cos\theta_{pll0}f^c_{q0})\\ sin\theta_{pll0} & cos\theta_{pll0} & (cos\theta_{pll0}f^c_{d0}-sin\theta_{pll0}f^c_{q0})\end{bmatrix}\begin{bmatrix}\Delta f^c_d\\ \Delta f^c_q\\ \Delta\theta_{pll}\end{bmatrix} \quad (3\text{-}2\text{-}3)$$

$$\begin{bmatrix}\Delta f^c_d\\ \Delta f^c_q\end{bmatrix}=\begin{bmatrix}cos\theta_{pll0} & sin\theta_{pll0} & (-sin\theta_{pll0}f_{d0}+cos\theta_{pll0}f_{q0})\\ -sin\theta_{pll0} & cos\theta_{pll0} & (-cos\theta_{pll0}f_{d0}-sin\theta_{pll0}f_{q0})\end{bmatrix}\begin{bmatrix}\Delta f_d\\ \Delta f_q\\ \Delta\theta_{pll}\end{bmatrix} \quad (3\text{-}2\text{-}4)$$

Where $\boldsymbol{f}$ represents variables $\boldsymbol{v_c}$, $\boldsymbol{v_s}$ and $\boldsymbol{i}$. Considering $\theta_{pll}=\theta_s=0$, equations (3-2-3) and (3-2-4) can be rewritten as

$$\begin{bmatrix}\Delta f_\mathrm{d}\\ \Delta f_\mathrm{q}\end{bmatrix}=\begin{bmatrix}1 & 0 & -f^\mathrm{c}_\mathrm{q0}\\ 0 & 1 & f^\mathrm{c}_\mathrm{d0}\end{bmatrix}\begin{bmatrix}\Delta f^\mathrm{c}_\mathrm{d}\\ \Delta f^\mathrm{c}_\mathrm{q}\\ \Delta\theta_\mathrm{pll}\end{bmatrix} \quad (3\text{-}2\text{-}5)$$

$$\begin{bmatrix}\Delta f^\mathrm{c}_\mathrm{d}\\ \Delta f^\mathrm{c}_\mathrm{q}\end{bmatrix}=\begin{bmatrix}1 & 0 & f_\mathrm{q0}\\ 0 & 1 & -f_\mathrm{d0}\end{bmatrix}\begin{bmatrix}\Delta f_\mathrm{d}\\ \Delta f_\mathrm{q}\\ \Delta\theta_\mathrm{pll}\end{bmatrix} \quad (3\text{-}2\text{-}6)$$

b) PLL

By linearising (3-1-6) and combining (3-2-6), it can be obtained that

$$\begin{cases} \Delta\theta_{pll} = \frac{-F_{pll}(s)}{s}\Delta v_{sq}^{c} \\ \Delta v_{sq}^{c} = \Delta v_{sq} - v_{sd0}\Delta\theta_{pll} \end{cases} \tag{3-2-7}$$

And then the expression of PLL shown in equation (3-2-8) can be deducted from the above equations.

$$\Delta\theta_{pll} = \frac{-F_{pll}(s)\Delta v_{sq}}{s - v_{sd0}F_{pll}(s)} = G_{pll}(s)\Delta v_{sq} \tag{3-2-8}$$

c) Inner current loop

The linearised expression of the mathematical model of inner loop current control (3-1-7) is shown in equation (3-2-9).

$$\begin{cases} \Delta v_{\mathrm{cdr}}^{\mathrm{c}} = H_{\mathrm{f}}(s)\Delta v_{\mathrm{sd}}^{c} - F_{\mathrm{cc}}(s)(\Delta i_{\mathrm{cdr}}^{\mathrm{c}} - \Delta i_{\mathrm{cd}}^{\mathrm{c}}) + \omega_{\mathrm{b}}L_{f}\Delta i_{\mathrm{cq}}^{\mathrm{c}} \\ \Delta v_{\mathrm{cqr}}^{\mathrm{c}} = H_{\mathrm{f}}(s)\Delta v_{\mathrm{sq}}^{c} - F_{\mathrm{cc}}(s)(\Delta i_{\mathrm{cqr}}^{\mathrm{c}} - \Delta i_{\mathrm{cq}}^{\mathrm{c}}) - \omega_{\mathrm{b}}L_{f}\Delta i_{\mathrm{cd}}^{\mathrm{c}} \end{cases} \tag{3-2-9}$$

Where $H_f(s)$ in the above equation represents the transfer function of the filter

d) Outer loop

The small perturbation equations of the outer loop in the control system which derived from (3-1-8) are as follows

$$\Delta i_{\mathrm{dr}}^{\mathrm{c}} = F_{\mathrm{dc}}(s)(\Delta v_{\mathrm{dcr}} - \Delta v_{\mathrm{dc}}) =- F_{dc}(s)\Delta v_{\mathrm{dc}} \tag{3-2-10}$$

By combining the above linearised models, the state-space small-signal model of the studied system can be obtained, and the system stability can be assessed by the eigenvalue analysis of the small-signal model. This method is clear and rigorous for the theory, but the disadvantage of it is that the derivation process is complicated, and it needs to establish the relationship between the differential of each variable with all other state variables. When the number of state variables increases, the derivation is very difficult. Moreover, it requires the parameters of all elements which is not always completely available.

3.3 Impedance model

An impedance linearised model is derived in this section, which characterises the external characteristics of the devices under small disturbance near the steady-state operation point, and then analyse the stability of the system. The details of the modelling process are as follows:

1) AC grid

The dynamic equations of the grid in the dq-frame with the VSC input voltage v and current i are

$$v_g = \begin{bmatrix} v_{gd} \\ v_{gq} \end{bmatrix} = \underbrace{\begin{bmatrix} Z_{g,dd}(s) & Z_{g,dq}(s) \\ Z_{g,qd}(s) & Z_{g,qq}(s) \end{bmatrix}}_{Z_{grid}(s)} i + v \tag{3-3-1}$$

For a symmetric system, it can be concluded that $Z_{g,dd}(s)=Z_{g,qq}(s)$ and $Z_{g,dq}(s)=-Z_{g,qd}(s)$. In particular, transformers and medium and high voltage lines can be modelled as R-L circuits at SSI frequencies and the impedance matrix of these components is

$$Z_{grid}(s) = \begin{bmatrix} R_g + L_g s & -L_g \omega_b \\ L_g \omega_b & R_g + L_g s \end{bmatrix} \tag{3-3-2}$$

where $\omega_b = 2\pi f_b$ (f_b =50Hz) is the fundamental angular frequency of the grid. The impedance matrix of the grid commonly presents the same structure as $Z_{grid}(s)$.

2) Control systems

The factors of each loop and the dynamic interactions among them in the VSC control systems will affect the system stability. There are also various SSI characteristics and mechanisms in different impedance modelling scenarios. Therefore, the different impedance modelling scenarios are considered to meet the requirement of analysing the SSI stability affected by different loops separately, which are: 1) with inner loop only (the effects of the outer loop and PLL are neglected), 2) with inner loop and outer loop only (the effects of PLL are neglected), 3) with inner loop, outer loop and PLL (the effects of all of them are considered).

a) With inner loop only

Based on (3-2-1) and (3-1-7), the equations of the output AC voltage v_s in current control loop (CC) can be expressed with complex transfer functions (3-3-3) due to the real transfer functions are symmetrical and this makes the VSC modelling easier. These equations are as follows:

$$\begin{cases} \boldsymbol{v_c} = \boldsymbol{v_s} - (R_f + L_f s + jL_f\omega_b)\boldsymbol{i_c} \\ \boldsymbol{v_{c,r}} = D\left[- F_{cc}(s)(\boldsymbol{i_{cr}} - \boldsymbol{i_c}) + H_f(s)\boldsymbol{v}_s - jL_f\omega_b \boldsymbol{i_c}\right] \\ \boldsymbol{v_c} = \boldsymbol{v_{c,r}} \end{cases} \tag{3-3-3}$$

where the variables $\boldsymbol{v}=v_d+jv_q$ and $\boldsymbol{i_c}=i_{cd}+i_{cq}$ are the complex space vectors of the VSC input voltage and current in the dq-frame. The variable $v_s=v_{sd}+jv_{sq}$ is the VSC output voltage. $D=\exp(-T_d s)$ (T_d is the time delay which is small and directly depends on the switching frequency) represents the time delay coefficient of VSC.

From (3-3-3), equations (3-3-4) can be deducted as follows (see the bold variables because they are complex):

$$\begin{aligned}\boldsymbol{i_c} &= \frac{DF_{cc}(s)}{R_f+L_f s+jL_f\omega_b+D(F_{cc}(s)-jL_f\omega_b)}\boldsymbol{i_{cr}} \\ &+ \frac{1-DH_f(s)}{R_f+L_f s+jL_f\omega_b+D(F_{cc}(s)-jL_f\omega_b)}\boldsymbol{v_s}\end{aligned} \tag{3-3-4}$$

When analysing the SSI phenomenon, for the reason that the switching frequency of VSC is high, the time delay of VSC is very small and can be neglected because the bandwidth of D(s) is much higher (≈ kHz) than frequencies of SSI. This means that D(s) ≈ 1 at SSI frequency range. The model can be described as follows:

$$\boldsymbol{i_c} = \underbrace{\frac{F_{cc}(s)}{R_f+L_f s+F_{cc}(s)}}_{G_{cc}(s)}\boldsymbol{i_{cr}} + \underbrace{\frac{1-H_f(s)}{R_f+L_f s+F_{cc}(s)}}_{G_f(s)}\boldsymbol{v}_s \tag{3-3-5}$$

where the transfer functions $G_{cc}(s)$ and $G_f(s)$ characterise the dynamics of inner loop. Considering the complex and real space vectors notation $\boldsymbol{v}=v_d+\mathrm{j}v_q \Leftrightarrow v=[v_d\ v_q]^T$, $\boldsymbol{i_c}=i_{cd}+i_{cq} \Leftrightarrow \boldsymbol{i_c}=[i_{cd}\ i_{cq}]^T$ and $\boldsymbol{i_{cr}}=i_{cdr}+i_{cqr} \Leftrightarrow \boldsymbol{i_{cr}}=[i_{cdr}\ i_{cqr}]^T$, the real transfer model of the CC can be easily derived from (3-1-3) as follows

$$\begin{bmatrix} i_{cd} \\ i_{cq} \end{bmatrix} = \begin{bmatrix} G_{cc}(s) & 0 \\ 0 & G_{cc}(s) \end{bmatrix}\begin{bmatrix} i_{cdr} \\ i_{cqr} \end{bmatrix} + \begin{bmatrix} G_f(s) & 0 \\ 0 & G_f(s) \end{bmatrix}\begin{bmatrix} v_{sd} \\ v_{sq} \end{bmatrix} \tag{3-3-6}$$

$$\begin{aligned} i_{cd} &= G_{cc}(s)i_{cdr} + G_f(s)v_{sd} \\ i_{cq} &= G_{cc}(s)i_{cqr} + G_f(s)v_{sq} \end{aligned} \tag{3-3-7}$$

Since the PLL drives the q-component of the voltage v_{sq} in the converter dq-frame to zero providing the transformation angle θ, and the q-component of the CC reference current i_{cqr} is usually set to zero by assuming that VSC is operating at unity power factor which is common in normal operation conditions. By linearising (3-3-7), the small-signal model of CC can be described as

$$\begin{aligned} \Delta i_{cd} &= G_{cc}(s)\Delta i_{cdr} + G_f(s)\Delta v_{sd} \\ \Delta i_{cq} &= G_{cc}(s)\Delta i_{cqr} + G_f(s)\Delta v_{sq} = G_f(s)\Delta v_{sq} \end{aligned} \tag{3-3-8}$$

b) With inner loop and outer loop

When considering the outer loop as well, the models of the outer loop and the power flows in the AC grid are

$$\begin{aligned} i_{cdr} &= F_{dc}(s)(v_{dc\mathrm{r}} - v_{dc}) \\ P_s &= P_L - (\frac{C}{2}\frac{dv_{dc}{}^2{}_s}{dt}) \\ P_g &=- (v_{sd}i_{cd} + v_{sq}i_{cq}) \end{aligned} \quad (3\text{-}3\text{-}9)$$

where C is the DC capacitance. The variables P_s and P_g are the steady-state operation points of DC output power and the power of the AC transmission line. And the small-signal models of the models above can be expressed as:

$$\begin{aligned} &\Delta i_{cdr} =- F_{dc}(s)\Delta v_{dc} \\ &\Delta i_{cqr} = 0 \\ &\Delta P_s =- sCv_{dc0}\Delta v_{dc} \\ &\Delta P_g =- (v_{sd0}\Delta i_{cd} + i_{sd0}\Delta v_{sd} + v_{sq0}\Delta i_{cq} + i_{cq0}\Delta v_{sq}) \end{aligned} \quad (3\text{-}3\text{-}10)$$

From (3-3-10), (3-3-11) can be derived

$$\begin{aligned} &\Delta v_{dc} = \frac{v_{sd0}G_f(s)+i_{cd0}}{sCv_{dc0}+v_{sd0}G_{cc}(s)F_{dc}(s)}\Delta v_{sd} \\ &\Rightarrow\ \Delta i_{cdr} =- F_{dc}(s)\Delta v_{dc} =- \underbrace{\frac{F_{dc}(s)(v_{sd0}G_f(s)+i_{cd0})}{sCv_{dc0}+v_{sd0}G_{cc}(s)F_{dc}(s)}}_{G_{dc}(s)}\Delta v_{sd} \\ &\begin{bmatrix}\Delta i_{cdr}\\ \Delta i_{cqr}\end{bmatrix} = \begin{bmatrix}- G_{dc}(s) & 0\\ 0 & 0\end{bmatrix}\begin{bmatrix}\Delta v_{sd}\\ \Delta v_{sq}\end{bmatrix} \end{aligned} \quad (3\text{-}3\text{-}11)$$

Where i_{cd0} can be expressed as P_s/v_{d0}. And the model can be finally described as

$$\begin{aligned} \begin{bmatrix}\Delta i_{cd}\\ \Delta i_{cq}\end{bmatrix} &= \begin{bmatrix}G_{cc}(s) & 0\\ 0 & G_{cc}(s)\end{bmatrix}\begin{bmatrix}- G_{dc}(s) & 0\\ 0 & 0\end{bmatrix}\begin{bmatrix}\Delta v_{sd}\\ \Delta v_{sq}\end{bmatrix} \\ &+ \begin{bmatrix}G_f(s) & 0\\ 0 & G_f(s)\end{bmatrix}\begin{bmatrix}\Delta v_{sd}\\ \Delta v_{sq}\end{bmatrix} \\ &= \begin{bmatrix}G_f(s) - G_{cc}(s)G_{dc}(s) & 0\\ 0 & G_f(s)\end{bmatrix}\begin{bmatrix}\Delta v_{sd}\\ \Delta v_{sq}\end{bmatrix} \end{aligned} \quad (3\text{-}3\text{-}12)$$

The transfer function $G_{dc}(s)$ characterises the dynamics of the reference current i_{cdr} due to the change in the VSC input voltage v by considering the outer loop of the DVC.

c) With inner loop, outer loop and PLL

If PLL is considered, the VSC control works with the voltage and current in the converter dq frame $\boldsymbol{v^c_s}= v^c_{sd} +jv^c_{sq} \Leftrightarrow \boldsymbol{v^c_s}=[v^c_{sd}\ v^c_{sq}]^T$, $\boldsymbol{i^c_c}= i^c_{cd} +ji^c_{cq} \Leftrightarrow \boldsymbol{i^c_c} =[\ i^c_{cd}\ i^c_{cq}]^T$ and (3-3-12)must be written as

$$\begin{bmatrix}\Delta i^c_{cd}\\ \Delta i^c_{cq}\end{bmatrix} = \begin{bmatrix}G_f(s) - G_{cc}(s)G_{dc}(s) & 0\\ 0 & G_f(s)\end{bmatrix}\begin{bmatrix}\Delta v^c_{sd}\\ \Delta v^c_{sq}\end{bmatrix} \quad (3\text{-}3\text{-}13)$$

(3-3-14) is derived from (3-3-13)

$$\begin{aligned}
\begin{bmatrix}\Delta i_{cd}\\ \Delta i_{cq}\end{bmatrix} &= \begin{bmatrix}\Delta i_{cd}^{c}\\ \Delta i_{cq}^{c}\end{bmatrix} + \begin{bmatrix}0 & -i_{cq0}G_{pll}(s)\\ 0 & i_{cd0}G_{pll}(s)\end{bmatrix}\begin{bmatrix}\Delta v_{sd}\\ \Delta v_{sq}\end{bmatrix}\\
&= \begin{bmatrix}G_f(s) - G_{cc}(s)G_{dc}(s) & 0\\ 0 & G_f(s)\end{bmatrix}\begin{bmatrix}\Delta v_{sd}^{c}\\ \Delta v_{sq}^{c}\end{bmatrix} + \begin{bmatrix}0 & -i_{cq0}G_{pll}(s)\\ 0 & i_{cd0}G_{pll}(s)\end{bmatrix}\begin{bmatrix}\Delta v_{sd}\\ \Delta v_{sq}\end{bmatrix}\\
&= \begin{bmatrix}G_f(s) - G_{cc}(s)G_{dc}(s) & 0\\ 0 & G_f(s)\end{bmatrix}\begin{bmatrix}1 & 0\\ 0 & 1 - v_{sd0}G_{pll}(s)\end{bmatrix}\begin{bmatrix}\Delta v_{sd}\\ \Delta v_{sq}\end{bmatrix}\\
&+ \begin{bmatrix}0 & -i_{cq0}G_{pll}(s)\\ 0 & i_{cd0}G_{pll}(s)\end{bmatrix}\begin{bmatrix}\Delta v_{sd}\\ \Delta v_{sq}\end{bmatrix}
\end{aligned} \tag{3-3-14}$$

The model can be finally described as

$$\begin{aligned}
&\begin{bmatrix}\Delta i_{cd}\\ \Delta i_{cq}\end{bmatrix} = \begin{bmatrix}Y_{v,dd}(s) & 0\\ 0 & Y_{v,qq}(s)\end{bmatrix}\begin{bmatrix}\Delta v_{sd}\\ \Delta v_{sq}\end{bmatrix}\\
&Y_{v,dd}(s) = G_f(s) - G_{cc}(s)G_{dc}(s)\\
&Y_{v,qq}(s) = G_f(s)(1 - v_{sd0}G_{pll}(s)) - \left\{\frac{P_{s0}}{v_{sd0}}\right\}G_{pll}(s)
\end{aligned} \tag{3-3-15}$$

where $P_{s0}=-i_{cd0}v_{sd0}$. The transfer function $G_{pll}(s)$ describes the dynamics of the PLL as

$$G_{pll}(s) = \frac{F_{pll}(s)}{s + v_{sd0}F_{pll}(s)} \tag{3-3-16}$$

where $F_{pll}(s)=k_{p\_pll}+k_{p\_pll}/s$ is the proportional-integral controller of the PLL. So, the impedance model of VSC can be finally expressed as

$$\begin{aligned}
&Z_{vsc}(s) = \frac{\Delta \boldsymbol{v_s}}{\Delta \boldsymbol{i_c}} = \begin{bmatrix}Z_{v,dd}(s) & 0\\ 0 & Z_{v,qq}(s)\end{bmatrix}\\
&Z_{v,dd}(s) = \left(Y_{v,dd}(s)\right)^{-1}\\
&Z_{v,qq}(s) = \left(Y_{v,qq}(s)\right)^{-1}
\end{aligned} \tag{3-3-17}$$

So, the VSC impedance model can be finally obtained that

3) Grid-connected VSC model

The dynamic equations of the grid in the *dq*-frame with the VSC input voltage *v* and current *i* are

$$v_g = \begin{bmatrix}v_{gd}\\ v_{gq}\end{bmatrix} = \underbrace{\begin{bmatrix}Z_{g,dd}(s) & Z_{g,dq}(s)\\ Z_{g,qd}(s) & Z_{g,qq}(s)\end{bmatrix}}_{Z_{grid}(s)} i_c + v_s \tag{3-3-18}$$

For a symmetric system, it can be concluded that $Z_{g,dd}(s)=Z_{g,qq}(s)$ and $Z_{g,dq}(s)=-Z_{g,qd}(s)$. In particular, transformers and medium and high voltage lines can be modelled as R-L circuits at SSI frequencies (equivalent shunt capacitors are neglected in line models) and the impedance matrix of these components is

$$Z_{grid}(s) = \begin{bmatrix}R_g + L_g s & -L_g\omega_{\mathrm{b}}\\ L_g\omega_{\mathrm{b}} & R_g + L_g s\end{bmatrix} \tag{3-3-19}$$

where $\omega_b = 2\pi f_b$ (f_b=50Hz) is the fundamental angular frequency of the grid. The impedance matrix of the grid commonly presents the same structure as $Z_{grid}(s)$.

The impedance-based equivalent circuit of the grid-connected VSC system is obtained by replacing the WTGs in Fig. 3.1 with $Z_{vsc}(s)$ (3-3-17) and characterising the grid as the voltage source v_g in series with the equivalent impedance matrix $Z_{grid}(s)$ (3-3-19). The small-signal dynamics of grid-connected VSC system can be analysed from the expression:

$$\Delta i_c = \underbrace{\left(Z_{vsc}(s) + Z_{grid}(s)\right)^{-1}}_{Y_{sys}(s)=Z_{sys}^{-1}(s)} \Delta v_s = \left(1 + \underbrace{Z_{vsc}^{-1}(s) Z_{grid}(s)}_{L(s)}\right)^{-1} Z_{vsc}^{-1}(s) \Delta v_s \qquad (3\text{-}3\text{-}20)$$

3.4 Validation of impedance model by time-domain simulations

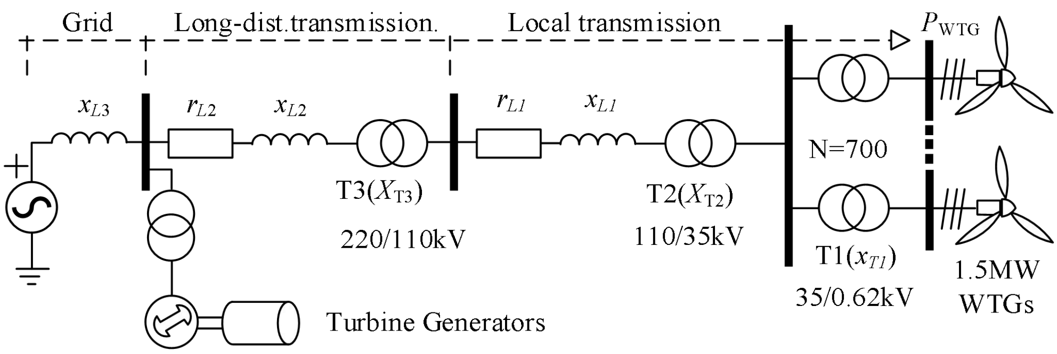

Fig. 3.7. The example of the studied system model.

To validate the proposed linearised model, an example of WTGs connected to a weak AC grid which reflects the SSI scenario observed in the actual installation in [32] is analysed. The example has N (number) = 700 identical PMSG type-4 WTGs of rated power $P_{WTG,\ rated}$ = 1.5 MW connected through a local and a long-distance transmission lines to the main grid (see Fig. 3.7). It is assumed that the WTGs operate under a similar operating point and the possible turbine generators connected to the main grid are shut down, which are actual conditions of the detected SSI [88]. The data of the AC grid and the WTG VSCs are shown in Table B-1 and Table B-2 in Appendix B, respectively. The electrical parameters of the AC grid in [88] are expressed in per unit value with S_B = 1500 MVA.

For the purpose of illustration, a typical scenario is considered in the PSCAD simulation. WTG is equivalent to a VSC connected to a controlled current source.

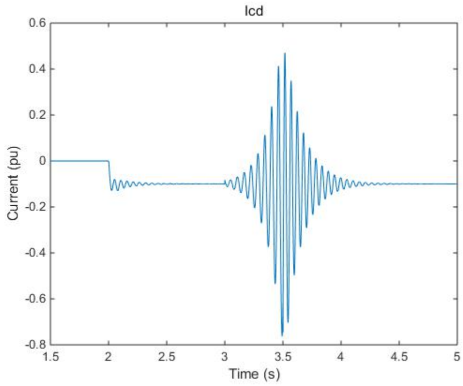
Icd
Current (pu)
Time (s)

a)

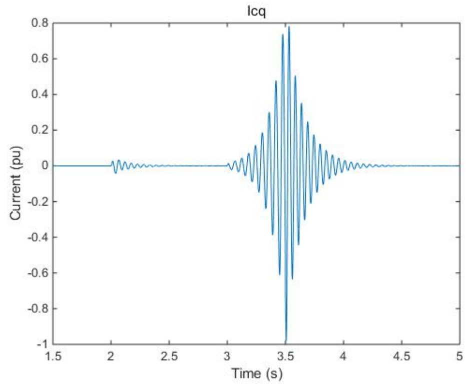
Icq
Current (pu)
Time (s)

b)

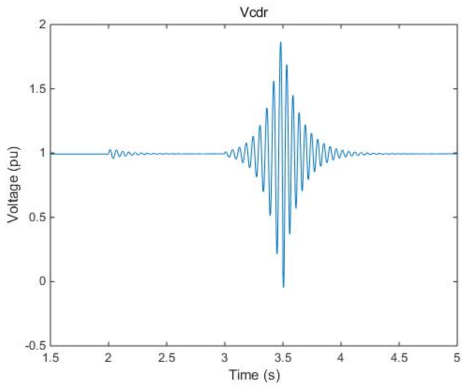
Vcdr
Voltage (pu)
Time (s)

c)

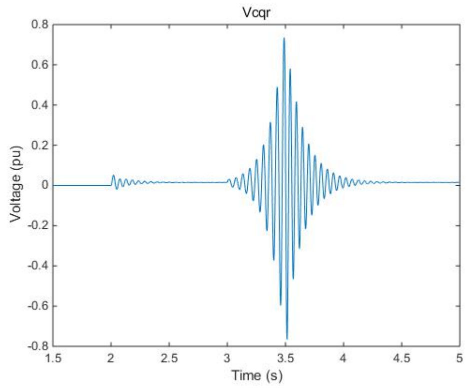
Vcqr
Voltage (pu)
Time (s)

d)

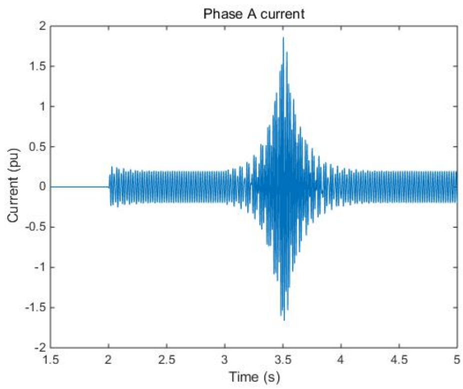
Phase A current
Current (pu)
Time (s)

e)

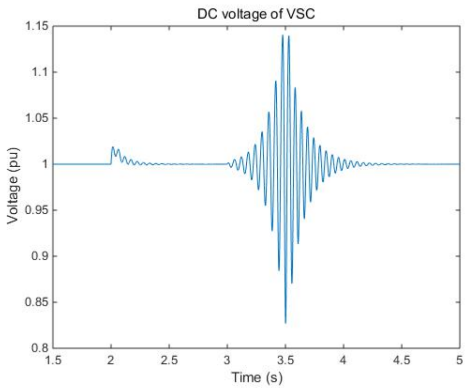
DC voltage of VSC
Voltage (pu)
Time (s)

f)

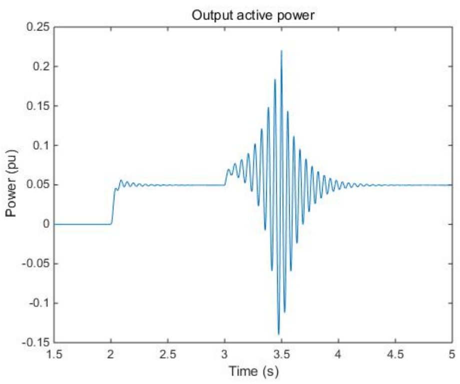
Output active power
Power (pu)
Time (s)

g)

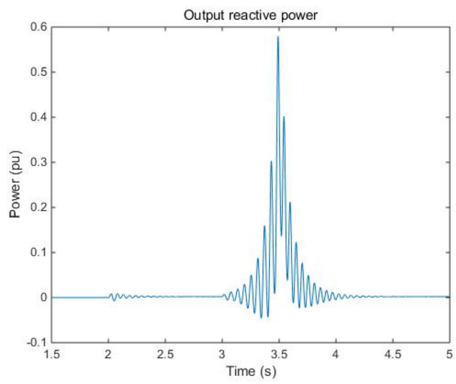
Output reactive power
Power (pu)
Time (s)

h)

Fig. 3.8. Simulation results of the reference scenario a) d-axis component of current i_{cd}. b) q-axis component of current i_{cq}. c) d-axis component of reference voltage v_{cdr}. d) q-axis component of reference voltage v_{cqr}. e) Phase A current. f) DC voltage v_{dc}. g) Output active power. h) Output reactive power.

Fig. 3.8 presents the waves of d-axis component of current i_{cd}, q-axis component of current i_{cq}, d-axis component of reference voltage v_{cdr}, q-axis component of reference voltage v_{cqr}, phase A current, DC voltage v_{dc}, total output active power and total output reactive power respectively. Initially, 500 equivalent WTGs are connected, and the output active power is raised from 0% to 10% at 2s and the system is stable between 2s and 3s. Clearly, sustained oscillation appears when the number of WTGs is increased to 700, which is the SSI scenario in [88]. At this time, the AC grid has a low value of SCR equal to 1.34. The equation of SCR expressed as follows:

$$SCR = \frac{S_B/x_\Sigma}{N \cdot P_{WTG,rated}}, \tag{3-4-1a}$$

$$x_\Sigma = x_{L1} + x_{L2} + x_{T2} + x_{T3} \tag{3-4-1b}$$

After the number of WTGs is decreased from 700 to 500 at 3.5s, the SSI is suppressed, and the system becomes stable again.

Eigenvalue analysis of the impedance linear model when the number of connected WTGs is equal to 700 is shown in Fig. 3.9 a). Clearly, there exists a pair of conjugate eigenvalues with their frequency located in the subsynchronous range (17.8Hz), and the real parts of the eigenvalues are positive, meaning the SSI occurs and the system is unstable. The Fast Fourier Transform (FFT) result of phase A current in time-domain simulation by PSCAD is presented in Fig. 3.9 b), the frequency of the subsynchronous component of phase A current with maximum amplitude is around 17Hz (the amplitude of the current component at this frequency is about 0.0792026 pu). The SSI frequency calculated by eigenvalue analysis in MATLAB is similarly with the oscillation frequency detected from the FFT module of PSCAD in time-domain simulation that verifies the correctness of the impedance model.

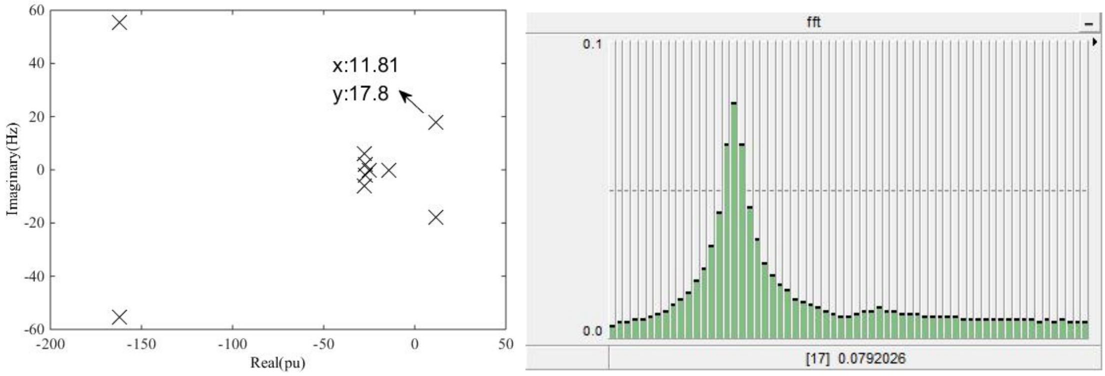

a) b)

Fig. 3.9. Stability analysis. a) Eigenvalue analysis, b) FFT in PSCAD.

3.5 Summary

This chapter built and analysed the state-space model and impedance model of the single VSC connected to an AC grid system. Both models are linearised which is available to assess system stability theoretically. Compared with the impedance model, the deduction of the state-space model is complicated and requires detailed information for all elements in the system, which is not always completely available, so the impedance model is finally utilised for further analysis. A proposed base case was investigated by the eigenvalue analysis of the impedance linear model in MATLAB and then validated in the nonlinear model in PSCAD time-domain simulation. The results verify the correctness and practicability of the impedance model.

Chapter 4

SSI in single VSC connected to an AC grid

4.1 Introduction

The analysis in the previous chapter shows that the SSI characteristics in the model of a single VSC connected to AC system are affected by several parameters of the VSC control system and the power grid. Based on the proposed impedance model, this chapter introduces three criteria: Generalised Nyquist criterion (GNC), eigenvalue analysis, and determinant-impedance criterion, to assess the system stability and analyse the influence of the inner loop, outer loop and PLL of the VSC control system on the stability of the system. The mechanism of SSI is investigated based on the closed-loop transfer function method.

4.2 Three stability criteria based on impedance analysis

Three stability criteria of impedance analysis are used in this chapter to analyse SSI namely GNC, eigenvalue analysis, and determinant-impedance criterion.

4.2.1 GNC

In the frequency domain, GNC is a useful alternative criterion based on the traditional Nyquist criterion [128]. Theory for complex space vectors which have long been used to model ac machines, usually in time-domain. By applying the Laplace transform to such a model, the corresponding complex transfer function is obtained. Not as frequently used as space vectors, complex transfer functions permit frequency-domain analysis, which is useful for current controllers and filters. The main theory and explanation of the GNC are described as follows.

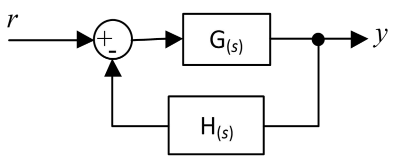

Fig. 4.1. Grid-connected VSC system model.

Considering Fig. 4.1, where the closed-loop system from ***r*** to ***y*** is given by $G_c(s) = G(s)/[1 + G_k(s)]$ and where $G_k(s) = G(s)H(s)$ is the open-loop system.

1) In symmetric systems, assuming $G_k(s)$ has no right-half plane poles, $G_c(s)$ is asymptotically stable if and only if the Nyquist curve of $G_k(s)$ does not encircle -1 for $s = j\omega$, $-\infty < \omega < \infty$.

When replacing the complex transfer functions in Fig. 4.1 by the respective transfer matrices G(s) and H(s), the stability of the closed-loop system from ***r*** to ***y***, i.e., $G_c(s)= [I + G_k(s)]^{-1} G(s)$ and $G_k(s) = G(s)H(s)$, can be analysed using the multivariable Nyquist criterion and also when $G_k(s)$ is unsymmetric. Then theorem 2 can be obtained as follows:

2) In asymmetric systems, assuming $G_k(s) = \begin{bmatrix} G_{kdd}(s) & -G_{kqd}(s) \\ G_{kdq}(s) & G_{kqq}(s) \end{bmatrix}$ has no right-half-plane poles, $G_c(s)$ is asymptotically stable if and only if the characteristic loci (Nyquist curves) for the eigenvalues of $G_k(s)$, i.e.,

$$\det[\lambda_i(s)I - G_k(s)] = 0 \quad (i = 1, 2) \quad \Rightarrow \lambda_{1,2}(s) = \frac{G_{k_{dd}}(s)+G_{k_{qq}}(s)}{2} \pm \sqrt{\left(\frac{G_{k_{dd}}(s)-G_{k_{qq}}(s)}{2}\right)^2 + G_{k_{dq}}(s)G_{k_{qd}}(s)} \tag{4-1-1}$$

taken together, do not encircle −1 for s = jω, $-\infty < \omega < \infty$. The GNC extends the traditional Nyquist criterion to the Nyquist curves of the eigenvalues of $L(s)$ [21], i.e.,

$$\det[\lambda_i(s)I - L(s)] = 0 \quad (i = 1, 2) \quad \Rightarrow \lambda_{1,2}(s) = \frac{L_{dd}(s)+L_{qq}(s)}{2} \pm \sqrt{\left(\frac{L_{dd}(s)-L_{qq}(s)}{2}\right)^2 + L_{dq}(s)L_{qd}(s)} \tag{4-1-2}$$

Although GNC is commonly used, it does not allow analysing system stability in detail because it only provides qualitative results.

4.2.2 Eigenvalue analysis

Eigenvalue analysis is based on the linear system model at the stable operation point. When the linear impedance matrix of the system is obtained, the eigenvalues of its matrix can be calculated which are the poles of the equivalent closed-loop system. Then system stability can be assessed by the positions of eigenvalues on complex planes. The theory of eigenvalue analysis is rigorous and the physical concept is clear. However, its applicability in the large-scale system is limited since the order of the linear impedance matrix of the system is high, and the elements in the system matrix could be also a multi-order matrix that increases the difficulty to calculate the determinant of the system matrix to obtain the poles.

4.2.3 Determinant-impedance criterion

A criterion based on the determinant-impedance criterion of the system impedance matrix is recently proposed in [8] to overcome the drawbacks of the previous approaches as follows. If a disturbance voltage source $\boldsymbol{V}(s)$ of the SSI mode is injected into the AC system, a current of the same mode can be produced and expressed by $\boldsymbol{I}(\mathrm{s})=\boldsymbol{V}(\mathrm{s})\boldsymbol{Z}^{-1}(s)$. Then the system stability can be assessed by the poles of $\boldsymbol{Z}^{-1}(s)$ which are also the zeroes of the determinant of $\boldsymbol{Z}(s)$, namely $D_{\mathrm{Y}}(s)$. Considering the difficulty to determine the zeros of $D_{\mathrm{Y}}(s)$ in actual systems due to their high order, the determinant-impedance characteristic stability criterion assesses the oscillatory stability of the poorly damped zeros of $D_{\mathrm{Y}}(s)$ by analysing its frequency-domain plot. If $z_o = \sigma_o \pm j\omega_o$ are a pair of conjugate zeros of $D_{\mathrm{Y}}(s)$, the frequency-domain representation of $D_{\mathrm{Y}}(s)$ can be expressed as follows:

$$D(j\omega) = (j\omega - z_o)(j\omega - z_o^*)H(j\omega), \tag{4-2-1}$$

which can be approximated in a small neighbourhood of ω_o as

$$D(j\omega) \approx (\sigma_o^2 + \omega_o^2 - \omega^2 - j2\omega\sigma_o)H(j\omega_o) = \underbrace{H_r(\sigma_o^2 \quad + \omega_o^2 \quad - \omega^2) + 2H_x\omega\sigma_o}_{D_r(\omega)} +$$

$$j\underbrace{(H_x(\sigma_o^2 \quad + \omega_o^2 \quad - \omega^2) - 2H_r\omega\sigma_o)}_{D_x(\omega)}, \tag{4-2-2}$$

by assuming that $H(j\omega) \approx H(j\omega_o) = H_r + jH_x$ with H_r and H_x constant values. The zero-crossing frequencies ωr and ωx of the real and imaginary parts of $D(j\omega)$ are obtained from the maximum value of solving $D_r(j\omega)=0$ and $D_x(j\omega)=0$, respectively.

$$\begin{aligned} \omega_r &= \mathrm{m}\left\{\frac{H_x}{H_r}\sigma_o \pm \sqrt{\left(\frac{H_x}{H_r}\sigma_o\right)^2 + (\sigma_0^2 + \omega_o^2)}\right\} \\ \omega_x &= \mathrm{m}\left\{-\frac{H_r}{H_x}\sigma_o \pm \sqrt{\left(\frac{H_r}{H_x}\sigma_o\right)^2 + (\sigma_0^2 + \omega_o^2)}\right\}, \end{aligned} \tag{4-2-3}$$

where the function max $\{\cdot\}$ returns the larger and positive zero-crossing frequencies which are the feasible solutions.

According to (4-2-3), the poorly damped zeros (i.e., the zeros with $|\sigma_o| \ll |\omega_o|$) can be recognised from the frequency-domain plots of D_r and D_x because ω_r and ω_x are very close. Moreover, the zero-crossing frequencies ω_r and ω_x approximately match with the oscillatory mode of these zeros, i.e., $\omega_r \approx \omega_x \approx \omega_o$. The zero-crossing frequency that best approximates the subsynchronous oscillation frequency ω_o depends on the ratio between H_r and H_x: If $H_r < H_x$, $\omega_o \approx \omega_x$, otherwise $\omega_o \approx \omega_r$. Subsequently, the system stability, characterised by the sign of σ_o, is assessed from the real or imaginary part of $D(j\omega)$ depending on the ratio between H_r and H_x and considering the poorly damped zero assumption $|\sigma_o| \ll |\omega_o|$:

1) If $H_r<H_x$, the real part of $D(j\omega)$ at ω_x can be approximated as

$$D_r(\omega_x) \approx -k_x\sigma_o \tag{4-2-4}$$

where k_x is the slope of $D_x(\omega)$ at ω_x, i.e,

$$k_x = \left[\frac{dD_x(\omega)}{d\omega}\right]_{\omega=\omega_x} \approx -2H_x\omega_x \tag{4-2-5}$$

Therefore, the system is stable (i.e., $\sigma_o<0$) if $D_r(\omega_x)$ is positive when k_x is positive or if $D_r(\omega_x)$ is negative when k_x is negative.

2) If $H_r>H_x$, the imaginary part of $D(j\omega)|$ at ω_r can be approximated as follows

$$D_x(\omega_r) \approx k_r\sigma_o \tag{4-2-6}$$

where k_r is the slope of $D_r(\omega)$ at ω_r, i.e.

$$k_r = \left[\frac{dD_r(\omega)}{d\omega}\right]_{\omega=\omega_r} \approx -2H_r\omega_r \tag{4-2-7}$$

Therefore, the system is stable (i.e., $\sigma_o<0$) if $D_x(\omega_r)$ is positive when k_r is negative or if $D_x(\omega_r)$ is negative when k_r is positive.

4.3 Influence factors analysis utilising different criteria

The influence of system parameters on system stability is analysed in several cases. These parameters are classified into electrical (e.g., grid components) and control parameters. Control parameters are divided into feed-forward voltage low-pass filter, current loop, outer loop and PLL of VSC because they have different time constants, and therefore their influence on stability may be different. Stability is assessed from the poles of the closed-loop system, the GNC and the determinant-impedance criterion. The study is also validated from PSCAD/EMTDC time-domain simulations.

4.3.1 Reference case

The example system of WTGs connected to weak AC grids proposed in Fig. 3.7 is analysed. An unstable reference case is analysed when 600 WTGS are connected, the parameters of AC grid and VSC control system are corresponding to the data in Table B-1 and Table B-2 in Appendix B, SSI instabilities are mainly due to the interaction between VSC and AC grid, and they need to be studied from the system matrix impedance model due to the asymmetries introduced in the VSC model. In this case, the stability of grid-connected VSC systems is usually assessed by either determining the poles of the closed-loop system (the eigenvalues of the system), applying the GNC to the system open-loop transfer matrix or by determinant criterion.

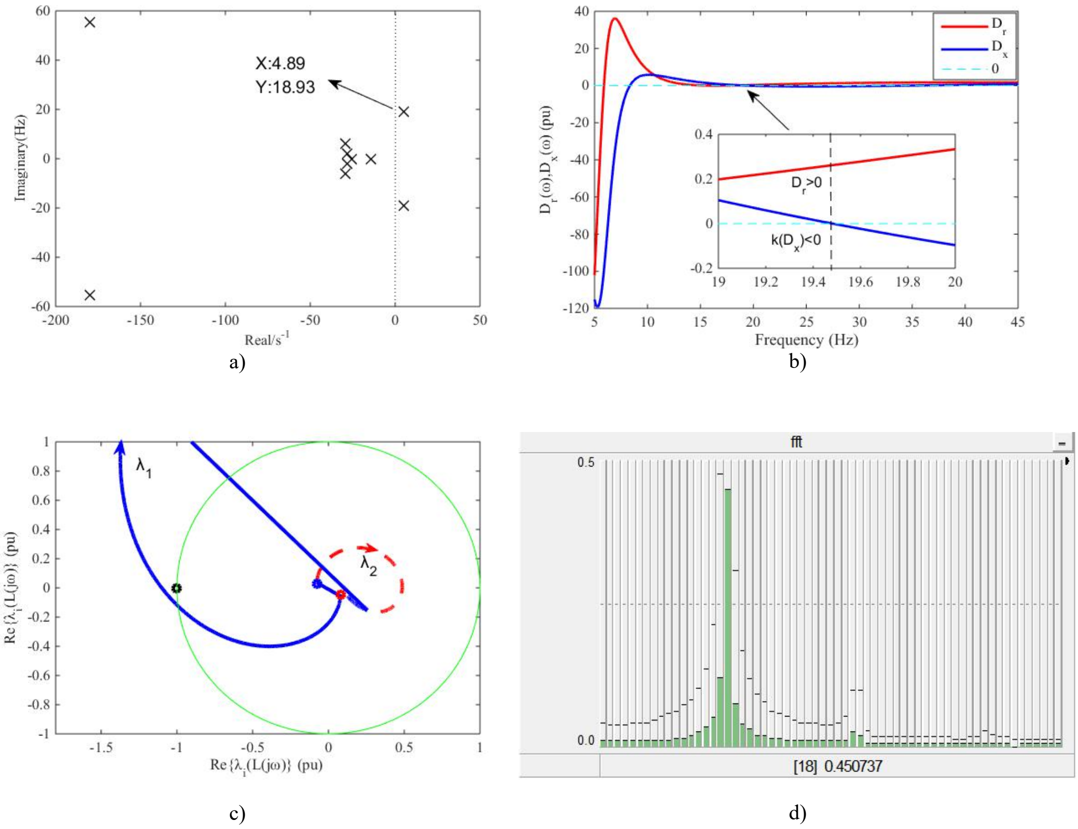

Fig. 4.2. Stability studies of the reference case a) Eigenvalue analysis. b) Determinant-impedance criterion. c) GNC. d) FFT analysis of phase A current in PSCAD time-domain simulations.

Stability analysis results of the reference case are shown in Fig. 4.2. In Fig. 4.2. a), the system has a pair of poorly damped conjugate poles, $z_o = 4.89 \pm j(2\pi \cdot 18.93)$, with their frequencies located in the subsynchronous range and positive real parts meaning that the system at this frequency is unstable. In Fig. 4.2 b), the determinant-impedance criterion predicts the instability because, in the neighbourhood of the previous poorly damped poles, the slope of $D_x(\omega_x)$ is negative, $k(D_x) < 0$, and $D_r(\omega_x)$ is positive, $D_r(\omega_x) > 0$, at the zero-crossing frequency of $D_x(\omega_x)$ =19.48 Hz. Note that the above frequency approximates the SSI frequency of the unstable poles. According to Fig. 4.2 c), the GNC allows verifying the results on instability because the curve of the eigenvalue λ_1 encircles the $(-1,0)$ point in a clockwise direction. The code of the analysis process in MATLAB is shown in Appendix C.

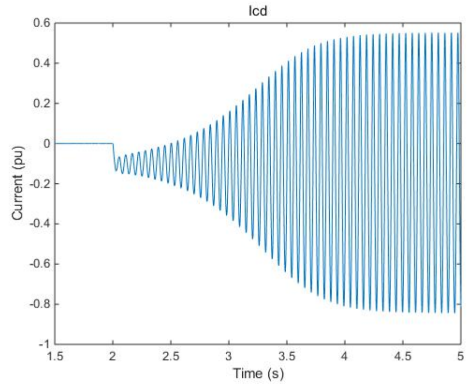
Icd
Current (pu)
Time (s)

a)

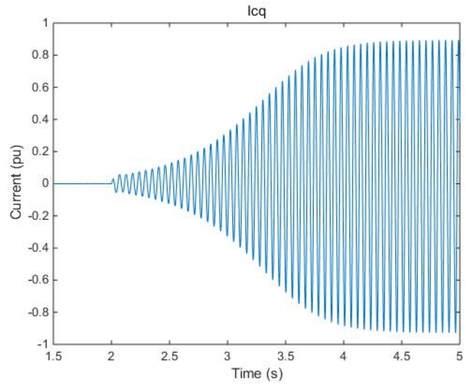
Icq
Current (pu)
Time (s)

b)

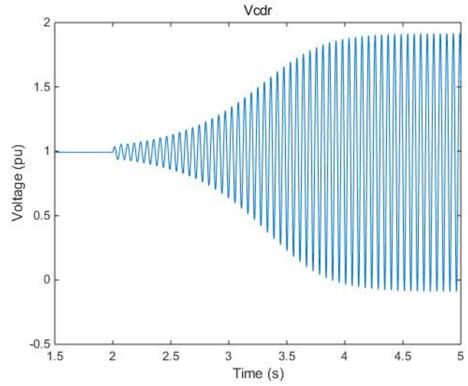
Vcdr
Voltage (pu)
Time (s)

c)

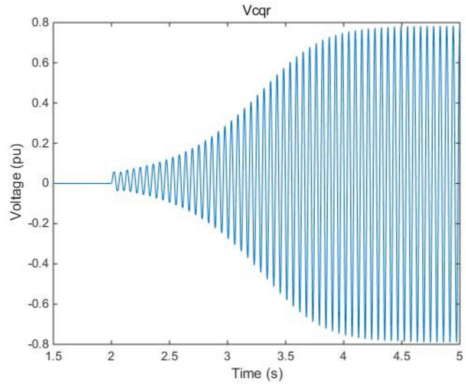
Vcqr
Voltage (pu)
Time (s)

d)

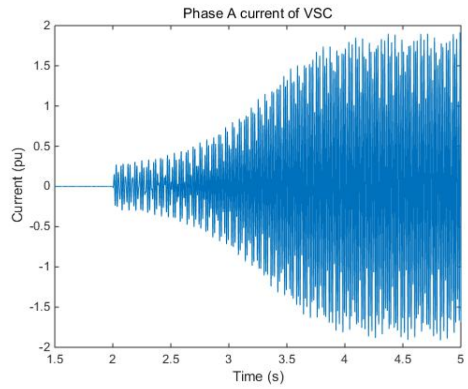
Phase A current of VSC
Current (pu)
Time (s)

e)

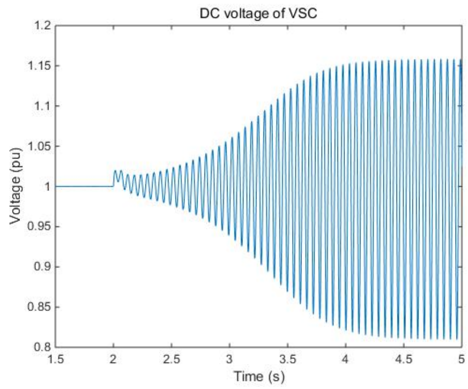
DC voltage of VSC
Voltage (pu)
Time (s)

f)

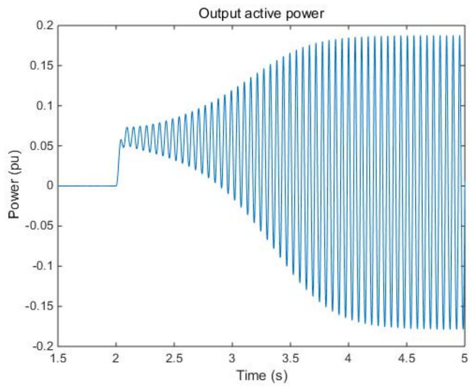
Output active power
Power (pu)
Time (s)

g)

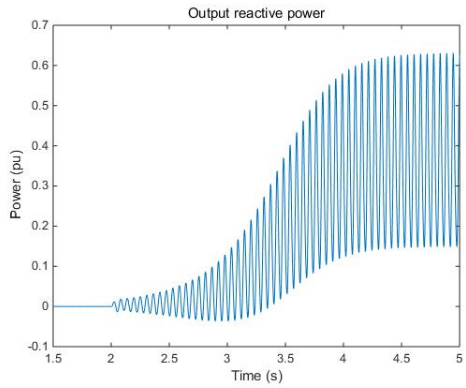
Output reactive power
Power (pu)
Time (s)

h)

Fig. 4.3. Dynamics of the VSC in time-domain simulation of the reference case, a) d-axis component of current i_{cd}. b) q-axis component of current i_{cq}. c) d-axis component of reference voltage v_{cdr}. d) q-axis component of reference voltage v_{cqr}. e) Phase A current. f) DC voltage v_{dc}. g) Output active power. h) Output reactive power.

From the stability study results by using eigenvalue analysis, GNC and determinant criterion. The comparisons of them are concluded as follows:

Determinant-impedance criterion is a practical approach to address SSI concerns because it allows easily quantifying the oscillatory stability by observing the frequency plots (real and imaginary parts) of the determinant of the system impedance matrix, which does not require detailed information for all elements in the system. However, the accuracy of the determinant-impedance criterion is to predict the oscillation frequency is lower than eigenvalue analysis. GNC can also clearly assess system stability, but GNC can only show qualitative results which is difficult to provide a stable region. Eigenvalue analysis is a useful tool to analyse the impact of system and control parameters on stability by determining the poles of the closed-loop system matrix. It has advantages compared with other criteria when assessing the stability of single VSC connected to an AC system such as obtaining system stability region and predicting oscillation frequency accurately. The limitation of eigenvalue analysis is mostly in high-order dynamic models for large systems which is difficult to obtain the poles of the closed-loop system by calculating the determinant value.

4.3.2 Effect of the strength of AC grid

The equation of short circuit ratio (SCR) is expressed as follows:

$$SCR = \frac{S_B/x_\Sigma}{N \cdot P_{WTG,rated}}, \tag{4-3-1a}$$

$$x_\Sigma = F_X * (x_{L1} + x_{L2} + x_{T2} + x_{T3}) \tag{4-3-1b}$$

where S_B is the base frequency, x_Σ is the line reactance, $P_{WTG,\ rated}$ is the rated power of one WTG, N represents the number of connected WTGs and F_X is a coefficient of the reactance in order to change the value of line reactance in case studies. When the product of N and F_x is as a constant value, the SCR will not change. Eigenvalue analysis results of five cases are shown in Fig. 4.4 to study system stability when SCR=1.56 but with different N and F_x, which are: Case1 (N=600, F_x =1), Case2 (N=500, F_X=1.2), Case3 (N=400, F_X=1.5), Case4 (N=300, F_X=2), Case5 (N=200, F_X=3). The eigenvalues are nearly same which indicating that it is SCR related to system stability instead of the ratio between number of WTGs and F_X.

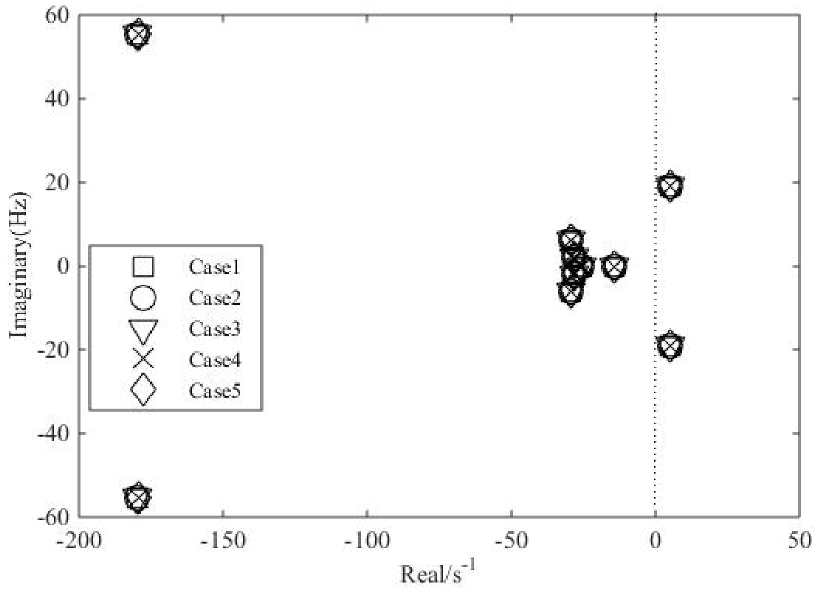

Fig.4.4. Eigenvalue analysis of the reference case.

1) Changing SCR with different numbers of connected WTGs

Stability study of the case of changing SCR with different numbers of connected WTGs is shown in Fig. 4.5. From Fig. 4.5 a), as the numbers of connected WTGs N increases from 400 to 1000 which means SCR decreases, the real part of the eigenvalue changes from negative to positive. In other words, the system will become unstable when the AC grid is becoming weaker, and the stable region is N<545. Moreover, increased SCR leads to a decrease of the oscillation frequency. Fig. 4.5 b) shows the stable result when N=500 by using GNC because the curves of the eigenvalues λ_1 and λ_2 do not encircle the $(-1,0)$ point. In Fig. 4.5 c), the determinant-impedance criterion predicts the system is stable when N=500 because, in the neighbourhood of the previous poorly damped poles, the slope of $D_x(\omega_x)$ and the value of $D_r(\omega_x)$ are both negative at the zero-crossing frequency of $D_x(\omega_x)$ =19.63 Hz.

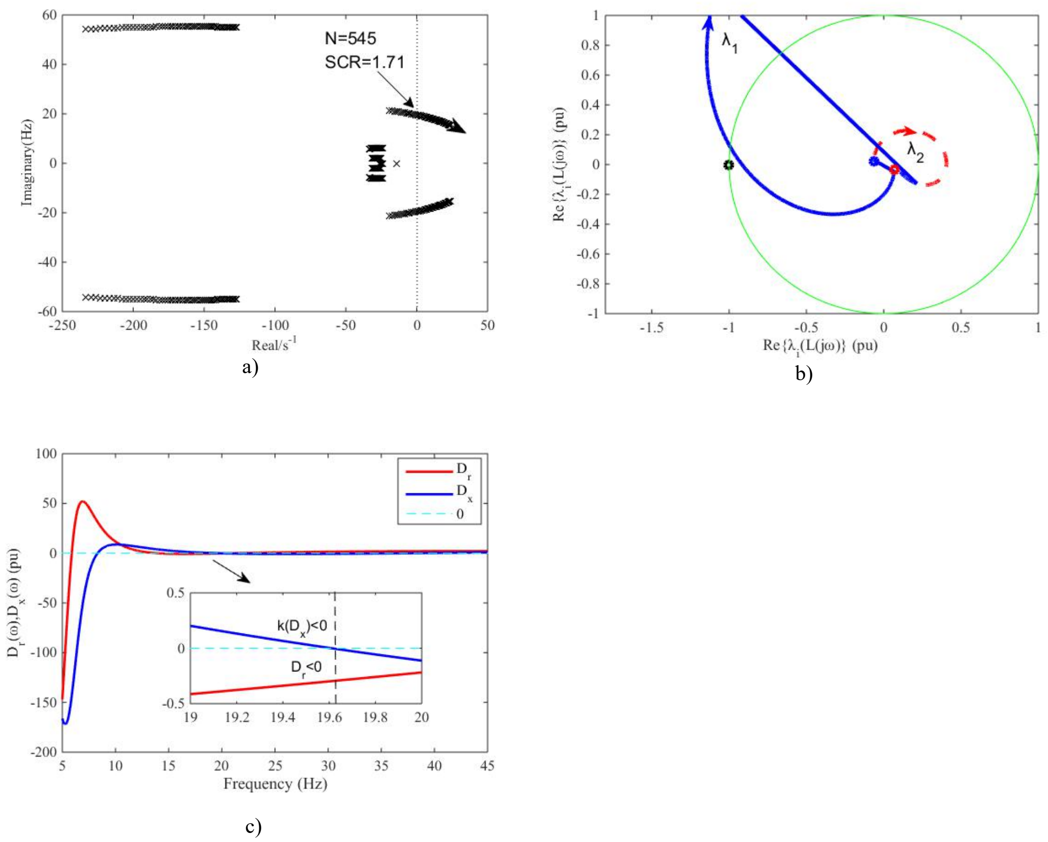

Fig. 4.5. Stability study of the case with different numbers of connected WTGs a) Eigenvalue analysis. b) GNC. c) Determinant-impedance criterion.

Dynamics of the VSC in the time-domain simulation of the case when changing SCR with different numbers of connected WTGs are shown in Fig. 4.6. N=600 initially and after the WTG output active power P_{WTG} increases from zero to 10% of $P_{WTG,\ rated}$ at 2 s, the system becomes unstable. Since the number of WTGs decreased from 600 to 500 (SCR=1.87) at 5s, the system becomes stable. The simulation results are consistent with previous stability analysis results.

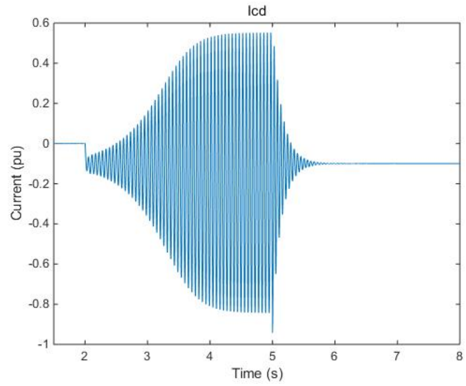
Icd
Current (pu)
Time (s)

a)

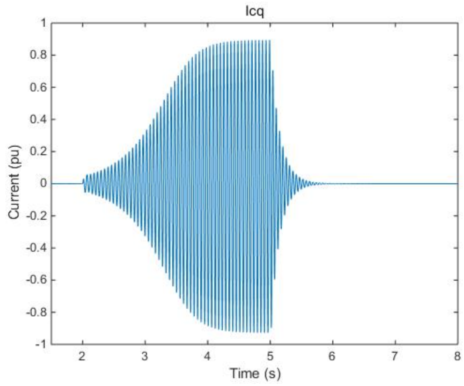
Icq
Current (pu)
Time (s)

b)

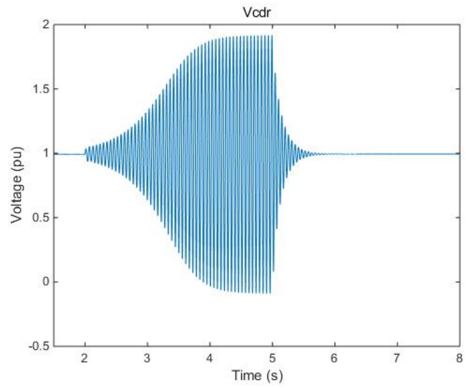
Vcdr
Voltage (pu)
Time (s)

c)

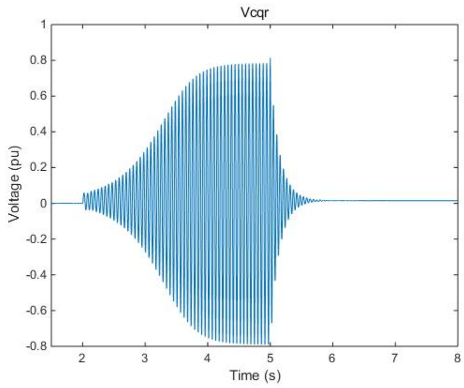
Vcqr
Voltage (pu)
Time (s)

d)

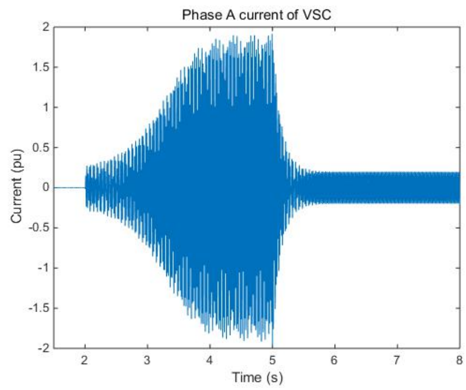
Phase A current of VSC
Current (pu)
Time (s)

e)

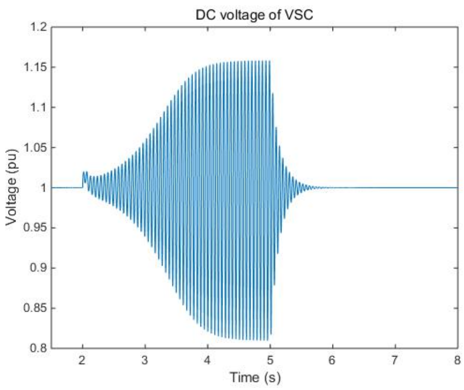
DC voltage of VSC
Voltage (pu)
Time (s)

f)

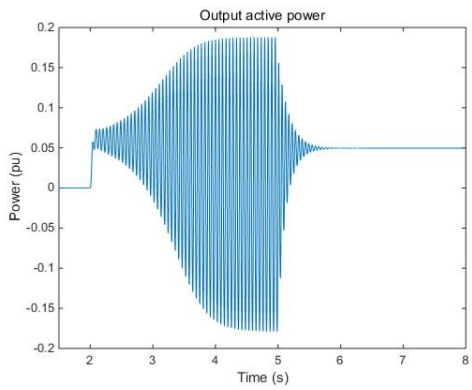
Output active power
Power (pu)
Time (s)

g)

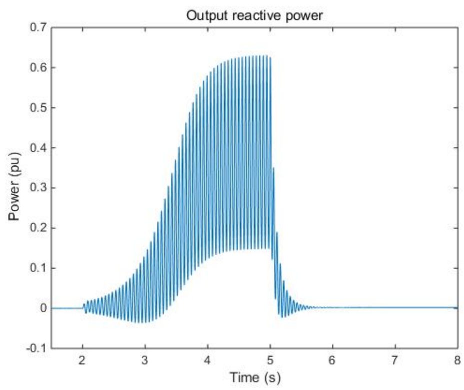
Output reactive power
Power (pu)
Time (s)

h)

Fig. 4.6. Dynamics of the VSC in the time-domain simulation of the case when changing SCR with different numbers of connected WTGs. a) d-axis component of current i_{cd}. b) q-axis component of current i_{cq}. c) d-axis component of reference voltage v_{cdr}. d) q-axis component of reference voltage v_{cqr}. e) Phase A current. f) DC voltage v_{dc}. g) Output active power. h) Output reactive power.

2) Changing SCR with various line reactance

From Fig. 4.7 a), as the coefficient of line reactance F_X increases from 0.4 to 1.4 which means SCR decreases, a pair of eigenvalues move from the left half-plane to the right half-plane, indicating system stability is decreased. And oscillation frequency is also decreased with the increment of F_X. The stable region is F_X <1.1 which means SCR>1.71. Fig. 4.7 b) and Fig. 4.7 c) are the case of F_X =0.83 in GNC and determinant criterion respectively. The GNC allows verifying the stable results because the curves of the eigenvalues λ_1 and λ_2 do not encircle the (−1,0) point. And the determinant-impedance criterion predicts the system is stable because, in the neighbourhood of the previous poorly damped poles, the slope of $D_x(\omega_x)$ is negative, $k(D_x) < 0$, and $D_r(\omega_x)$ is negative, $D_r(\omega_x) < 0$, at the zero-crossing frequency of $D_x(\omega_x)$ =19.63 Hz.

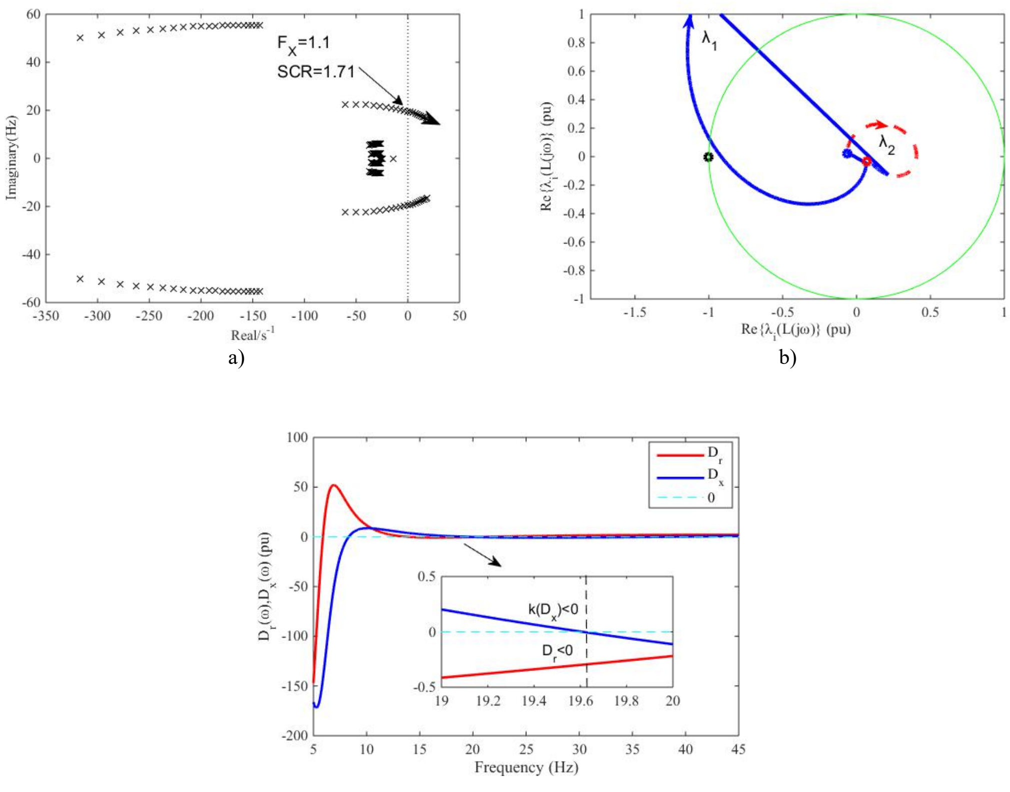

c)

Fig. 4.7. Stability study of the case when changing SCR with various line reactance. a) Eigenvalue analysis. b) GNC. c) Determinant-impedance criterion.

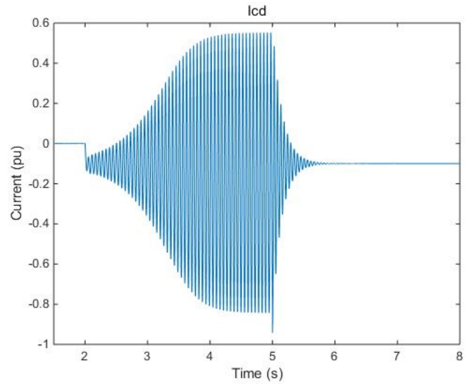
Icd
Current (pu)
Time (s)

a)

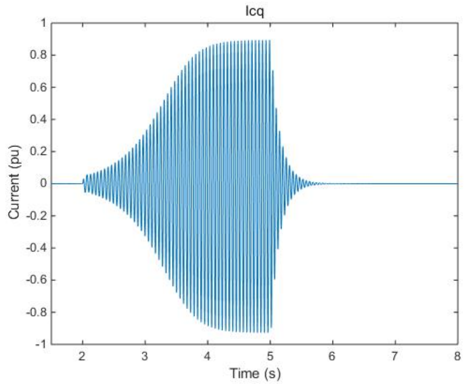
Icq
Current (pu)
Time (s)

b)

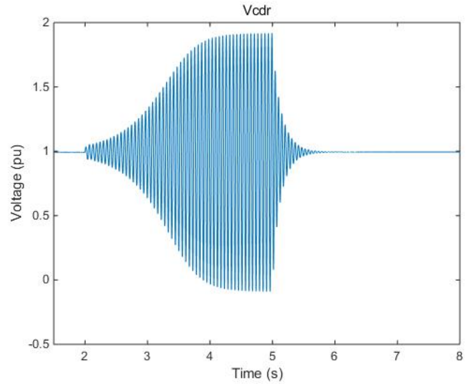
Vcdr
Voltage (pu)
Time (s)

c)

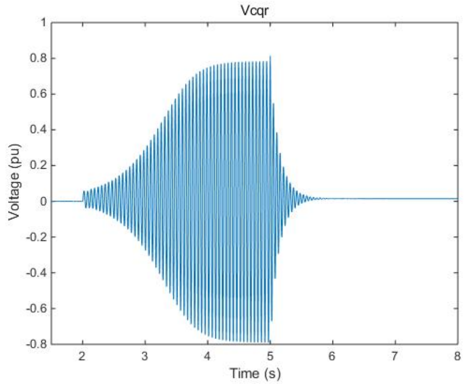
Vcqr
Voltage (pu)
Time (s)

d)

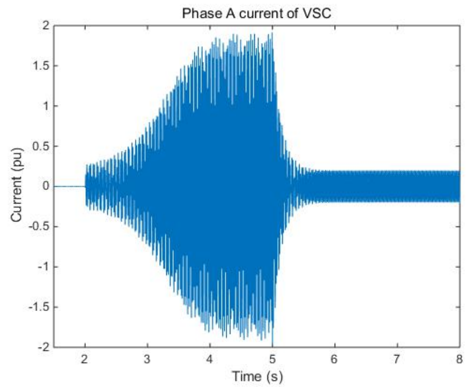
Phase A current of VSC
Current (pu)
Time (s)

e)

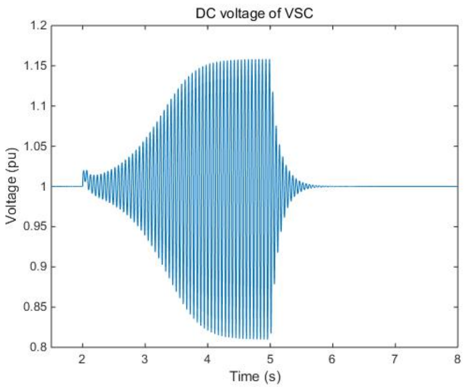
DC voltage of VSC
Voltage (pu)
Time (s)

f)

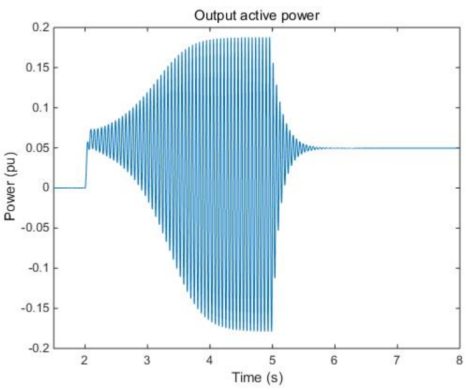
Output active power
Power (pu)
Time (s)

g)

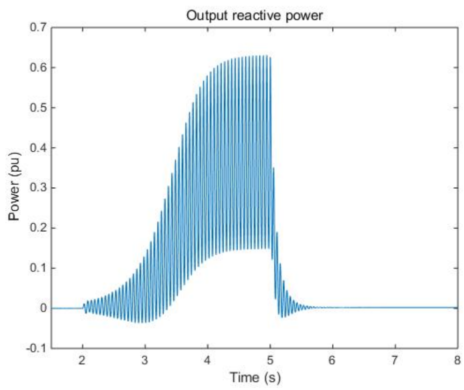
Output reactive power
Power (pu)
Time (s)

h)

Fig. 4.8. Dynamics of the VSC in the time-domain simulation of the case when changing SCR with various line reactance. a) *d*-axis component of current i_{cd}. b) *q*-axis component of current i_{cq}. c) *d*-axis component of reference voltage v_{cdr}. d) *q*-axis component of reference voltage v_{cqr}. e) Phase A current. f) DC voltage v_{dc}. g) Output active power. h) Output reactive power.

Dynamics of the VSC in the time-domain simulation of the case when changing SCR with various line reactance are shown in Fig. 4.8. F_X=1 initially and after the WTG output active power P_{WTG} increases from zero to 10% of $P_{WTG,\ rated}$ at 2 s, the system is unstable between 2s to 5s. Then F_X is decreased from 1 to 0.83 (SCR=1.71) at 5s, the system becomes stable. The simulation results are consistent with previous stability analysis results that verify the correctness of the stability studies.

4.3.3 Effect of VSC output power

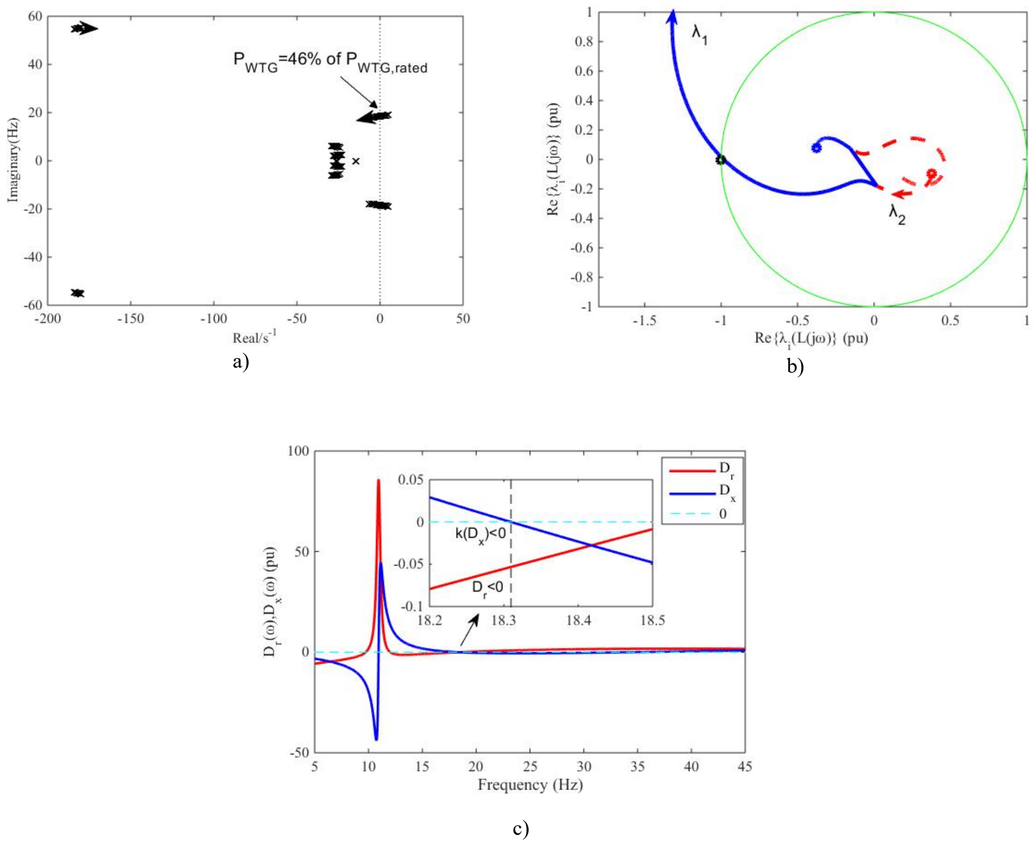

Fig. 4.9. Stability study of the case when with different P_{WTG}. a) Eigenvalue analysis. b) GNC. c) Determinant-impedance criterion.

In Fig. 4.9 a), the output active power of one WTG P_{WTG} is increased from 10% to 70% of $P_{WTG,\ rated}$, the real part of the eigenvalue changes from positive to negative, the stability of the system is increased. The stability region is P_{WTG} >46% of $P_{WTG,\ rated}$ and increased P_{WTG} leads to the decrease of oscillation frequency. Fig. 4.9 b) and Fig. 4.9 c) are the analysis results in GNC and determinant criterion when P_{WTG}=50% of $P_{WTG,\ rated}$. The GNC allows verifying the stable results because the curves of the eigenvalues λ_1 and λ_2 do not encircle the (−1,0) point. And the determinant-impedance criterion predicts the system is stable because, in the neighbourhood of the previous poorly damped poles, the slope of $D_x(\omega_x)$ is negative, $k(D_x) < 0$, and $D_r(\omega_x)$ is negative, $D_r(\omega_x) < 0$, at the zero-crossing frequency of $D_x(\omega_x)$ =19.32 Hz.

Dynamics of the VSC in the time-domain simulation of the case when changing P_{WTG} are shown in Fig. 4.10. The number of connected WTGs is 500, the system is stable between 2-3s after the P_{WTG} =10% of $P_{WTG,\ rated}$ is injected at 2 s. At 3s, the number of connected WTGs is increased from 500 to 600 and then the SSI occurs. When P_{WTG} is increased to 50% of $P_{WTG,\ rated}$ at 5s, the system becomes stable again. The simulation results are consistent with the previous stability study.

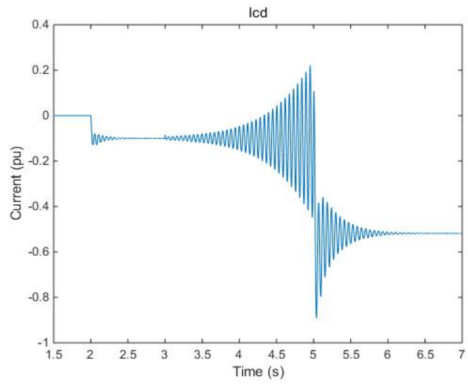
Icd
Current (pu)
Time (s)

a)

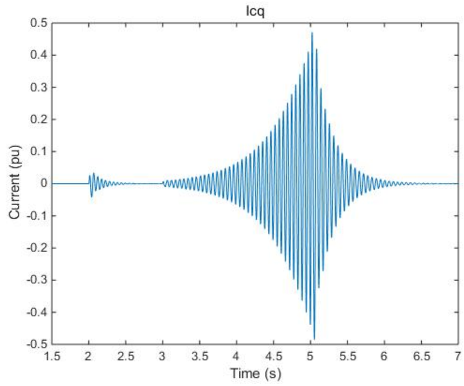
Icq
Current (pu)
Time (s)

b)

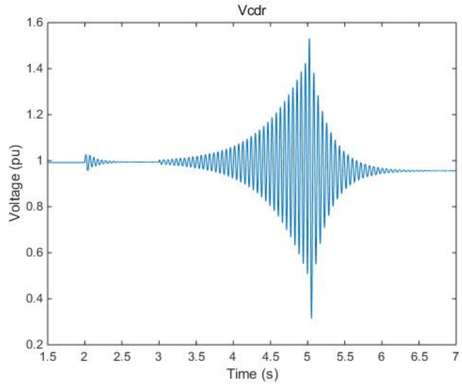
Vcdr
Voltage (pu)
Time (s)

c)

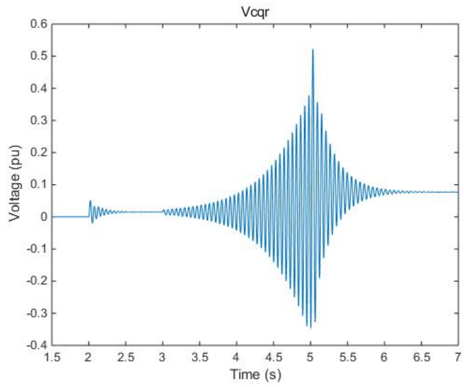
Vcqr
Voltage (pu)
Time (s)

d)

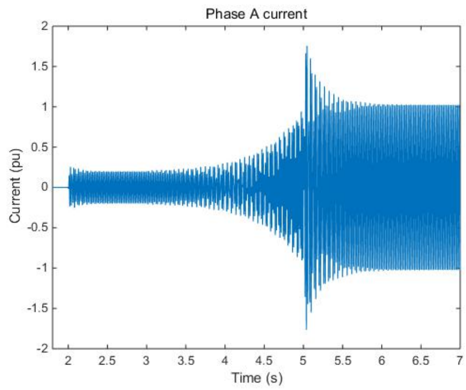
Phase A current
Current (pu)
Time (s)

e)

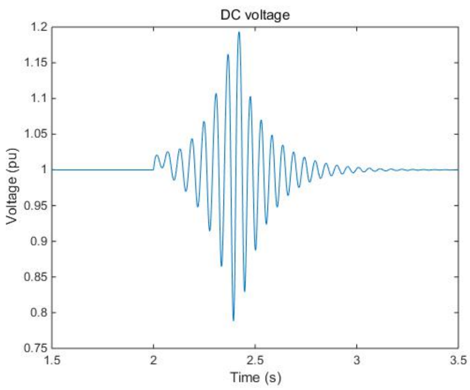
DC voltage
Voltage (pu)
Time (s)

f)

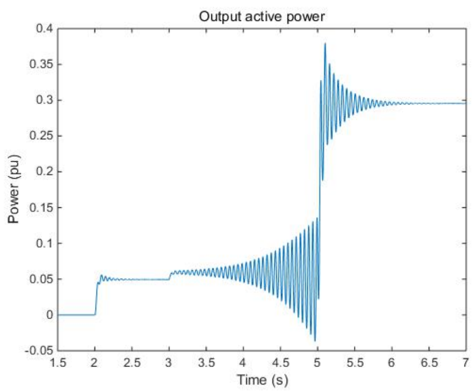
Output active power
Power (pu)
Time (s)

g)

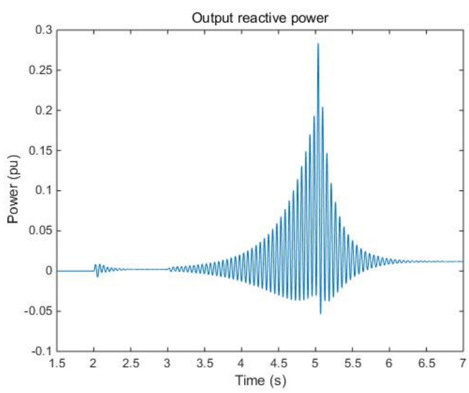
Output reactive power
Power (pu)
Time (s)

h)

Fig. 4.10. Dynamics of the VSC in the time-domain simulation of the case with different P_{WTG}, a) *d*-axis component of current i_{cd}. b) *q*-axis component of current i_{cq}. c) *d*-axis component of reference voltage v_{cdr}. d) *q*-axis component of reference voltage v_{cqr}. e) Phase A current. f) DC voltage v_{dc}. g) Output active power. h) Output reactive power.

4.3.4 Effect of various control system parameters

The parameters of control loops in the VSC will affect the system stability including the bandwidth of feed-forward voltage low-pass filter ω_{Hf}, the bandwidth of current loop ω_{cc}, the bandwidth of outer loop ω_{dc} and bandwidth of PLL ω_{pll}. The deductions of ω_{Hf}, ω_{cc}, ω_{dc} and ω_{pll} are shown in Appendix D. The details of these SSI modes are analysed as follows:

1) Feed-forward voltage low-pass filter

The poles of the equivalent closed-loop system model with various feed-forward voltage low-pass filter bandwidths ω_{Hf} are shown in Fig. 4.11 (eigenvalues only with positive frequencies are shown for a clear illustration). When ω_{Hf} is increased from $0.1\omega_{Hf,\ ref}$ to $5\omega_{Hf,\ ref}$, an unstable eigenvalue moves right firstly when $\omega_{Hf} < 1.2\omega_{Hf,\ ref}$ and then moves left when $\omega_{Hf} > 1.2\omega_{Hf,\ ref}$, the system stability region is $\omega_{Hf} < 1.2\omega_{Hf,\ ref}$ or $\omega_{Hf} > 2.6\omega_{Hf,\ ref}$. Moreover, lower ω_{Hf} will lead to a lower oscillation frequency.

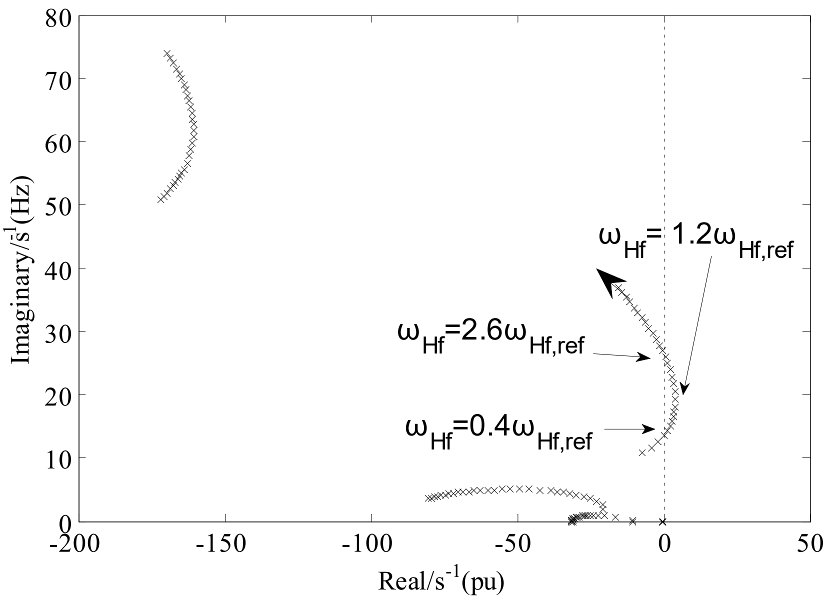

Fig. 4.11. Eigenvalue analysis of the case when with different ω_{Hf}.

Fig. 4.12 a) and b) show the GNC allows verifying the stable results of the system when $\omega_{Hf}=0.1\omega_{Hf,\ ref}$ and $\omega_{Hf}=5\omega_{Hf,\ ref}$ respectively because the curves of the eigenvalues λ_1 and λ_2 do not encircle the $(-1,0)$ point. In Fig. 4.12 c), when $\omega_{Hf}=0.1\omega_{Hf,\ ref}$, the determinant-impedance criterion predicts that the system is stable because, in the neighbourhood of the previous poorly damped poles, the slope of $D_x(\omega_x)$ is negative, $k(D_x) < 0$, and $D_r(\omega_x)$ is negative, $D_r(\omega_x) < 0$, at the zero-crossing frequency of $D_x(\omega_x)$ =11.75 Hz. Similarly in Fig. 4.12 d), when $\omega_{Hf}=5\omega_{Hf,\ ref}$, the determinant-impedance criterion indicates that the system is stable because, in the neighbourhood of the previous poorly damped poles, the slope of $D_x(\omega)$ is negative, $k(D_x) < 0$, and $Dr(\omega)$ is negative, $Dr(\omega) < 0$, at the zero-crossing frequency of $Dx(\omega)$=34.1 Hz. From the above stability analysis results, it can be concluded that when ω_{Hf} is increased, system stability is decreased firstly and then increased.

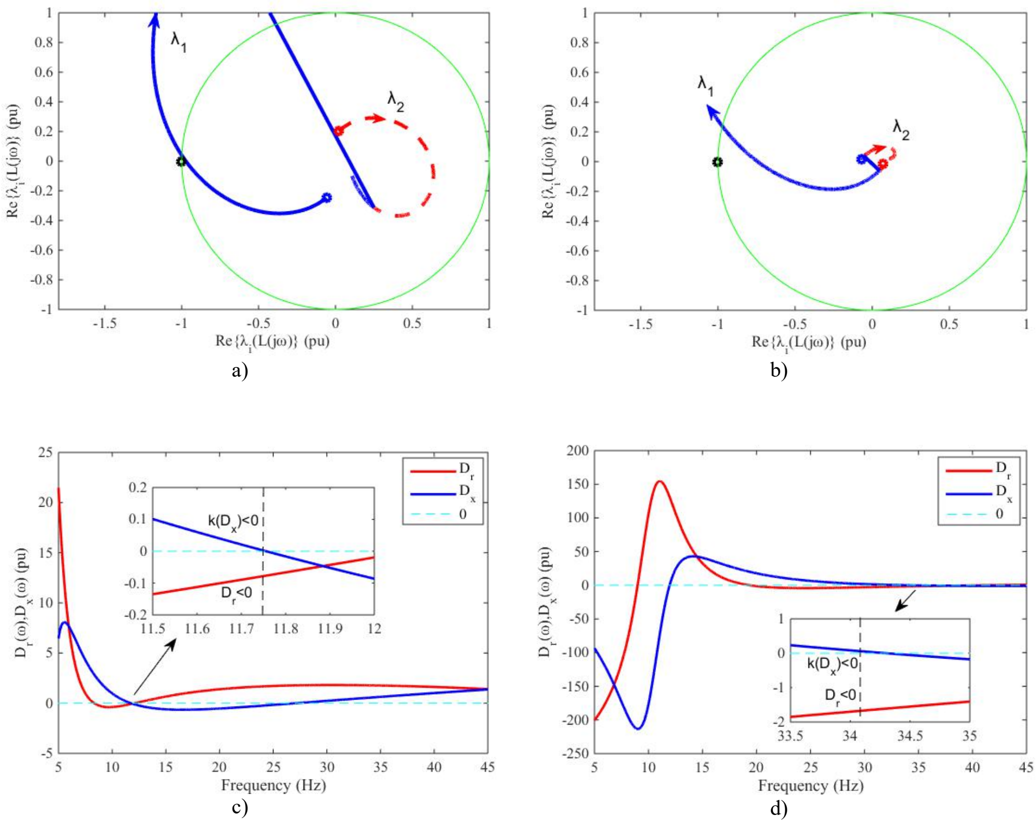

Fig. 4.12. Stability study of the case when changing bandwidth of feed-forward voltage low-pass filter. a) $\omega_{Hf}=0.1\omega_{Hf,\ ref}$ in GNC. b) $\omega_{Hf}=5\omega_{Hf,\ ref}$ in GNC. c) $\omega_{Hf}=0.1\omega_{Hf,\ ref}$ in determinant-impedance criterion. d) $\omega_{Hf}=5\omega_{Hf,\ ref}$ in determinant-impedance criterion.

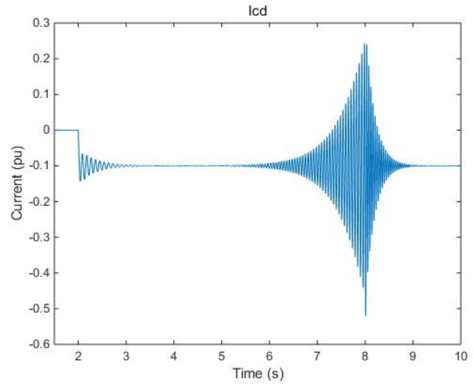
Icd
Current (pu)
Time (s)

a)

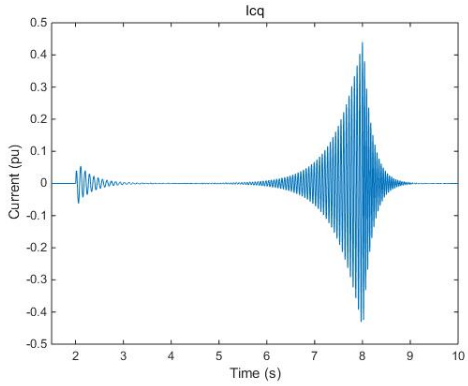
Icq
Current (pu)
Time (s)

b)

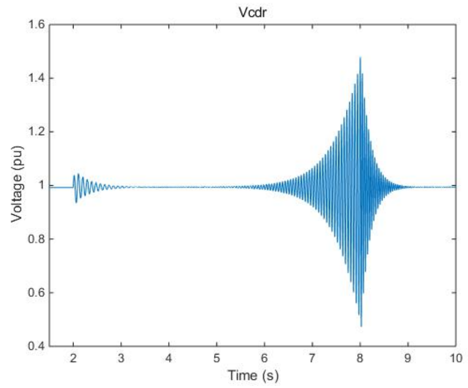
Vcdr
Voltage (pu)
Time (s)

c)

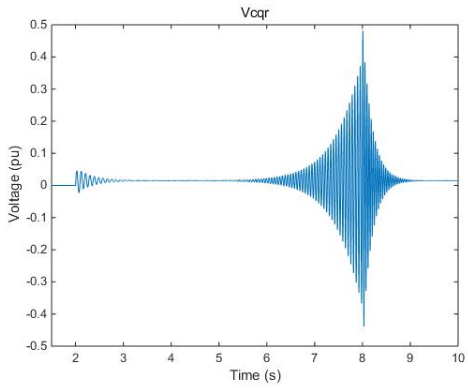
Vcqr
Voltage (pu)
Time (s)

d)

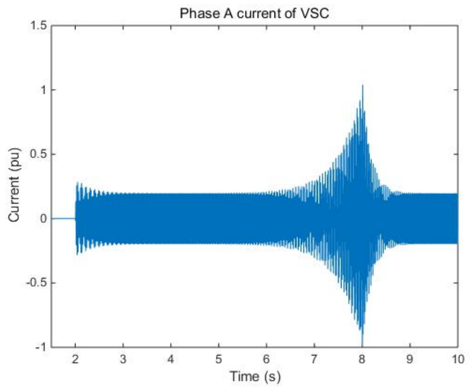
Phase A current of VSC
Current (pu)
Time (s)

e)

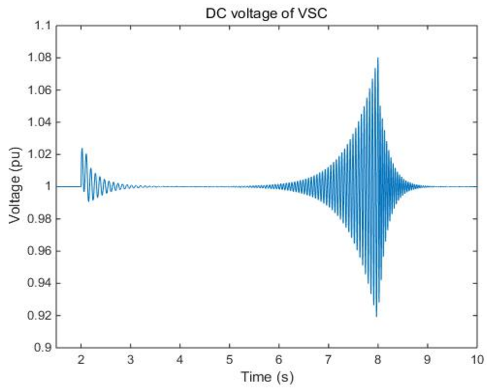
DC voltage of VSC
Voltage (pu)
Time (s)

f)

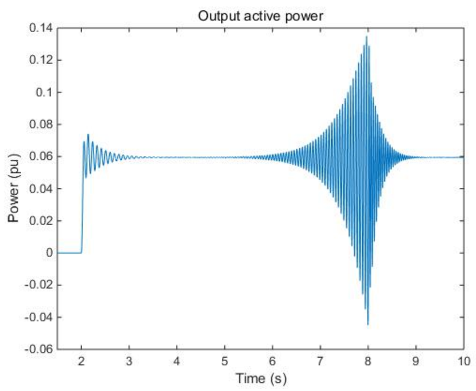
Output active power
Power (pu)
Time (s)

g)

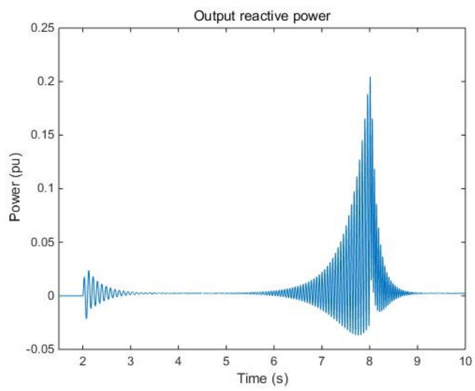
Output reactive power
Power (pu)
Time (s)

h)

Fig. 4.13. Dynamics of the VSC in the time-domain simulation of the case when changing bandwidth of feed-forward voltage low-pass filter. a) d-axis component of current i_{cd}. b) q-axis component of current i_{cq}. c) d-axis component of reference voltage v_{cdr}. d) q-axis component of reference voltage v_{cqr}. e) Phase A current. f) DC voltage v_{dc}. g) Output active power. h) Output reactive power.

Dynamics of the VSC in the time-domain simulation of the case when changing ω_{Hf} are shown in Fig. 4.13. The P_{WTG} is raised from zero to 10% of $P_{WTG, rated}$ with 600 WTGs connected at 2s and ω_{Hf}=0.1$\omega_{Hf, ref}$ at first. The system is stable initially and becomes unstable after the increment of ω_{Hf} from 0.1$\omega_{Hf, ref}$ to $\omega_{Hf, ref}$ at 5s. Then after ω_{Hf} is increased to 5$\omega_{Hf, ref}$ at 8s, SSI is suppressed, and the system becomes stable again. The simulation results verify the accuracy of the stability studies.

2) Inner current control loop

System poles are shown in Fig. 4.14 when inner current control loop bandwidth ω_{cc} increases from 0.1$\omega_{cc, ref}$ to 2$\omega_{cc, ref}$ (eigenvalues only with positive frequencies are shown for a clear illustration). An unstable eigenvalue moves left with the increment of ω_{cc}. The system stability region is ω_{cc} >1.1$\omega_{cc, ref}$. Moreover, lower ω_{cc} leads to lower oscillation frequency.

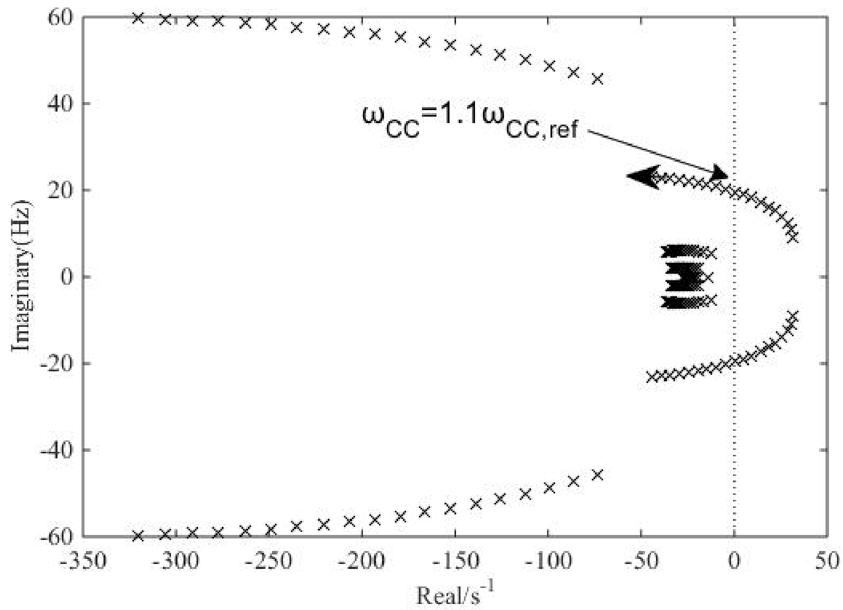

Fig. 4.14. Eigenvalue analysis of the case when with different ω_{cc}.

Fig. 4.15 a) shows the stability analysis by using GNC when ω_{cc}=1.05$\omega_{cc, ref}$. It indicates the unstable results because the curves of the eigenvalue λ_1 encircle the (−1,0) point in a clockwise direction. In Fig. 4.15 b), GNC allows verifying the stable results when ω_{cc}=1.15$\omega_{cc,\ ref}$ because the curves of the eigenvalues λ_1 and λ_2 do not encircle the (−1,0) point. In Fig. 4.15 c), the determinant-impedance criterion indicates that the system is unstable when ω_{cc}=1.05$\omega_{cc,\ ref}$ because, in the neighbourhood of the previous poorly damped poles, the slope of $D_x(\omega_x)$ is negative, $k(D_x) < 0$, but $D_r(\omega_x)$ is positive, $D_r(\omega_x) >0$, at the zero-crossing frequency of $D_x(\omega_x)$ =19.56 Hz. While the determinant-impedance criterion shows that the system is stable when ω_{cc}=1.15$\omega_{cc,\ ref}$ in Fig. 4.15 d) because the slope of $D_x(\omega_x)$ is negative, $k(D_x) < 0$, and $D_r(\omega_x)$ is negative, $D_r(\omega_x) >0$, at the zero-crossing frequency of $D_x(\omega_x)$ =19.7 Hz. From the above stability analysis results, it can be concluded that system stability will be increased with a larger ω_{cc}.

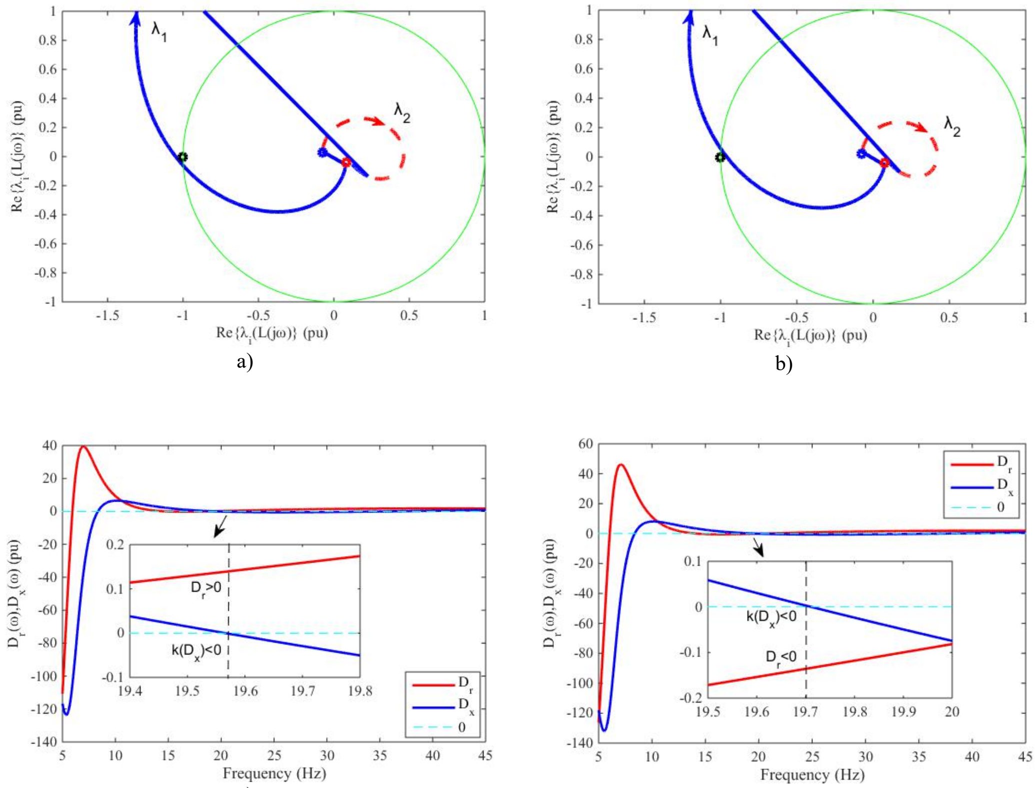

Fig. 4.15. Stability study of the case when changing the bandwidth of inner current control loop. a) ωcc=1.05ωcc, ref in GNC. b) ωcc=1.15ωcc, ref in GNC. c) ωcc=1.05ωcc, ref in determinant-impedance criterion. d) ωcc=1.15ωcc, ref in determinant-impedance criterion.

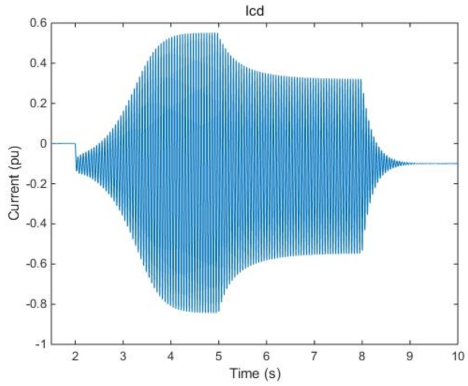
Icd
Current (pu)
Time (s)

a)

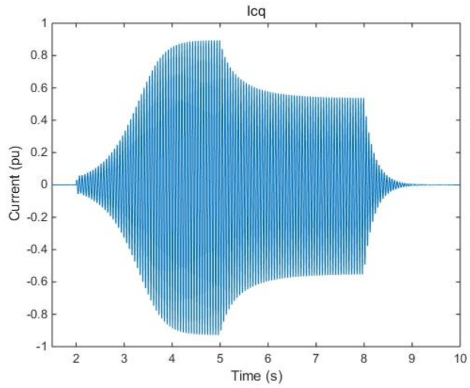
Icq
Current (pu)
Time (s)

b)

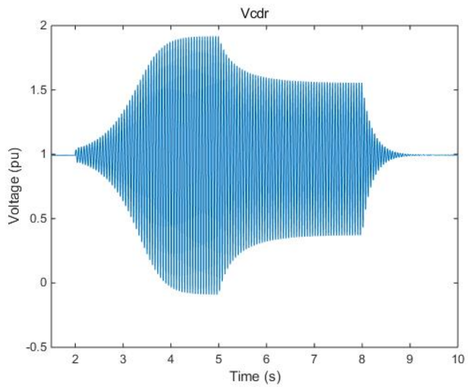
Vcdr
Voltage (pu)
Time (s)

c)

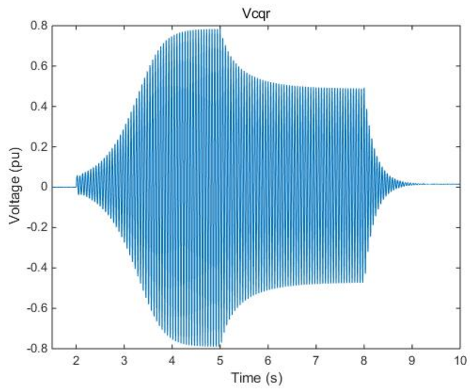
Vcqr
Voltage (pu)
Time (s)

d)

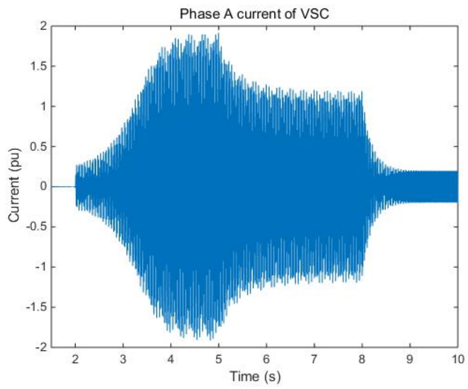
Phase A current of VSC
Current (pu)
Time (s)

e)

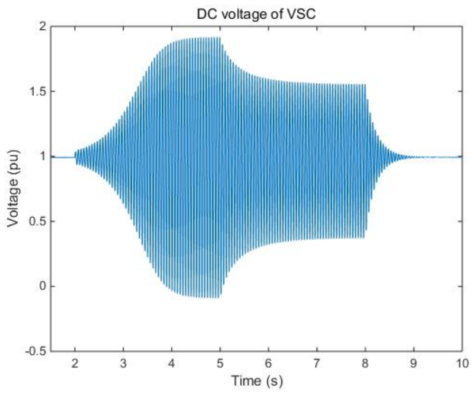
DC voltage of VSC
Voltage (pu)
Time (s)

f)

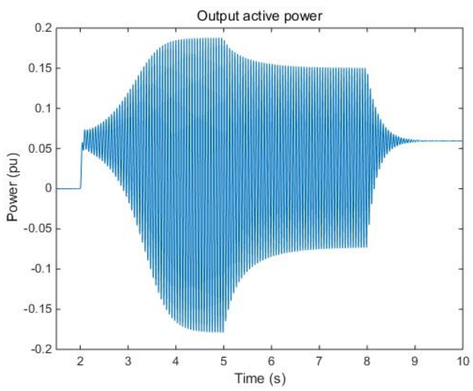
Output active power
Power (pu)
Time (s)

g)

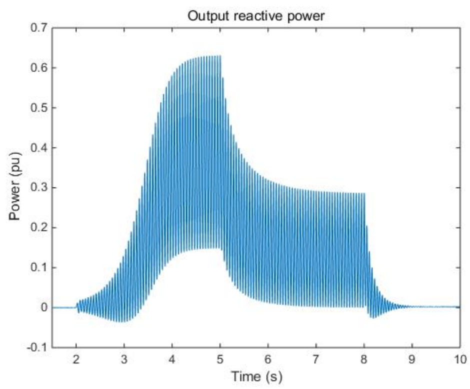
Output reactive power
Power (pu)
Time (s)

h)

Fig. 4.16. Dynamics of the VSC in the time-domain simulation of the case when changing the bandwidth of inner current control loop. a) *d*-axis component of current i_{cd}. b) *q*-axis component of current i_{cq}. c) *d*-axis component of reference voltage v_{cdr}. d) *q*-axis component of reference voltage v_{cqr}. e) Phase A current. f) DC voltage v_{dc}. g) Output active power. h) Output reactive power.

The correctness of the stability study is validated in time-domain simulation as shown in Fig. 4.16. P_{WTG} is raised from zero to 10% of $P_{WTG, rated}$ with 600 WTGs connected at 2s and $\omega_{cc} = \omega_{cc, ref}$ at first. The system is unstable initially and after ω_{cc} is increased to $1.05\omega_{cc, ref}$ at 5s, the amplitude of the oscillation is decreased but the SSI is not eliminated yet. When ω_{cc} is increased from $1.05\omega_{cc, ref}$ to $1.15\omega_{cc, ref}$ at 8s, the SSI is suppressed, and the system becomes stable.

3) Outer control loop

The poles of the equivalent closed-loop system model with various outer control bandwidths ω_{dc} are shown in Fig. 4.17 (eigenvalues only with positive frequencies are shown for a clear illustration). When ω_{dc} is increased from $0.1\omega_{dc, ref}$ to $3\omega_{dc, ref}$, an unstable eigenvalue moves right firstly when $\omega_{dc} < 0.8\omega_{dc, ref}$ and then moves left when $\omega_{dc} > 0.8\omega_{dc, ref}$, the system stability region is $\omega_{dc} < 0.2\omega_{dc, ref}$ or $\omega_{dc} > 1.7\omega_{dc, ref}$. Moreover, lower ω_{dc} will lead to a lower oscillation frequency.

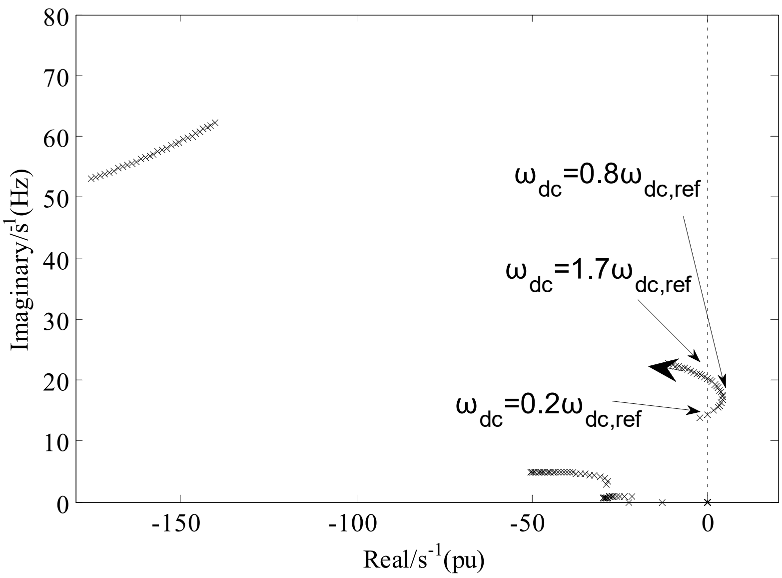

Fig. 4.17 Eigenvalue analysis of the case when with different ω_{dc}.

Fig. 4.18 a) and b) show the GNC allows verifying the stable results of the system when $\omega_{dc} = 0.1\omega_{dc, ref}$ and $\omega_{dc} = 3\omega_{dc, ref}$ respectively because the curves of the eigenvalues λ_1 and λ_2 do not encircle the $(-1,0)$ point. In Fig. 4.18 c), when $\omega_{dc} = 0.1\omega_{dc, ref}$, the determinant-impedance criterion predicts that the system is stable because, in the neighbourhood of the previous poorly damped poles, the slope of $D_x(\omega_x)$ is negative, $k(D_x) < 0$, and $D_r(\omega_x)$ is negative, $D_r(\omega_x) < 0$, at the zero-crossing frequency of $D_x(\omega_x)$ =14.62 Hz. Similarly in Fig. 4.18 d), when ω_{dc}=3$\omega_{dc,\ ref}$, the determinant-impedance criterion indicates that the system is stable because, in the neighbourhood of the previous poorly damped poles, the slope of $D_x(\omega_x)$ is negative, $k(D_x) < 0$, and $D_r(\omega_x)$ is negative, $D_r(\omega_x) < 0$, at the zero-crossing frequency of $D_x(\omega_x)$ =22.4 Hz. From the above stability analysis results, it can be concluded that when ω_{dc} is increased, system stability is decreased firstly and then increased.

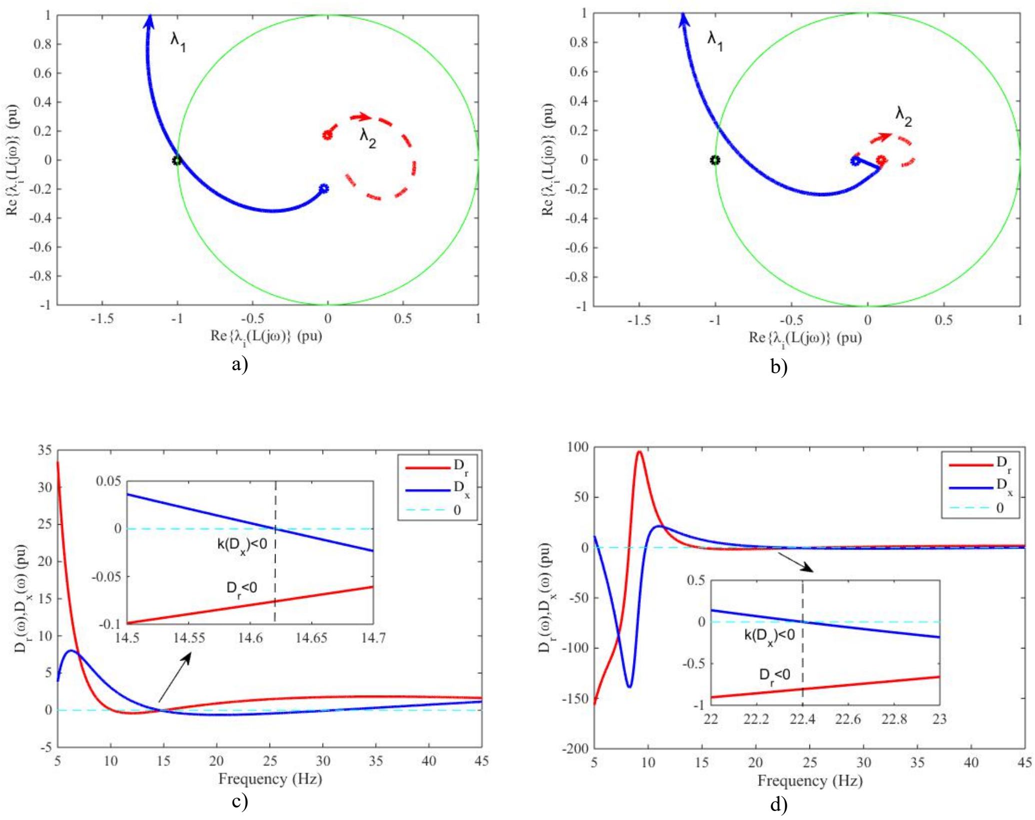

Fig. 4.18. Stability study of the case when changing the bandwidth of outer control loop. a) ω_{dc}=0.1$\omega_{dc,\ ref}$ in GNC. b) ω_{dc}=3$\omega_{dc,\ ref}$ in GNC. c) ω_{dc}=0.1$\omega_{dc,\ ref}$ in determinant-impedance criterion. d) ω_{dc}=3$\omega_{dc,\ ref}$ in determinant-impedance criterion.

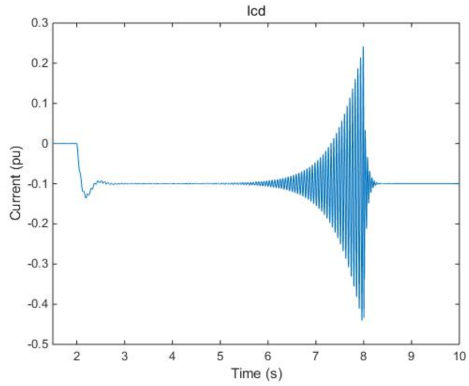
Icd
Current (pu)
Time (s)
a)

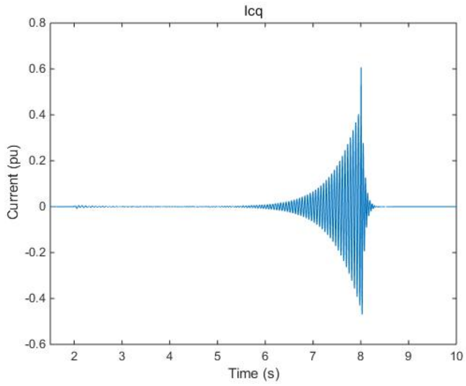
Icq
Current (pu)
Time (s)
b)

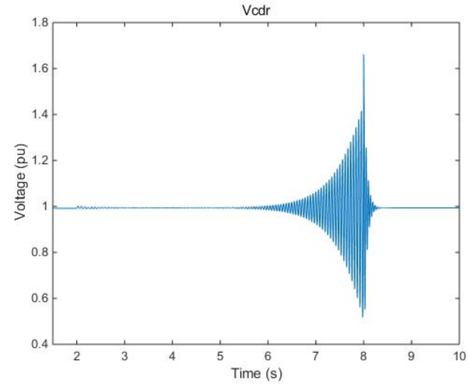
Vcdr
Voltage (pu)
Time (s)
c)

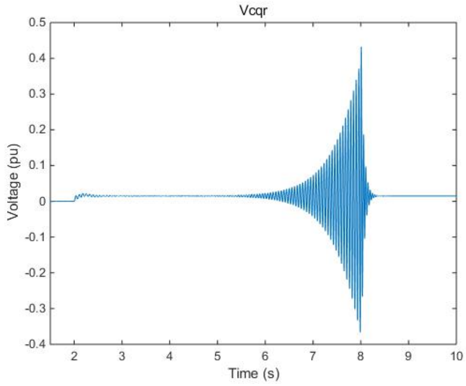
Vcqr
Voltage (pu)
Time (s)
d)

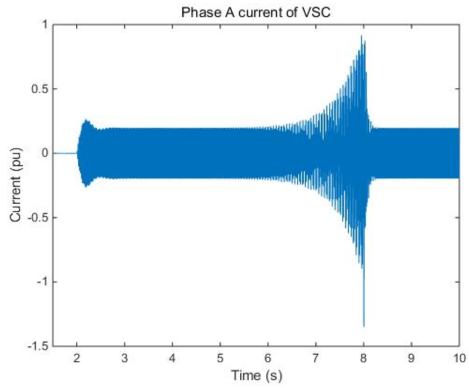
Phase A current of VSC
Current (pu)
Time (s)
e)

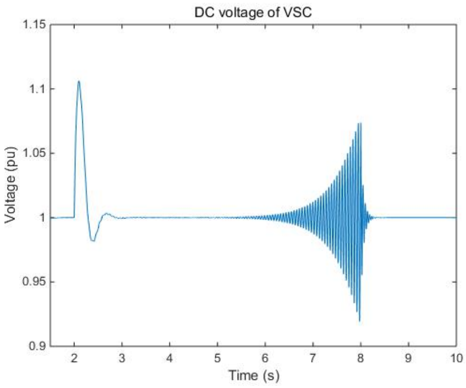
DC voltage of VSC
Voltage (pu)
Time (s)
f)

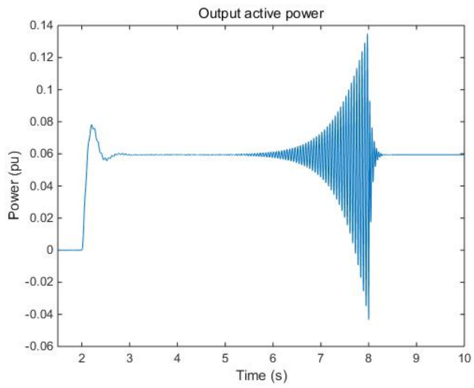
Output active power
Power (pu)
Time (s)
g)

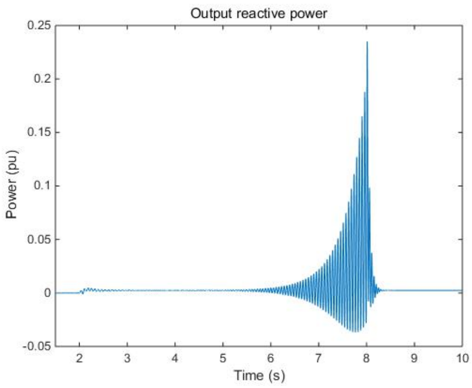
Output reactive power
Power (pu)
Time (s)
h)

Fig. 4.19. Dynamics of the VSC in the time-domain simulation of the case when changing the bandwidth of outer control loop. a) d-axis component of current i_{cd}. b) q-axis component of current i_{cq}. c) d-axis component of reference voltage v_{cdr}. d) q-axis component of reference voltage v_{cqr}. e) Phase A current. f) DC voltage v_{dc}. g) Output active power. h) Output reactive power.

The correctness of the stability study is validated in time-domain simulation as shown in Fig. 4.19. P_{WTG} is raised from zero to 10% of $P_{WTG, rated}$ with 600 WTGs connected at 2s and ω_{dc} =0.1$\omega_{dc, ref}$ at first. The system is stable initially and becomes unstable after the increment of ω_{dc} from 0.1$\omega_{dc, ref}$ to $\omega_{dc, ref}$ at 5s. Then after ω_{dc} is increased to 3$\omega_{dc, ref}$ at 8s, SSI is suppressed, and the system becomes stable again.

4) PLL

System poles are shown in Fig. 4.20 when PLL bandwidth ω_{pll} increases from 0.1$\omega_{pll, ref}$ to 10$\omega_{pll, ref}$ (eigenvalues only with positive frequencies are shown for a clear illustration). The unstable eigenvalue moves right firstly when ω_{pll} < 2$\omega_{pll, ref}$ and then moves left when ω_{pll} > 2$\omega_{pll, ref}$ the stability region is ω_{pll} < 0.5$\omega_{pll, ref}$ or ω_{pll} >4.9$\omega_{pll, ref}$. Moreover, decreased ω_{pll} will lead to a lower oscillation frequency.

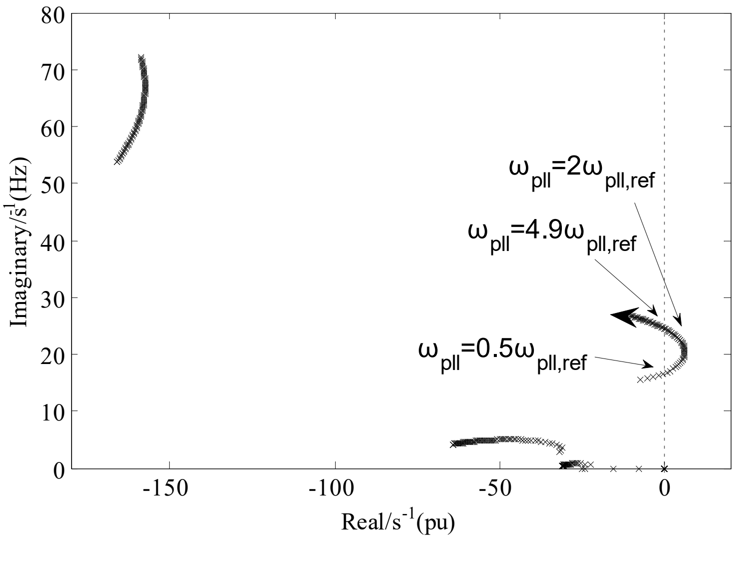

Fig. 4.20. Eigenvalue analysis. of the case when with different ω_{pll}.

Fig. 4.21 a) and b) show the GNC allows verifying the stable results of the system when ω_{pll}=0.1$\omega_{pll, ref}$ and ω_{pll}=3$\omega_{pll, ref}$ respectively because the curves of the eigenvalues λ_1 and λ_2 do not encircle the (−1,0) point. In Fig. 4.21 c), when ω_{pll}=0.1$\omega_{pll, ref}$, the determinant-impedance criterion predicts that the system is stable because, in the neighbourhood of the previous poorly damped poles, the slope of $D_x(\omega_x)$ is negative,

$k(D_x) < 0$, and $D_r(\omega_x)$ is negative, $D_r(\omega_x) < 0$, at the zero-crossing frequency of $D_x(\omega_x)$ =15.1 Hz. Similarly in Fig. 4.21 d), when ω_{pll}=5$\omega_{pll,\ ref}$, the determinant-impedance criterion indicates that the system is stable because, in the neighbourhood of the previous poorly damped poles, the slope of $D_x(\omega_x)$ is negative, $k(D_x) < 0$, and $D_r(\omega_x)$ is negative, $D_r(\omega_x) < 0$, at the zero-crossing frequency of $D_x(\omega_x)$ =26.25 Hz. From the above stability analysis results, it can be concluded that when ω_{pll} is increased, system stability is decreased firstly and then increased.

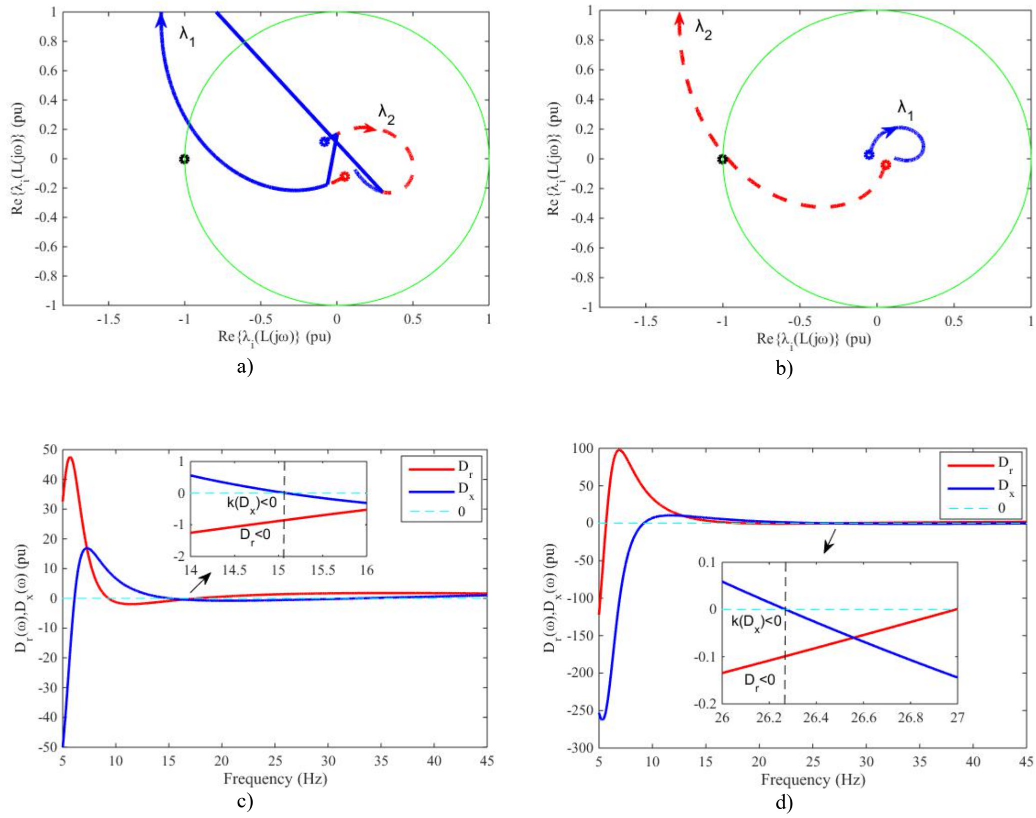

Fig. 4.21. Stability study of the case when changing the bandwidth of PLL. a) ω_{pll}=0.1$\omega_{pll,\ ref}$ in GNC. b) ω_{pll}=5$\omega_{pll,\ ref}$ in GNC. c) ω_{pll}=0.1$\omega_{pll,\ ref}$ in determinant-impedance criterion. d) ω_{pll}=5$\omega_{pll,\ ref}$ in determinant-impedance criterion.

Dynamics of the VSC in the time-domain simulation of the case when changing ω_{pll} are shown in Fig. 4.22. The P_{WTG} is raised from zero to 10% of $P_{WTG,\ rated}$ with 600 WTGs connected at 2s and ω_{pll}=0.1$\omega_{pll,\ ref}$ at first. The system is stable initially and becomes unstable after the increment of ω_{pll} from 0.1$\omega_{pll,\ ref}$ to $\omega_{pll,\ ref}$ at 5s. Then after ω_{pll} is increased to 5$\omega_{pll,\ ref}$ at 8s, SSI is suppressed, and the system becomes stable again. The simulation results verify the accuracy of the stability studies.

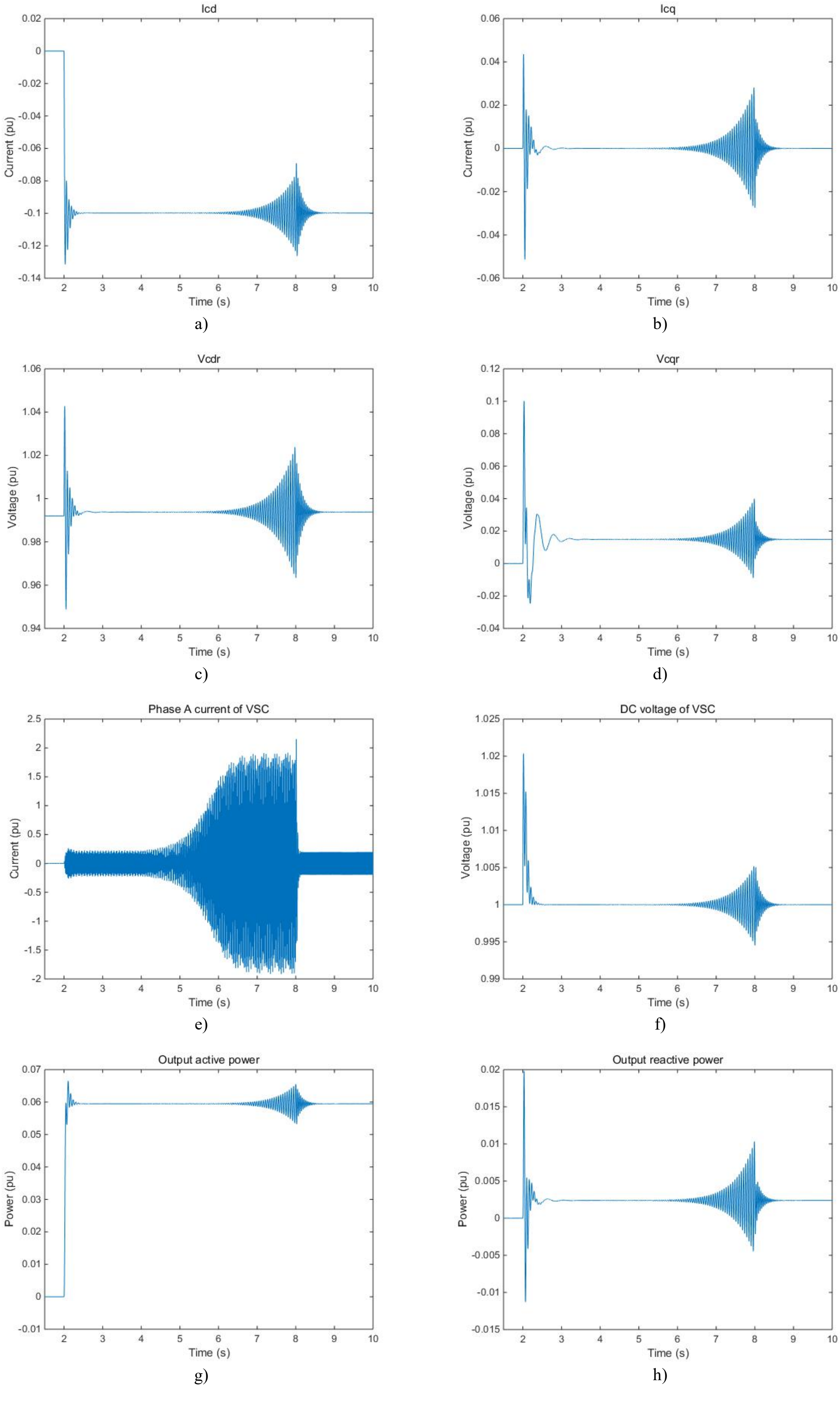
Icd
Current (pu)
Time (s)
Icq
Current (pu)
Time (s)
Vcdr
Voltage (pu)
Time (s)
Vcqr
Voltage (pu)
Time (s)
Phase A current of VSC
Current (pu)
Time (s)
DC voltage of VSC
Voltage (pu)
Time (s)
Output active power
Power (pu)
Time (s)
Output reactive power
Power (pu)
Time (s)

a) b)

c) d)

e) f)

g) h)

Fig. 4.22. Dynamics of the VSC in the time-domain simulation of the case when changing the bandwidth of PLL. a) d-axis component of current i_{cd}. b) q-axis component of current i_{cq}. c) d-axis component of reference voltage v_{cdr}. d) q-axis component of reference voltage v_{cqr}. e) Phase A current. f) DC voltage v_{dc}. g) Output active power. h) Output reactive power.

4.3.5 Mechanism analysis of the newly found SSI

The mechanism of SSI plays an important role in the study of SSI. Based on the impedance model, the mechanism of SSI is analysed in [31]. The conclusion shows that the weak damping SSI mode will appear when the strength of the AC grid is weak. WTG in the subsynchronous frequency band, is shown as a capacitive impedance with a small negative resistance, which forms a resonant circuit with the power grid, but there is no sufficient explanation for the reason.

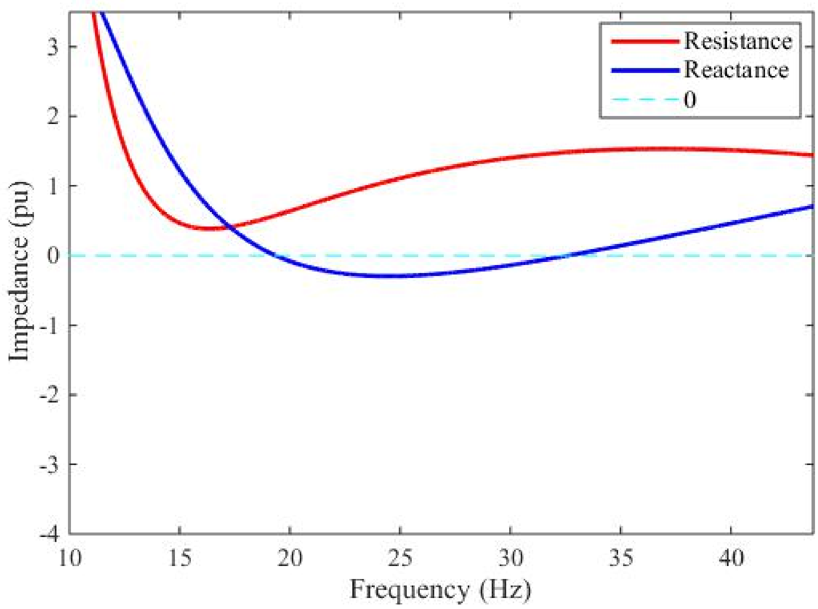

Fig. 4.23. Impedance-versus-frequency curves of the determinant D(s).

The impedance-frequency curves of the determinant D(s) when the typical scenario in Fig. 3.8 is used (an unstable case when SCR=1.34) as shown in Fig. 4.23. In the frequency range of 19 ~ 33Hz, the reactance is negative which will lead the system to form an R-L-C circuit that causes the risk of electrical resonance. However, the resistance of the equivalent R-L-C circuit is always positive in the whole subsynchronous range as shown in the figure. This result presents a different conclusion with paper [31] which indicates negative resistance effect is not the basic reason for the occurrence of SSI. SSI may occur even the equivalent resistance is positive. To investigate the physical mechanism of SSI, the equivalent impedance model of the studied system in Fig 3.1 is presented in Fig 4.24.

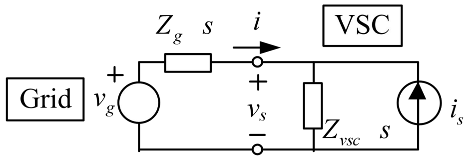

Fig. 4.24. Equivalent impedance model of the studied system.

The relationship between voltage v_s and current i can be described as

$$\Delta \boldsymbol{i} = \underbrace{\frac{\boldsymbol{Y_{vsc}(s)}}{\boldsymbol{I}+\boldsymbol{Y_{vsc}(s)Z_g(s)}}}_{\boldsymbol{G_O(s)}} = \frac{\boldsymbol{I}}{\boldsymbol{Z_{vsc}(s)}+\boldsymbol{Z_g(s)}}\Delta \boldsymbol{v_s} \tag{4-3-2}$$

where

$$\begin{aligned}
\boldsymbol{Y_{vsc}(s)} &= \begin{bmatrix} Y_{v,dd}(s) & 0 \\ 0 & Y_{v,qq}(s) \end{bmatrix} \\
Y_{v,dd}(s) &= G_f(s) - G_{cc}(s)G_{dc}(s) \\
Y_{v,qq}(s) &= G_f(s)(1 - v_{sd0}G_{pll}(s)) - \left\{\frac{P_{s0}}{v_{sd0}}\right\} G_{pll}(s) \\
\boldsymbol{Z_g(s)} &= \begin{bmatrix} R_g + L_g s & -L_g\omega_b \\ L_g\omega_b & R_g + L_g s \end{bmatrix},
\end{aligned} \tag{4-4-3}$$

The details of the system block diagram are shown in Fig 4.25 including the current control loop (CC), direct voltage control loop (DVC), PLL and AC grid. The relationship between grid voltage v_g and current i is derived and it can be found the dq components of them are coupled.

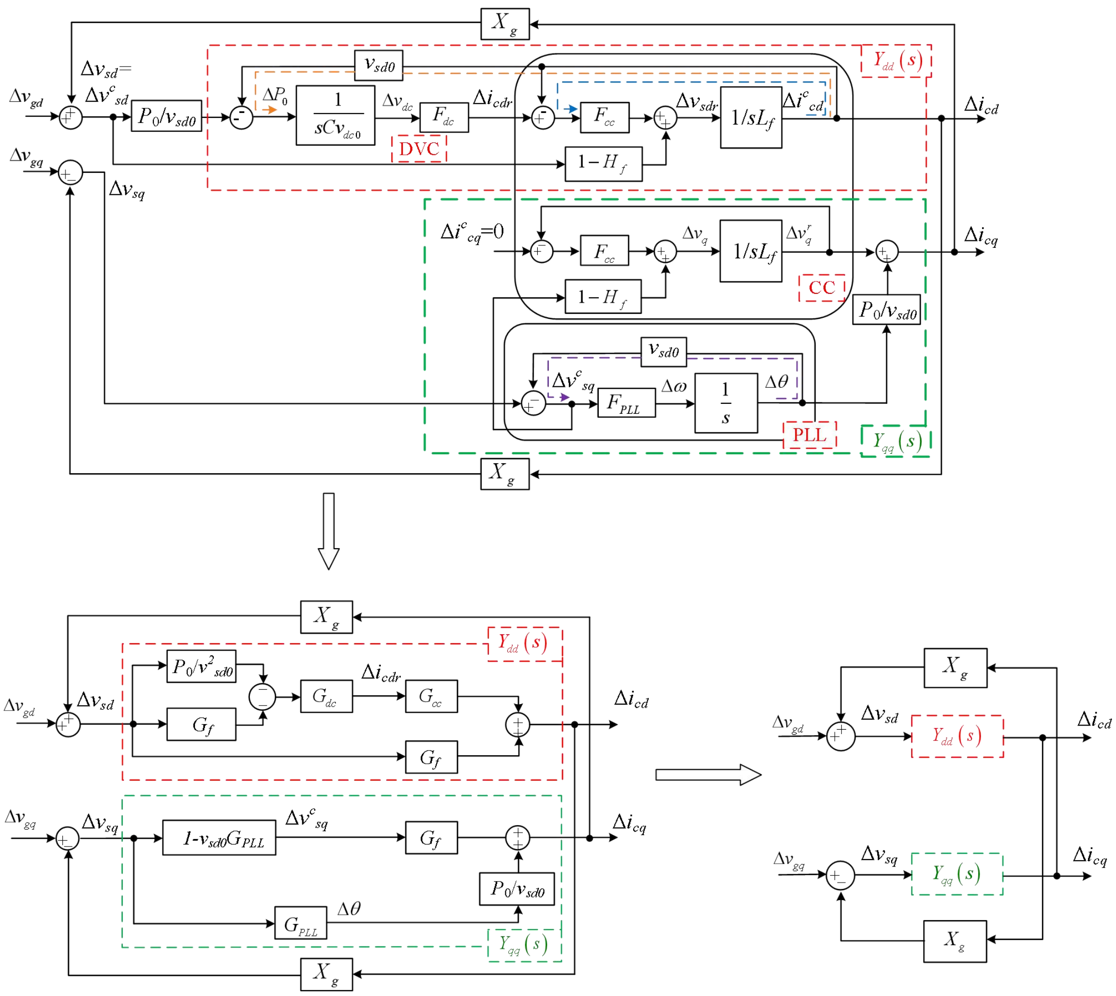

Fig. 4.25. Impedance model block diagram of VSCs connected to an AC grid (i_{cq} = 0).

For a clear explanation, the system model in Fig. 4.25 can be simplified as the model shown in Fig 4.26.

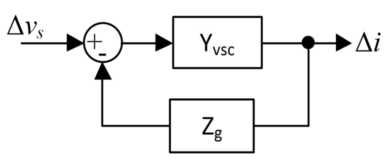

Fig. 4.26 Block diagram of the system.

Where **$G_o(s)$= $Z_g(s)Y_{vsc}(s)$** is the open-loop transfer function of the equivalent closed-loop system. And **$G_o(s)$** can be expressed as

$$\mathbf{G_o}(s) = \begin{bmatrix} \underbrace{(R_g + L_g s)Y_{v,dd}(s)}_{G_{o1}(s)} & \underbrace{-\omega_b L_g Y_{v,dd}(s)}_{G_{o2}(s)} \\ \underbrace{\omega_b L_g \quad {}_{v,qq}(s)}_{G_{o3}(s)} & \underbrace{(R_g + L_g s)Y_{v,qq}(s)}_{G_{o4}(s)} \end{bmatrix} \tag{4-3-4}$$

Then $\mathbf{G_o(s)}$ can be used to assess system stability in the Bode criterion. Fig. 4.27 shows the eigenvalue analysis results that when SCR is increased, system stability is decreased, and the critical stable point is SCR=1.71.

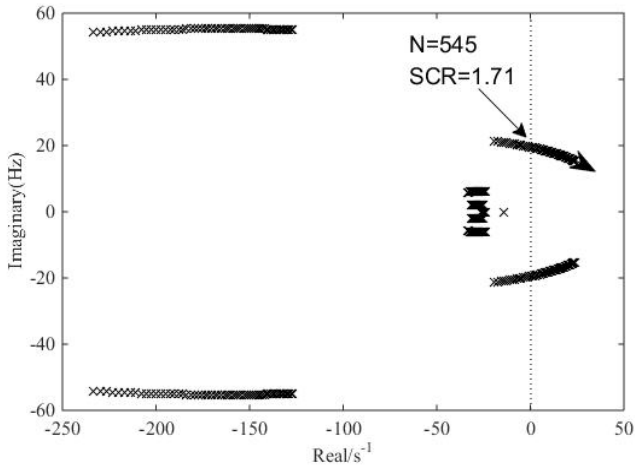

Fig. 4.27. Eigenvalue analysis with different SCR.

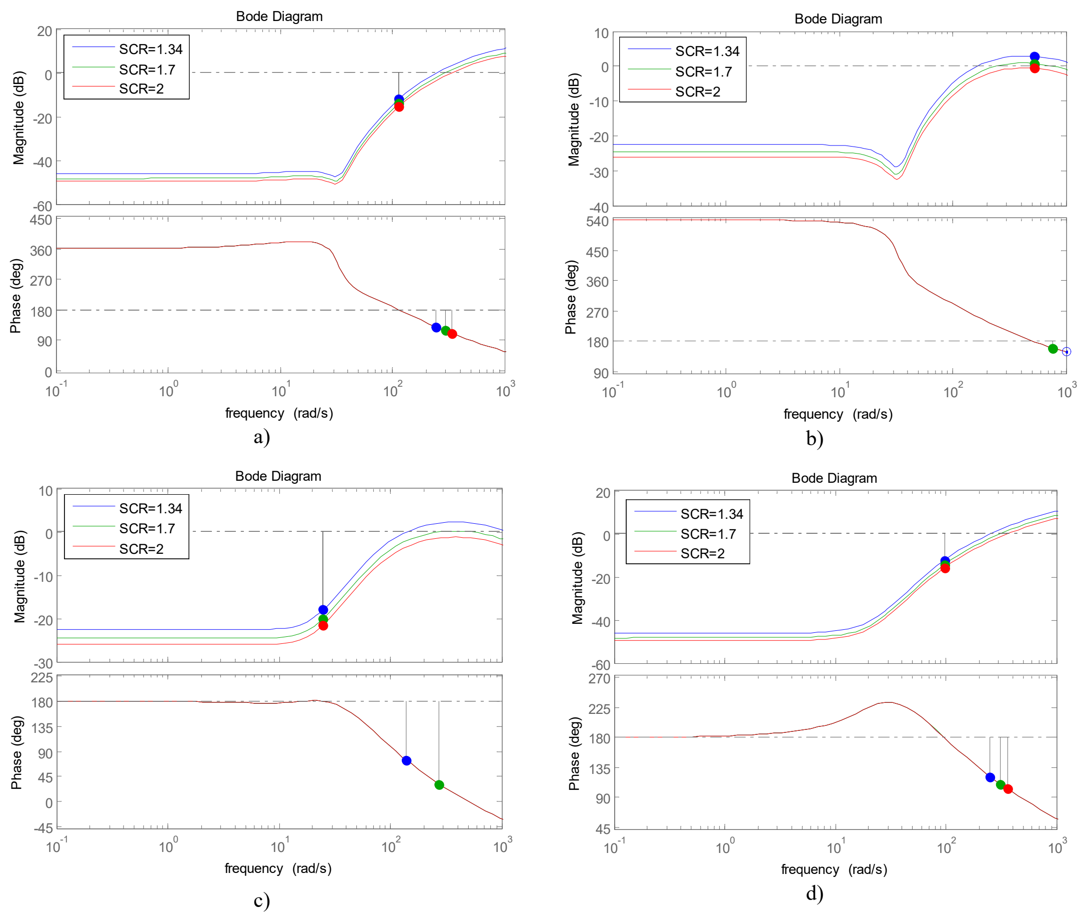

Fig. 4.28. Bode plots of the open-loop transfer function. a) Go1(s), b) Go2(s), c) Go3(s), d) Go4(s).

Then bode plots of $G_{o1}(s)$, $G_{o2}(s)$, $G_{o3}(s)$, $G_{o4}(s)$ in cases when SCR=1.34, SCR=1.7 and SCR=2 are presented respectively. From Fig. 4.28 a), c), d), it can be seen that the magnitude margins are all positive and become larger when SCR is increased, which means system stability is increased. While in Fig. 4.28 b), the magnitude margin of $\mathbf{G_{o2}(s)}$ is negative when SCR=1.34 and SCR=1.7 which are unstable cases. It means that a disturbance signal will be amplified through this closed-loop link which indicates the physical mechanism of the SSI. When SCR is decreased, disturbance of *q*-axis voltage Δv_{sq} caused by current disturbance Δi_d is larger.

4.3.6 Summary

In this chapter, the widely used stability criteria assessing system stability based on the impedance model have been reviewed. Three criteria including GNC, eigenvalue analysis and determinant-impedance criterion are used to assess the system stability and the results are verified by time-domain simulations. Following results of the effects of different factors on system stability are concluded:

1) Low SCR due to the increment of transmission line reactance or the number of online WTGs may lead to system instability. However, if line reactance or the number of online WTGs change together, the status and modes of system stability are approximately the same as long as the SCR of the systems.

2) When the bandwidth of feed-forward voltage low-pass filter ω_f, outer loop control ω_{dc} or PLL ω_{pll} is increased, system stability performance will decrease firstly and then increase.

3) Faster VSC inner current control loop will improve the system stability performance in the test system. Finally, the mechanism of analysis of the newly found SSI is investigated. The mathematical mechanism is analysed. The oscillation mechanism is generally considered to be due to the negative resistance effect in most research. However, from the impedance-frequency curves of the determinant D(s) of the proposed system impedance model, it can be seen that the components of the unstable system in impedance model consists of a capacitive impedance component with a small positive resistance component and then forms a R-L-C resonant circuit with the power grid that leads to the risk of electrical resonance, which against the opinion that SSI is caused of negative resistance effect. And the physical mechanism is presented from the bode plots

results of the opened-loop transfer function of the system. It shows that a disturbance signal will be amplified through the closed-loop from *q*-axis voltage Δv_{sq} to *d*-axis Δi_{d} and increase the potential risk of SSI.

Chapter 5
SSI in multiple VSCs connected to an AC grid

5.1 Introduction

Multiple VSCs connected to an AC grid are AC transmission networks with different components connected at the grid buses such as several main AC grids and VSC-based applications. High voltage direct current (HVDC) systems, as one of the most widely used applications, have emerged as a promising power transmission technology because of their ability to increase power transfer capability and improve power system operation flexibility and energy source interconnection. VSC is one of the core elements of HVDC systems, playing a key role in power conversion between ac and dc systems. However, due to dynamic interactions among the VSCs and the AC grid, oscillatory instabilities will appear and have caused great concern.

Such instabilities are investigated in frequency-domain by using the *dq*-frame impedance-based representation of the multiple VSCs connected to an AC grid in this chapter. An equivalent multiple VSCs connected to an AC grid model is presented. Generalised Nyquist Criterion (GNC) and determinant impedance-based stability criterion to assess the studied system are introduced. A new approach that simplifying the calculation process of the studied system compared with traditional GNC is proposed. The comparisons of the new approach with the traditional criterion are presented. Then the correctness of the analysis is validated through time-domain simulations.

5.2 System modelling

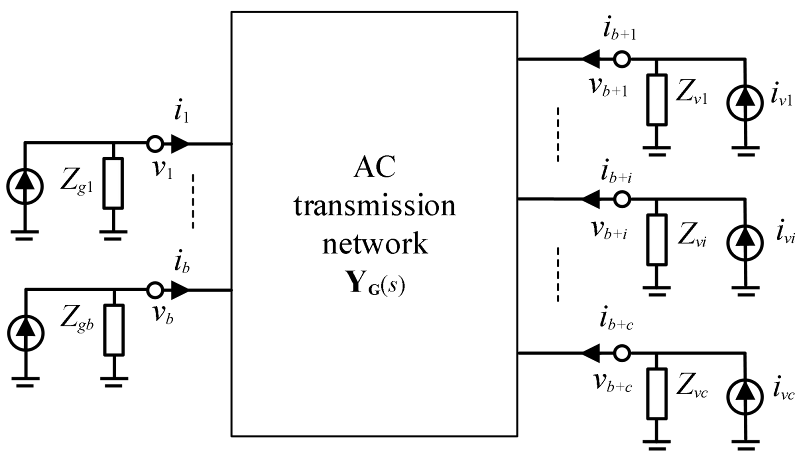

Fig. 5.1. Schematic diagram of multiple VSCs connected to an AC grid.

The circuit in Fig. 5.1 shows the system model of multiple VSCs connected to an AC grid where the AC transmission network is characterised by means of its admittance matrix $\mathbf{Y}_G(s)$ and the different components connected at the grid buses (e.g., the subscript b represents the number of connected equivalent conventional generations and the subscript c represents the number of VSCs) are expressed as the Norton equivalent circuits.

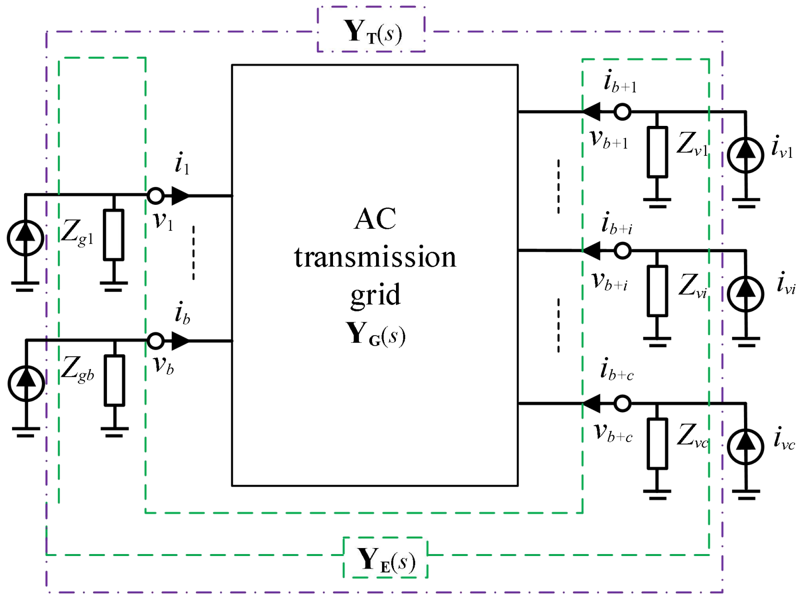

Fig. 5.2. Equivalent diagram of multiple VSCs connected to an AC grid observed from one of the VSCs: a) Equivalent circuit. b) Closed-loop system.

The equivalent system circuit of multiple VSCs connected to an AC grid observed from one of the VSCs can be obtained as shown in Fig. 5.2 a). The relationships between voltages and currents in the AC grid can be expressed as

$$\left.\begin{array}{l}\mathbf{i} = \mathbf{Y_G(s)v} \\ \mathbf{i} = \mathbf{i_E} - \mathbf{Y_E}(s)\mathbf{v}\end{array}\right\} \tag{5-2-1}$$

then the system can be equivalent to the closed-loop system shown in Fig. 5.2 b) and (5-2-1) can be expressed as

$$\boldsymbol{v} = \boldsymbol{Z_T}(s)\boldsymbol{i_E} \tag{5-2-2}$$

where the system equivalent impedance matrix $Z_B(s)$ is the inverse of the admittance node matrix and can be described as

$$\boldsymbol{Z_T}(s) = \boldsymbol{Y_T^{-1}}(s) = (\boldsymbol{Y_G}(s) + \boldsymbol{Y_E}(s))^{-1} \tag{5-2-3}$$

the voltages and currents at the AC grid terminals are $\mathbf{v}^T = [v_1, \ldots, v_n]$ and $\mathbf{i}^T = [i_1, \ldots, i_n]$ with n is equal to the number of buses, the current sources and equivalent admittances of the external components are $\mathbf{i}^T = [0, \ldots, i_{g1}, \ldots, i_{gb}, i_{v1}, \ldots, i_{vi}, \ldots, i_{vc}]$ and $\mathbf{Y_E}(s)$ =diag$\{0, \ldots, Y_{g1}(s), \ldots, Y_{gb}(s), Y_{v1}(s), \ldots, Y_{vc}(s)\}$ where i_{gi} and $Y_{gi}(s) = 1/Z_{gi}(s)$ describe the Norton equivalent circuits of the main AC grids. i_{vi} and $Y_{vi}(s) = 1/Z_{vi}(s)$ characterise the Norton equivalent circuits of the VSC applications ($v = h$, w for HVDC, DG plants and other VSC applications respectively).

5.3 Stability criteria

There are different approaches to assess the stability of multiple VSCs connected to an AC grid in the frequency domain. GNC, determinant impedance-based stability criterion and a proposed new approach are discussed and compared as follows.

5.3.1 Existed stability criteria on assessing multiple VSCs connected to an AC grid in frequency-domain

A. GNC

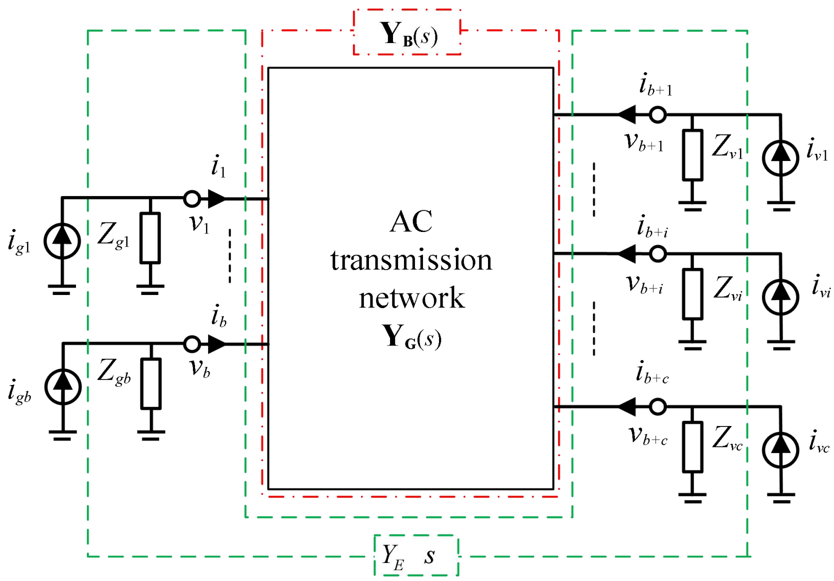

Fig. 5.3. Schematic diagram of multiple VSCs connected to an AC grid in GNC.

Fig. 5.3 shows the system model of multiple VSCs connected to an AC grid in GNC. Stability can be analysed in frequency-domain by rewriting as

$$\boldsymbol{v} = (\boldsymbol{Y_B}(s) + \boldsymbol{Y_E}(s))^{-1}\boldsymbol{i_E} = (\boldsymbol{I} + \boldsymbol{Z_B}(s)\boldsymbol{Y_E}(s))^{-1}\boldsymbol{Z_B}(s)\boldsymbol{i_E} \tag{5-3-1}$$

where $\boldsymbol{I}$ is the identity matrix and $\mathbf{Z_B}(s) = \mathbf{Y_B}^{-1}(s)$ is the grid impedance matrix and $\mathbf{Z_B}(s) = \mathbf{Z_G}(s)$,. Considering that the AC transmission network is passive (i.e., $\mathbf{Z_G}(s)$ is stable), the stability of the closed-loop system in Fig. 5.1 can be assessed by means of the GNC which extends the traditional Nyquist criterion to the Nyquist curves of the eigenvalues of the open-loop transfer function. Compared with state-space eigenvalue analysis, the GNC allows study stability with fewer calculations and data.

B. Determinant impedance-based stability criterion

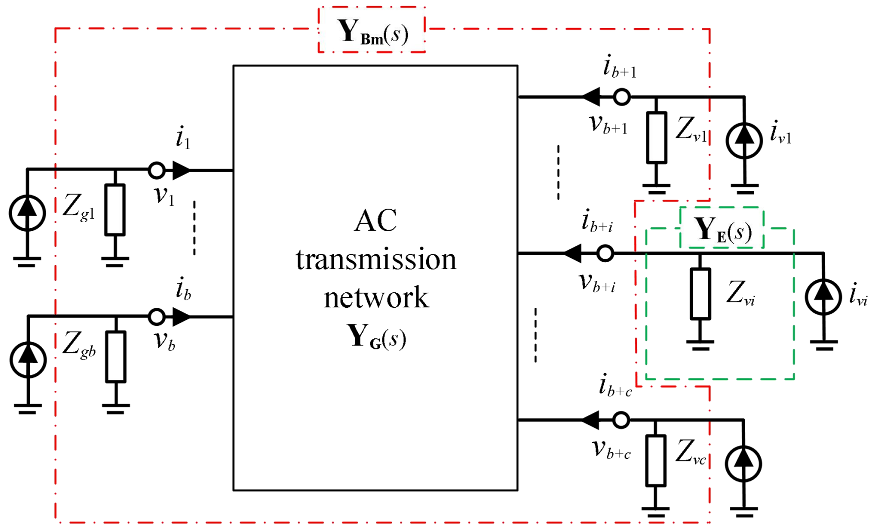

Fig. 5.4. Schematic diagram of multiple VSCs connected to an AC grid in determinant impedance-based stability criterion.

Fig. 5.4 shows the system model of multiple VSCs connected to an AC grid in determinant impedance-based stability criterion, instabilities of the system can be investigated in frequency-domain by using the impedance-based representation of multiple VSCs connected to an AC grid system observed from one of the VSCs. And the equivalent impedance $Z_B(s)$ observed from the VSC side which is equal to the term $b + i$ of the system impedance matrix $\mathbf{Z}_{\mathbf{Bm}}$(s) without the equivalent admittance $Y_{vi}(s)$ of the i^{th} VSC, i.e., $Z_B(s) = Z_{Bm,\,jj}$(s) with $j = b + i$. The impedance-based equivalent circuit in Fig. 5.1 can be represented as the circuit in Fig. 5.4 which is obtained from the transfer function between the sources and the grid voltage v_{b+i} as follows:

$$v_{b+i} = \frac{1}{1/\boldsymbol{Z_B}(s)+\boldsymbol{Y}_{vi}(s)}(v_{\boldsymbol{B}}(s)/\boldsymbol{Z_B}(s) + \boldsymbol{i}_{vi}) = \frac{\boldsymbol{Z_B}(s)}{1+\boldsymbol{Z_B}(s)\boldsymbol{Y}_{vi}(s)}\boldsymbol{i}_E \tag{5-3-2}$$

and stability can be assessed by applying the Nyquist and bode criteria to the open-loop transfer function $L(s) = Z_B(s)Y_{vi}(s) = Z_{Bm,\,jj}(s)Y_{vi}(s)$ with $j = b + i$.

The above approach can assess the stability of the system in Fig. 5.5 by applying the GNC. The AC transmission network and other components connected at the grid buses except that the VSC at terminals b+i can be characterised by means of its admittance matrix $\mathbf{Y}_{\mathbf{Bm}}(s)$ and the equivalent impedance matrix $\mathbf{Z}_{\mathbf{Bm}}(s)$= $\mathbf{Y}_{\mathbf{Bm}}^{-1}(s)$. Then the open-loop transfer function $\mathbf{L}(s) = \mathbf{Z_G}(s)\mathbf{Y_E}(s)$ of the closed-loop system in (5-3-1) can be expressed as

$$\boldsymbol{L}(s) = \boldsymbol{Z_{Bm}}(s)\boldsymbol{Y_E}(s) = \begin{bmatrix} \dots & Z_{Bm,1j}(s) & \dots \\ & \dots & \\ \dots & Z_{Bm,nj}(s) & \dots \end{bmatrix} \begin{bmatrix} 0 & \dots & 0 \\ \vdots & Y_{vi}(s) & \vdots \\ 0 & \dots & 0 \end{bmatrix} \quad (j = b + i) \tag{5-3-3}$$

and the eigenvalues of $\mathbf{L}(s)$ are obtained from the characteristic polynomial

$$\begin{aligned} &\mathrm{Det}\{\boldsymbol{Z}_{\mathrm{Bm}}(s)\boldsymbol{Y_E}(s) - \lambda \boldsymbol{I}\} = Z_{Bm,jj}(s)Y_{vi}(s)\lambda^{n-1} - \lambda^n = 0 \\ &\Rightarrow \lambda = Z_{Bm,jj}(s)Y_{vi}(s) \ (j = b + i) \end{aligned} \tag{5-3-4}$$

which must verify the traditional Nyquist criterion, i.e., the Nyquist criterion applied in (5-3-2). It must be highlighted that in this approach, the impedance-based stability criterion is only feasible if the multiple VSCs connected to an AC grid observed from the VSC is passive (i.e., if $\mathbf{Z_{Bm}}(s)$ is stable) which is not always true due to it contains the other VSCs. It may lead to the wrong result when it is observed from other VSCs.

5.3.2 New approach to assess stability based on GNC

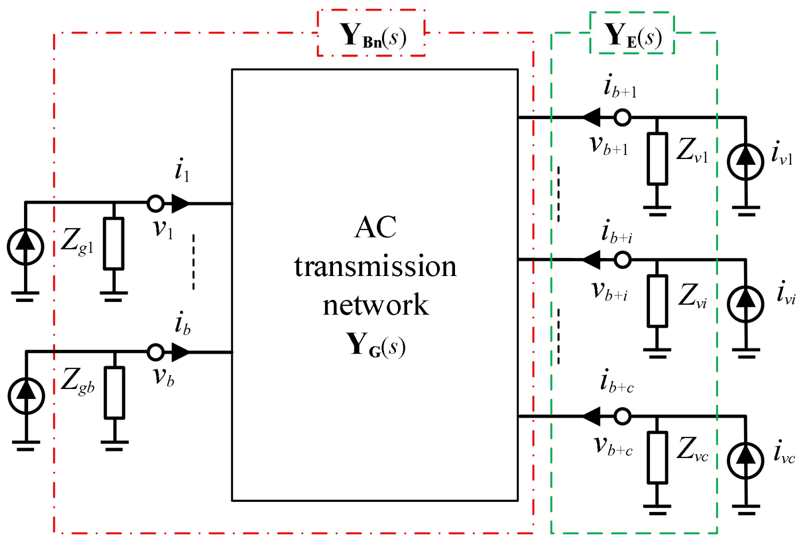

Fig. 5.5. Schematic diagram of multiple VSCs connected to an AC grid in new approach based on GNC.

The GNC allows analysing system stability but the number of the eigenvalues to handle is equal to the number of the system buses which can be very large. On the other hand, the impedance-based stability criterion only studies one eigenvalue because it analyses system stability from one VSC, but this approach may not be feasible because the grid observed from this VSC could not be stable due to other VSCs.

Fig. 5.5 presents the system model of multiple VSCs connected to an AC grid in a new approach. This approach can assess system stability by applying the GNC to the system in Fig. 5.1 where the AC transmission network together with the different components connected at the grid buses except all the VSCs is characterised by means of its admittance matrix $\mathbf{Y_{Bn}}(s)$ and the equivalent impedance matrix $\mathbf{Z_{Bn}}(s) = \mathbf{Y_{Bn}^{-1}}(s)$. In this case, the loop transfer function $\mathbf{L}(s) = \mathbf{Z_G}(s)\mathbf{Y_E}(s)$ of the closed-loop system in (5-3-1) becomes

$$\mathbf{L}(s) = \mathbf{Z}_{\mathbf{B}n}(s)\mathbf{Y_E}(s) = \begin{bmatrix} Z_{Bn,11}(s) & \dots & Z_{Bn,1d}(s) \\ & \dots & \\ Z_{Bn,d1}(s) & \dots & Z_{Bn,dd}(s) \end{bmatrix} \begin{bmatrix} Y_{v1}(s) & \dots & 0 \\ \vdots & \ddots & \vdots \\ 0 & \dots & Y_{vd}(s) \end{bmatrix}, \tag{5-3-5}$$

and the maximum number of eigenvalues of $\mathbf{L}(s)$ is only equal to the number c of VSCs connected to an AC grid. Note that system stability can be correctly assessed with this approach because the AC transmission network together with the different components connected at the grid buses except all the VSCs is passive (i.e., $\mathbf{Z_{Bn}}(s)$ is stable).

5.4 Case study

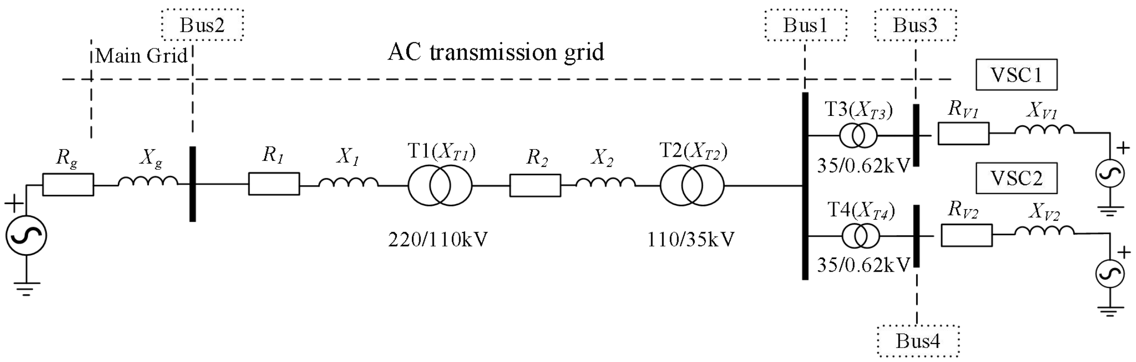

Fig. 5.6. An application of the multiple VSCs connected to an AC grid model.

An example system model of multiple VSCs connected to an AC grid is presented in Fig. 5.6. VSC1 and VSC2 are connected to the main grid by transmission grid including a local and a long-distance transmission line. VSC1 and VSC2 with controlled current sources can represent the output characteristics of WTG1 and WTG2. The symbols of the AC grid and VSCs of WTGs are shown in Table B-5 in Appendix B. Parameters of VSC1 are the same as the parameters of the VSC in Table B-4 in Appendix B. The control scheme and structure of VSC1 and VSC2 are the same as the VSC in the model as shown in Fig. 3.1. Control parameters of VSC2 are also the same as VSC1 except for the bandwidth of the feed-forward voltage low-pass filter. It is concluded in Chapter 4 that when $\omega_{Hf} > 1.2\omega_{Hf,\,ref}$, system stability is increased. Therefore, the bandwidth of the feed-forward voltage low-pass filter of VSC2 is set to 1.3$\omega_{Hf,\ ref}$ to increase its control performance. Since the bandwidth of the feed-forward voltage low-pass filter of VSC2 is different from that of VSC1, the transfer functions of the impedance model of VSC1 and VSC2 are different.

The equivalent model of the example system in Fig. 5.6 is presented in Fig. 5.7. $Z_{g1}(s)$ describes the impedance of the main AC grid, $Z_L(s)$ describes the line impedance between Bus1 and Bus2, $Z_{T3}(s)$ and $Z_{T4}(s)$ represent the impedance of the transformer T3 and T4 respectively, $Z_{v1}(s)$ and $Z_{v1}(s)$ represent the impedance of VSC1 and VSC2 respectively.

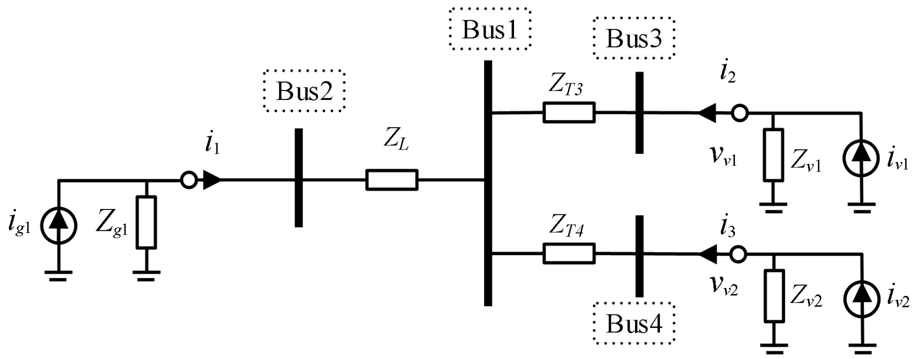

Fig. 5.7. Equivalent model of the example system.

The equivalent system admittance model is then derived from GNC, determinant impedance-based stability criterion and a proposed new approach as follows.

A. GNC

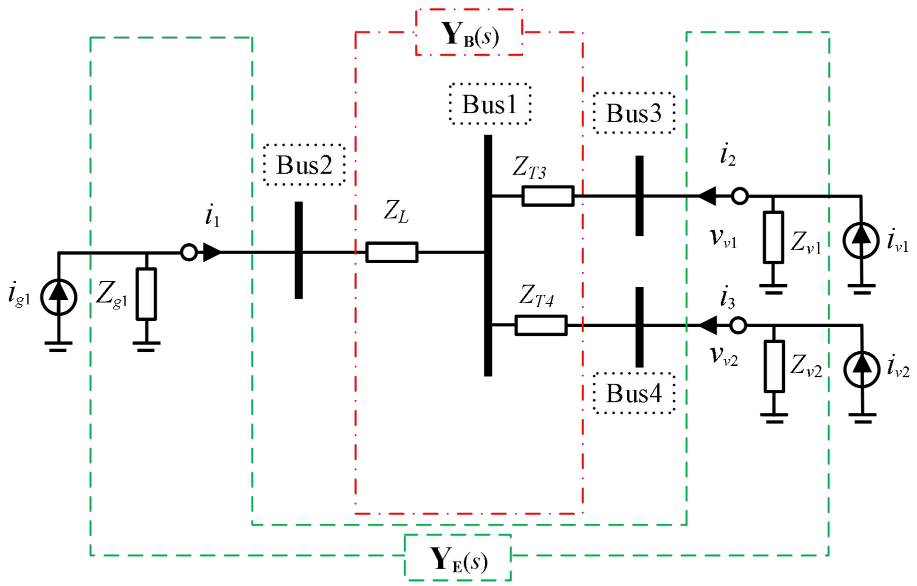

Fig. 5.8. Schematic diagram of the example system in GNC.

The schematic diagram of the example system in GNC is shown in Fig. 5.8. In this case, the open-loop transfer function $\mathbf{L}(s)$ of the studied system can be expressed as

$$
\begin{aligned}
&\boldsymbol{L}(s)=\boldsymbol{Z_B}(s)\boldsymbol{Y_E}(s)\\
&=\begin{bmatrix} Z_{B,11}(s) & Z_{B,12}(s) & Z_{B,13}(s) & Z_{B,14}(s)\\ Z_{B,21}(s) & Z_{B,22}(s) & Z_{B,23}(s) & Z_{B,24}(s)\\ Z_{B,31}(s) & Z_{B,32}(s) & Z_{B,33}(s) & Z_{B,44}(s)\\ Z_{B,41}(s) & Z_{B,42}(s) & Z_{B,43}(s) & Z_{B,44}(s)\end{bmatrix}\begin{bmatrix} 0 & 0 & 0 & 0\\ 0 & Y_{g1}(s) & 0 & 0\\ 0 & 0 & Y_{v1}(s) & 0\\ 0 & 0 & 0 & Y_{v2}(s)\end{bmatrix}\\
&=\begin{bmatrix} Z_L(s)+Z_{T3}(s)+Z_{T4}(s) & -Z_L(s) & -Z_{T3}(s) & -Z_{T4}(s)\\ -Z_L(s) & Z_L(s) & 0 & 0\\ -Z_{T3}(s) & 0 & Z_{T3}(s) & 0\\ -Z_{T4}(s) & 0 & 0 & Z_{T4}(s)\end{bmatrix}\begin{bmatrix} 0 & 0 & 0 & 0\\ 0 & Y_{g1}(s) & 0 & 0\\ 0 & 0 & Y_{v1}(s) & 0\\ 0 & 0 & 0 & Y_{v2}(s)\end{bmatrix}\\
&=\begin{bmatrix} 0 & L_{12}(s) & L_{13}(s) & L_{14}(s)\\ 0 & L_{22}(s) & 0 & 0\\ 0 & 0 & L_{33}(s) & 0\\ 0 & 0 & 0 & L_{44}(s)\end{bmatrix}
\end{aligned}
\tag{5-4-1}
$$

where $Z_{B,\,jj}$(s) (j=1, 2, 3, 4) represents the impedance of the component in the whole system, $Y_{g1}(s)$ represents the equivalent admittance of the main AC grid, $Y_{vi}(s)$ represents equivalent admittance $Y_{vi}(s)$ of the i^{th} VSC. Then the eigenvalues of $\mathbf{L}(s)$ can be calculated as follows:

$$
\begin{aligned}
&Det\{\boldsymbol{Z}_{\text{Bm}}(s)\boldsymbol{Y_E}(s)-\lambda\boldsymbol{I}\}=0\\
&[Z_{B,22}(s)Y_{g1}(s)-\lambda][Z_{B,33}(s)Y_{v1}(s)-\lambda][Z_{B,44}(s)Y_{v2}(s)-\lambda]=0
\end{aligned}
\tag{5-4-2}
$$

B. Determinant impedance-based stability criterion

1) Observed from VSC1

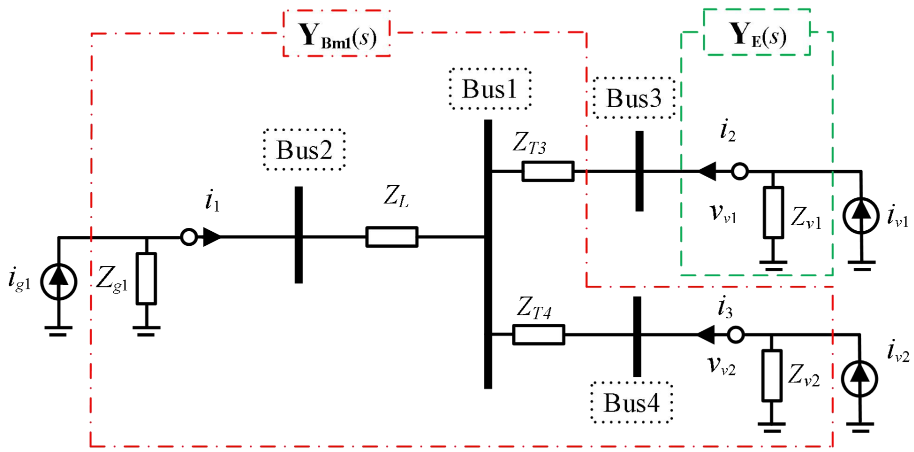

Fig. 5.9. Schematic diagram of the example system in determinant impedance-based stability criterion when observed from VSC1.

The schematic diagram of the example system in determinant impedance-based stability criterion when observed from VSC1 is shown in Fig. 5.9. In this case, the open-loop transfer function $\mathbf{L}(s) = \mathbf{Z_G}(s)\mathbf{Y_E}(s)$ of the closed-loop system in (5-3-1) becomes

$$
\begin{aligned}
&\boldsymbol{L}(s) = \boldsymbol{Z_{Bm1}}(s)\boldsymbol{Y_E}(s) \\
&= \begin{bmatrix} Z_{Bm1,11}(s) & Z_{Bm1,12}(s) & Z_{Bm1,13}(s) & Z_{Bm1,14}(s) \\ Z_{Bm1,21}(s) & Z_{Bm1,22}(s) & Z_{Bm1,23}(s) & Z_{Bm1,24}(s) \\ Z_{Bm1,31}(s) & Z_{Bm1,32}(s) & Z_{Bm1,33}(s) & Z_{Bm1,34}(s) \\ Z_{Bm1,41}(s) & Z_{Bm1,42}(s) & Z_{Bm1,43}(s) & Z_{Bm1,44}(s) \end{bmatrix} \begin{bmatrix} 0 & 0 & 0 & 0 \\ 0 & 0 & 0 & 0 \\ 0 & 0 & Y_{v1}(s) & 0 \\ 0 & 0 & 0 & 0 \end{bmatrix} \\
&= \begin{bmatrix} Z_L(s) + Z_{T3}(s) + Z_{T4}(s) & -Z_L(s) & -Z_{T3}(s) & -Z_{T4}(s) \\ -Z_L(s) & Z_L(s) + Z_{g1}(s) & 0 & 0 \\ -Z_{T3}(s) & 0 & Z_{T3}(s) & 0 \\ -Z_{T4}(s) & 0 & 0 & Z_{T4}(s) + Z_{v2}(s) \end{bmatrix} \begin{bmatrix} 0 & 0 & 0 & 0 \\ 0 & 0 & 0 & 0 \\ 0 & 0 & Y_{v1}(s) & 0 \\ 0 & 0 & 0 & 0 \end{bmatrix} \\
&= \begin{bmatrix} 0 & 0 & L_{13}(s) & 0 \\ 0 & 0 & 0 & 0 \\ 0 & 0 & L_{33}(s) & 0 \\ 0 & 0 & 0 & 0 \end{bmatrix}
\end{aligned} \tag{5-4-3}
$$

where $Z_{Bm1,\,jj}$(s) (j=1, 2, 3, 4) represents the impedance of the component in the whole system, $Yvi(s)$ represents equivalent admittance $Y_{vi}(s)$ of the i^{th} VSC. Then the eigenvalues of $\mathbf{L}(s)$ can be calculated as follows:

$$
\begin{gathered}
\mathrm{Det}\{Z_{\mathrm{Bm}}(s)Y_E(s) - \lambda I\} = 0 \\
[Z_{Bm1,33}(s)Y_{v1}(s)\text{-}\lambda] = 0
\end{gathered} \tag{5-4-4}
$$

2) Observed from VSC2

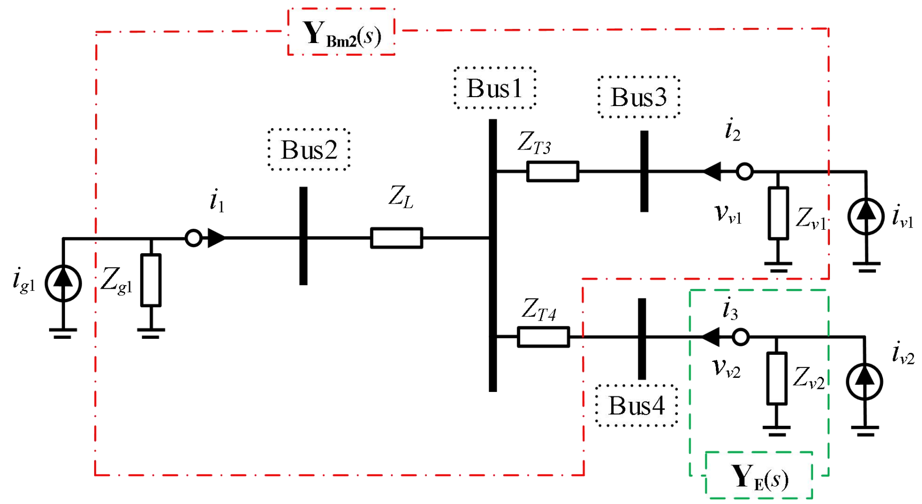

Fig. 5.10. Schematic diagram of the example system in determinant impedance-based stability criterion when observed from VSC2.

The schematic diagram of the example system in determinant impedance-based stability criterion when observed from VSC2 is shown in Fig. 5.10. Then the open-loop transfer function $\mathbf{L}(s) = \mathbf{Z_G}(s)\mathbf{Y_E}(s)$ of the closed-loop system in (5-3-1) becomes

$$
\begin{aligned}
&\boldsymbol{L}(s) = \boldsymbol{Z_{Bm2}}(s)\boldsymbol{Y_E}(s) \\
&= \begin{bmatrix} Z_{Bm2,11}(s) & Z_{Bm2,12}(s) & Z_{m2,13}(s) & Z_{Bm2,14}(s) \\ Z_{Bm2,21}(s) & Z_{Bm2,22}(s) & Z_{Bm2,23}(s) & Z_{Bm2,24}(s) \\ Z_{Bm2,31}(s) & Z_{Bm2,32}(s) & Z_{Bm2,33}(s) & Z_{Bm2,34}(s) \\ Z_{Bm2,41}(s) & Z_{Bm2,42}(s) & Z_{Bm2,43}(s) & Z_{Bm2,44}(s) \end{bmatrix} \begin{bmatrix} 0 & 0 & 0 & 0 \\ 0 & 0 & 0 & 0 \\ 0 & 0 & 0 & 0 \\ 0 & 0 & 0 & Y_{v2}(s) \end{bmatrix} \\
&= \begin{bmatrix} Z_L(s) + Z_{T3}(s) + Z_{T4}(s) & -Z_L(s) & -Z_{T3}(s) & -Z_{T4}(s) \\ -Z_L(s) & Z_L(s) + Z_{g1}(s) & 0 & 0 \\ -Z_{T3}(s) & 0 & Z_{T3}(s) + Z_{v1}(s) & 0 \\ -Z_{T4}(s) & 0 & 0 & Z_{T4}(s) \end{bmatrix} \begin{bmatrix} 0 & 0 & 0 & 0 \\ 0 & 0 & 0 & 0 \\ 0 & 0 & 0 & 0 \\ 0 & 0 & 0 & Y_{v2}(s) \end{bmatrix} \\
&= \begin{bmatrix} 0 & 0 & 0 & L_{14}(s) \\ 0 & 0 & 0 & 0 \\ 0 & 0 & 0 & 0 \\ 0 & 0 & 0 & L_{44}(s) \end{bmatrix}
\end{aligned} \tag{5-4-5}
$$

where $Z_{Bm2,\ jj}$(s) (j=1, 2, 3, 4) represents the impedance of the component in the whole system, $Y_{vi}(s)$ represents equivalent admittance $Y_{vi}(s)$ of the i^{th} VSC, then eigenvalues of $\mathbf{L}(s)$ can be calculated as follows:

$$
\begin{aligned}
&\mathrm{Det}\{\boldsymbol{Z}_{\mathrm{Bm}}(s)\boldsymbol{Y}_E(s) - \lambda \boldsymbol{I}\} = 0 \\
&\left[Z_{Bm2,44}(s)Y_{v2}(s)\text{-}\lambda\right] = 0
\end{aligned} \tag{5-4-6}
$$

C. The new approach

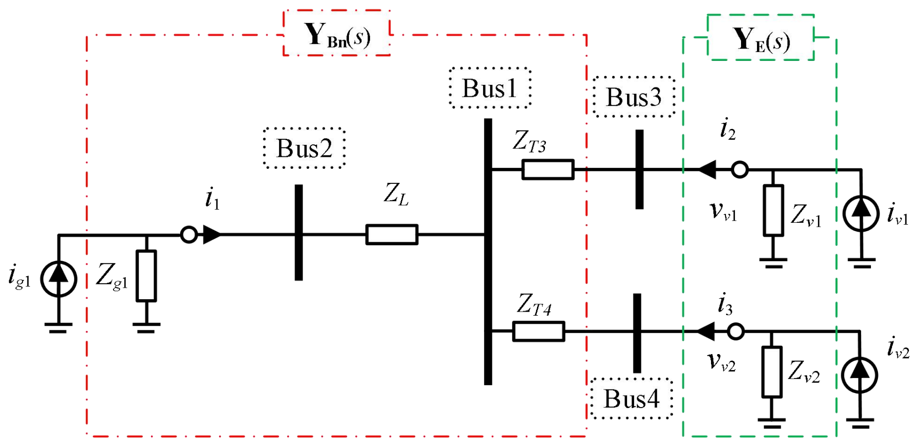

Fig. 5.11. Schematic diagram of the example system in the new approach.

In the new approach, the open-loop transfer function $\mathbf{L}(s)$ of the studied system can be expressed as

$$
\boldsymbol{L}(s)=\boldsymbol{Z}_{Bn}(s)\boldsymbol{Y}_E(s)=\begin{bmatrix} Z_{Bn,11}(s) & Z_{Bn,12}(s) & Z_{Bn,13}(s) & Z_{Bn,14}(s) \\ Z_{Bn,21}(s) & Z_{Bn,22}(s) & Z_{Bn,23}(s) & Z_{Bn,24}(s) \\ Z_{Bn,31}(s) & Z_{Bn,32}(s) & Z_{Bn,33}(s) & Z_{Bn,34}(s) \\ Z_{Bn,41}(s) & Z_{Bn,42}(s) & Z_{Bn,43}(s) & Z_{Bn,44}(s) \end{bmatrix}\begin{bmatrix} 0 & 0 & 0 & 0 \\ 0 & 0 & 0 & 0 \\ 0 & 0 & Y_{v1}(s) & 0 \\ 0 & 0 & 0 & Y_{v2}(s) \end{bmatrix}
$$

$$
=\begin{bmatrix} Z_L(s)+Z_{T3}(s)+Z_{T4}(s) & -Z_L(s) & -Z_{T3}(s) & -Z_{T4}(s) \\ -Z_L(s) & Z_L(s)+Z_{g1}(s) & 0 & 0 \\ -Z_{T3}(s) & 0 & Z_{T3}(s) & 0 \\ -Z_{T4}(s) & 0 & 0 & Z_{T4}(s) \end{bmatrix}\begin{bmatrix} 0 & 0 & 0 & 0 \\ 0 & 0 & 0 & 0 \\ 0 & 0 & Y_{v1}(s) & 0 \\ 0 & 0 & 0 & Y_{v2}(s) \end{bmatrix} \quad (5\text{-}4\text{-}7)
$$

$$
=\begin{bmatrix} 0 & 0 & L_{13}(s) & L_{14}(s) \\ 0 & 0 & 0 & 0 \\ 0 & 0 & L_{33}(s) & 0 \\ 0 & 0 & 0 & L_{44}(s) \end{bmatrix}
$$

where $Z_{Bn,\,jj}$(s) (j=1, 2, 3, 4) represents the impedance of the component in the whole system, $Y_{vi}(s)$ represents equivalent admittance $Y_{vi}(s)$ of the ith VSC. Then eigenvalues of $\mathbf{L}(s)$ can be calculated as follows:

$$
\begin{gathered} \mathrm{Det}\{\mathbf{Z}_{\mathrm{Bm}}(s)\mathbf{Y}_{\mathbf{E}}(s)-\lambda\mathbf{I}\}=0 \\ \left[Z_{Bm2,44}(s)Y_{v2}(s)-\lambda\right]=0 \end{gathered} \quad (5\text{-}4\text{-}8)
$$

Compared to the eigenvalues of the open-loop transfer function $\mathbf{L}$(s) in the traditional GNC, this new method is simpler cause fewer eigenvalues are required to calculate which can be applied usefully in a larger size system with several main AC grids.

5.4.1 Base case

A base case of the example system in Fig. 5.7 is analysed. In this case, 400 WTG1s and 200 WTG2s are connected to an AC grid. Stability is assessed by GNC, determinant-impedance criterion and the new approach respectively. Then the results of GNC, determinant impedance-based stability criterion and the new approach to assess system stability are compared. Fig. 5.12 a) to d) shows the eigenvalues of the open-loop transfer function $\mathbf{L}(s)$ by those three criteria respectively. The GNC verifies the instability results as shown in Fig. 5.12 a) because the curves of one eigenvalue intersect the unit circle, enclosing the (−1,0) point in a clockwise direction. Similarly, the determinant impedance-based stability criterion when observed from VSC1 shown in Fig. 5. 12 b) and the new approach shown in Fig. 5.12 d) also indicate unstable results because the curves of one eigenvalue enclose the (−1,0) point in clockwise direction respectively. However, the result of the determinant impedance-based stability criterion when observed from VSC2 shown in Fig. 5. 12 c) provides an opposite result cause the curves of eigenvalues do not enclose the (−1,0) point.

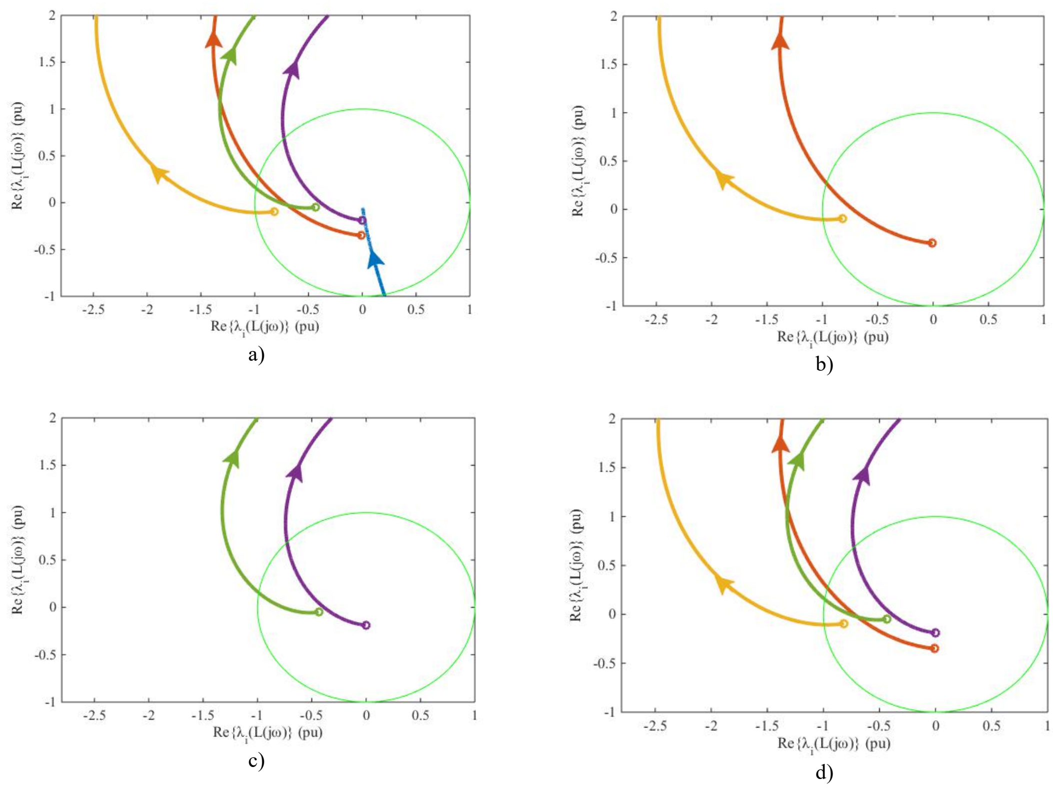

Fig. 5.12. Stability study in a) GNC, b) determinant impedance-based stability criterion when observed from VSC1, c) determinant impedance-based stability criterion when observed from VSC2, d) the new approach.

The stability study is then validated by PSCAD/EMTDC time-domain simulations. In this case, 400 WTG1s and 200 WTG2s are connected to the main AC grid, the input active power of WTG1 (P_{WTG1}) and the input active power of WTG2 (P_{WTG2}) are raised from zero to 10% of each rated power at 2 s. The dynamics of the VSC1, VSC2 and the power of the main grid as shown in Fig. 5.13, Fig. 5.14 and Fig. 5.15 respectively. It is clearly all signals oscillate after 2s, which indicating the system is unstable.

The simulation results validate the correctness of stability results of GNC and the new approach. For determinant impedance-based stability criterion, the stability study result when observed from VSC2 is inconsistent with time-domain simulation results. This indicates the impedance-based stability criterion is not feasible if the multiple VSCs connected to an AC grid system observed from the VSC is not stable ($\mathbf{Z_{Bm}}(s)$ is unstable).

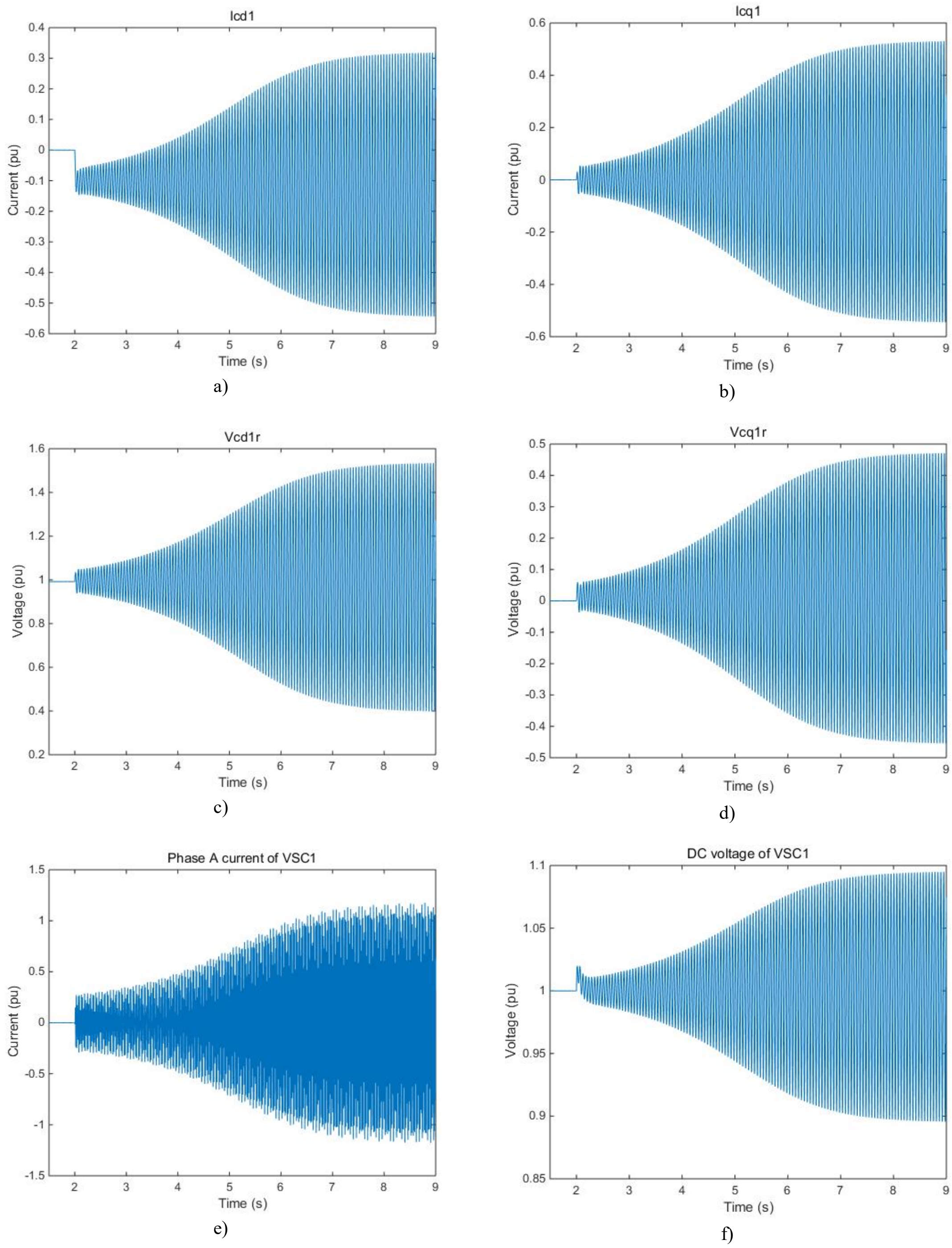

Fig. 5.13. Dynamics of the VSC1 in the time-domain simulation of the base case. a) *d*-axis component of current i_{cd1}. b) *q*-axis component of current i_{cq1}. c) *d*-axis component of reference voltage v_{cd1r}. d) *q*-axis component of reference voltage v_{cq1r}. e) Phase A current. f) DC voltage v_{dc1}.

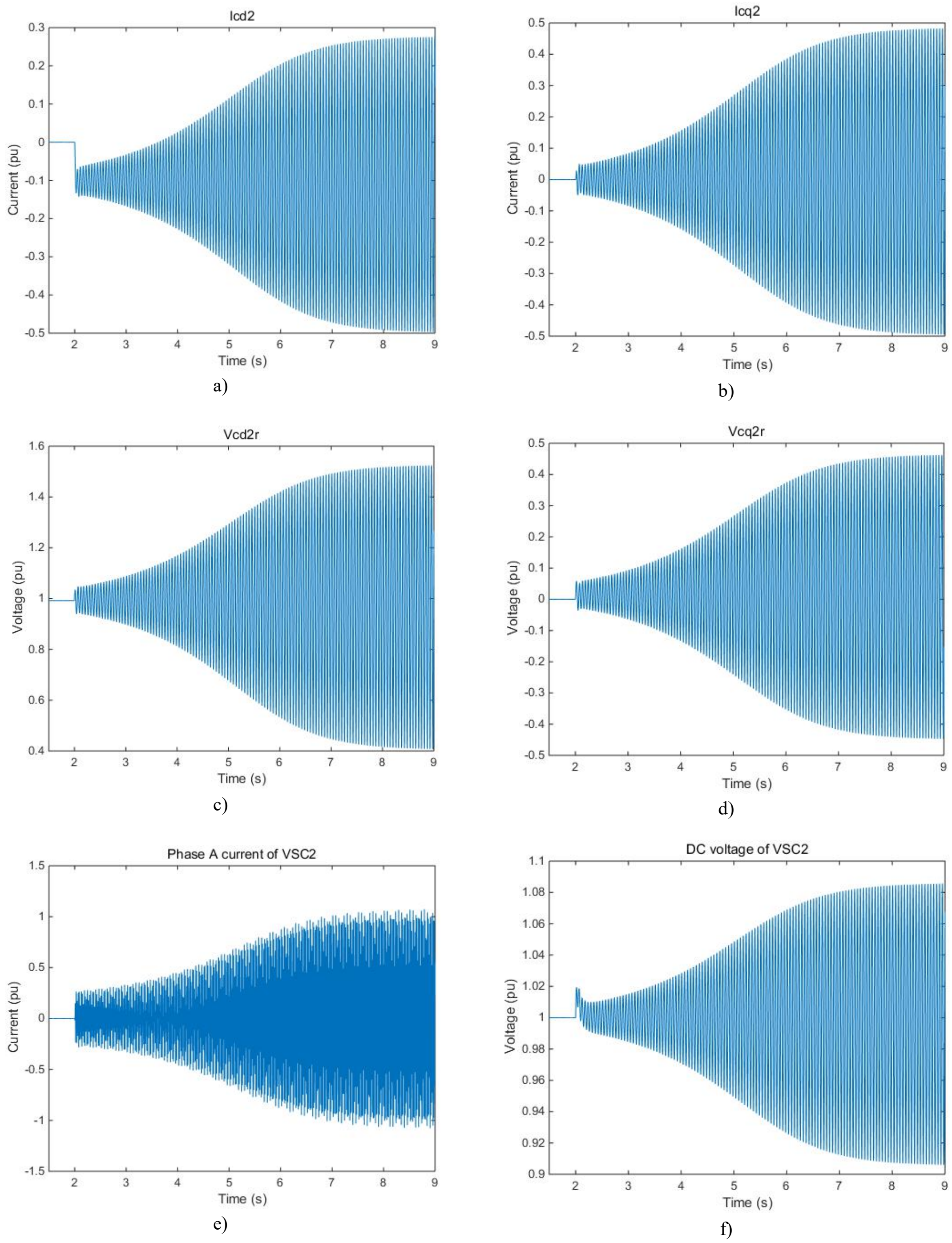

Fig. 5.14. Dynamics of the VSC2 in the time-domain simulation of the base case. a) *d*-axis component of current i_{cd2}. b) *q*-axis component of current i_{cq2}. c) *d*-axis component of reference voltage v_{cd2r}. d) *q*-axis component of reference voltage v_{cq2r}. e) Phase A current. f) DC voltage v_{dc2}.

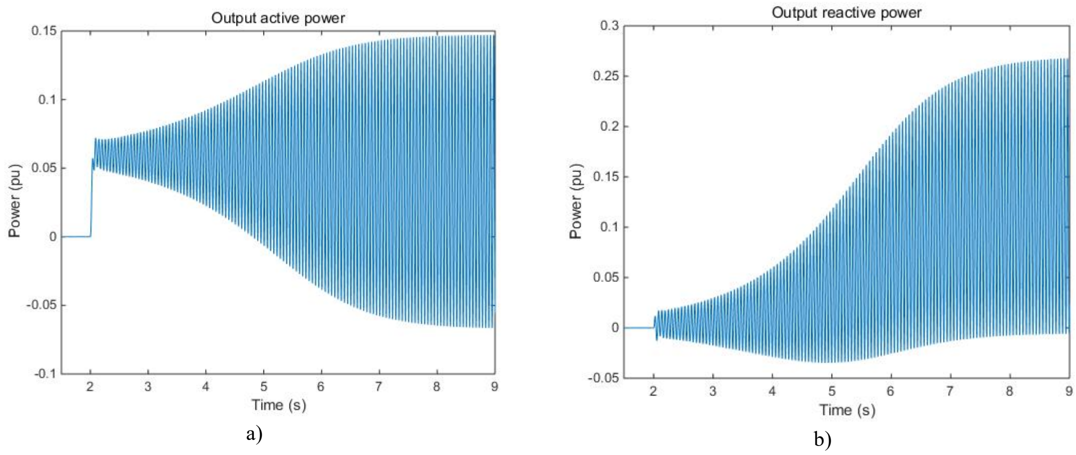

Fig. 5.15. Dynamics of the main grid in the time-domain simulation of the base case. a) Output active power. b) Output reactive power.

Compared with the determinant impedance-based stability criterion, the proposed new approach can investigate system stability more accurately. When compared with traditional GNC, the proposed new approach is easier cause fewer eigenvalues are required which is useful when applied to a larger system.

5.4.2 Changing the number of connected VSCs

1) Case 1

Fig. 5.16 a) and b) show the eigenvalues of the open-loop transfer function **L**(s) by GNC and the new approach respectively when numbers of connected WTG1s N_1=500 and numbers of connected WTG2s N_2=100. GNC and the new approach verifies the instability results as shown in Fig. 5.16 a) and b) because the curves of one eigenvalue intersect the unit circle, enclosing the (−1,0) point in a clockwise direction in each method. Fig. 5.16 c) and d) show the eigenvalues of the open-loop transfer function **L**(s) by GNC and the new approach respectively when N_1=100, N_2=500. GNC and the new approach verify that the system is stable because the curves of eigenvalues do not enclose the (−1,0) point. These results indicate that system stability will be improved when the proportion of WTG2 of total WTGs is increased cause VSC2 in WTG2 has better control performance.

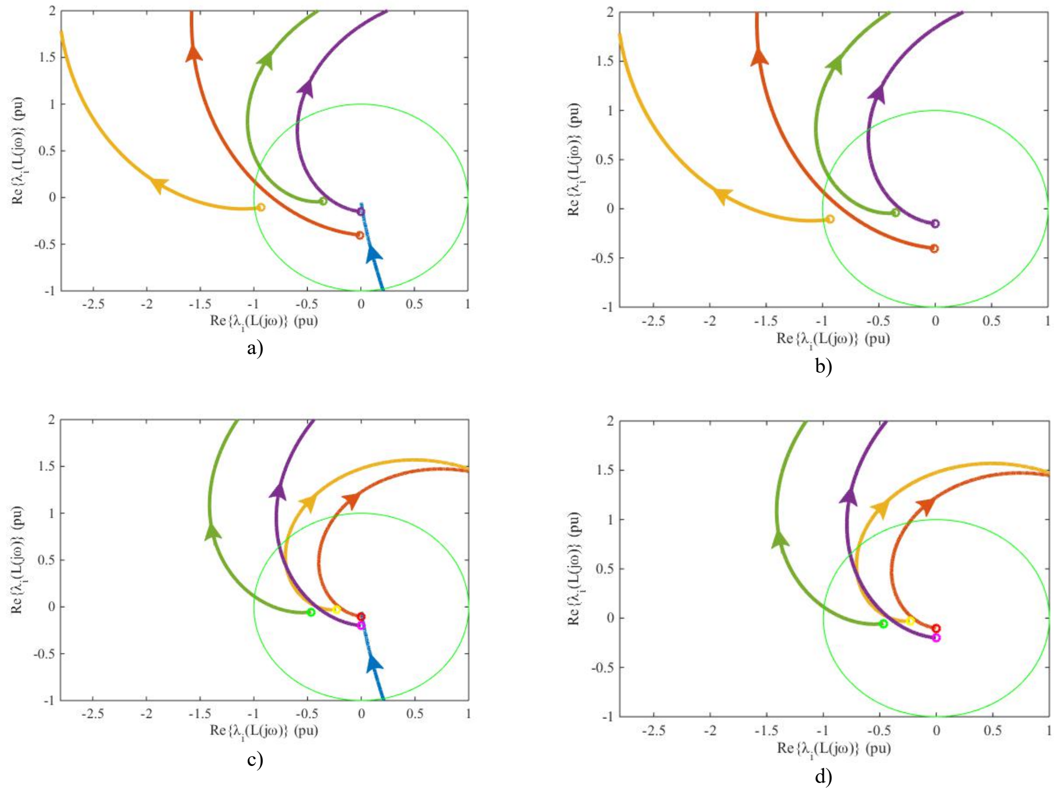

Fig. 5.16. Stability studies: a) in GNC when N_1=500, N_2=100. b) in the new approach when N_1=500, N_2=100. c) in GNC when N_1=100, N_2=500. d) in the new approach when N_1=100, N_2=500.

Dynamics of the VSC1, VSC2 and AC grid in the time-domain simulation of the case with different numbers of connected WTG1s (N_1) and WTG2s (N_2) are shown in Fig. 5.17, Fig. 5.18 and Fig. 5.19. Initially, 500 WTG1s and 100 WTG2s are connected to the AC grid. The output active power of WTG1s and WTG2s ($P_{WTG1}$and P_{WTG2}) is raised from zero to 10% of each rated power respectively at 2 s, then all signals in Fig. 5.17, Fig. 5.18 and Fig. 5.19 oscillate which indicating that the system is unstable. At 4s, N_1 is decreased to 100 and N_2 is increased to 500 at the same time, then the oscillations are suppressed. The simulation results in Fig. 5.17, Fig. 5.18 and Fig. 5.19 validated this hypothesis and the stability analysis results.

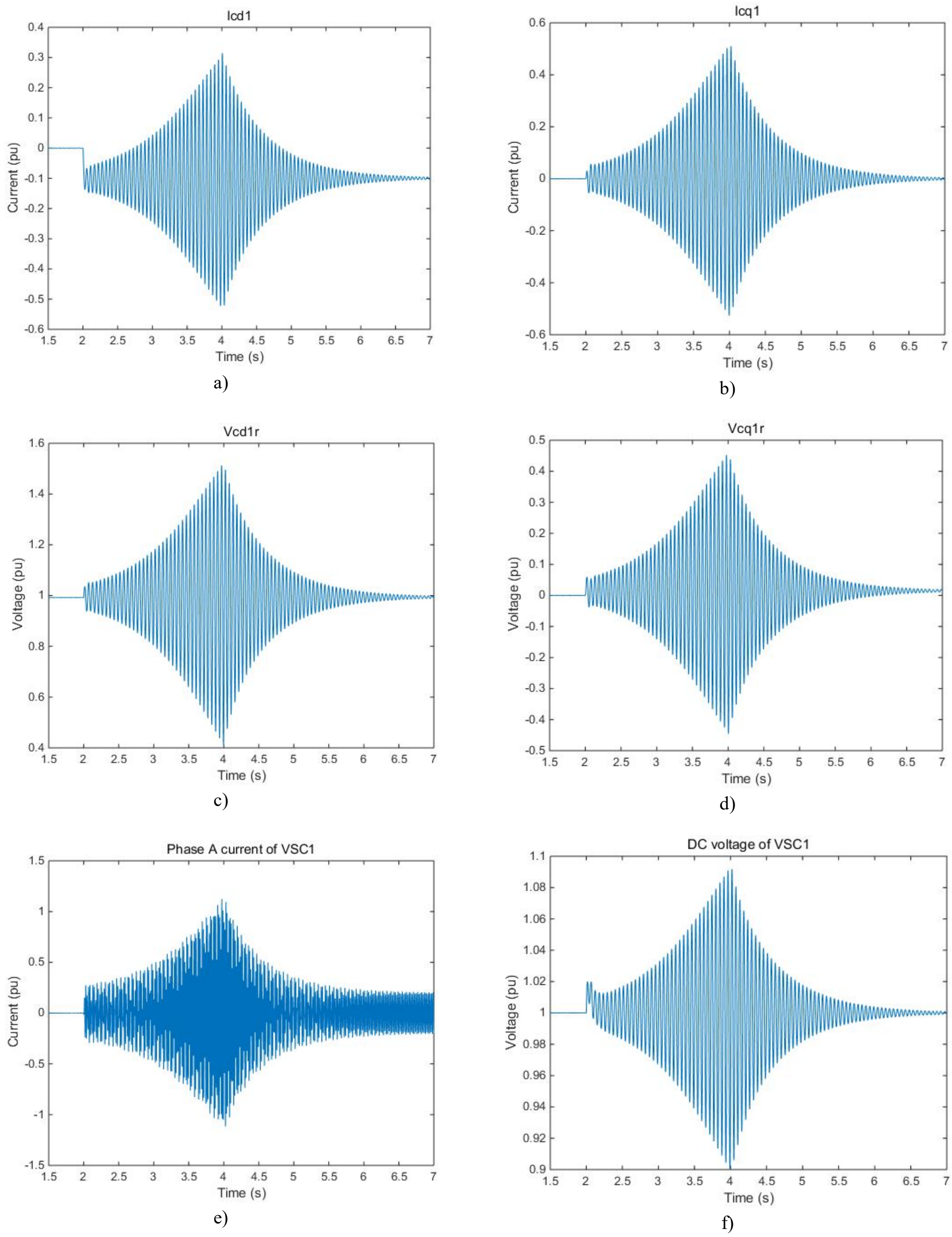

Fig. 5.17. Dynamics of the VSC1 in the time-domain simulation of case 1. a) *d*-axis component of current i_{cd1}. b) *q*-axis component of current i_{cq1}. c) *d*-axis component of reference voltage v_{cd1r}. d) *q*-axis component of reference voltage v_{cq1r}. e) Phase A current. f) DC voltage v_{dc1}.

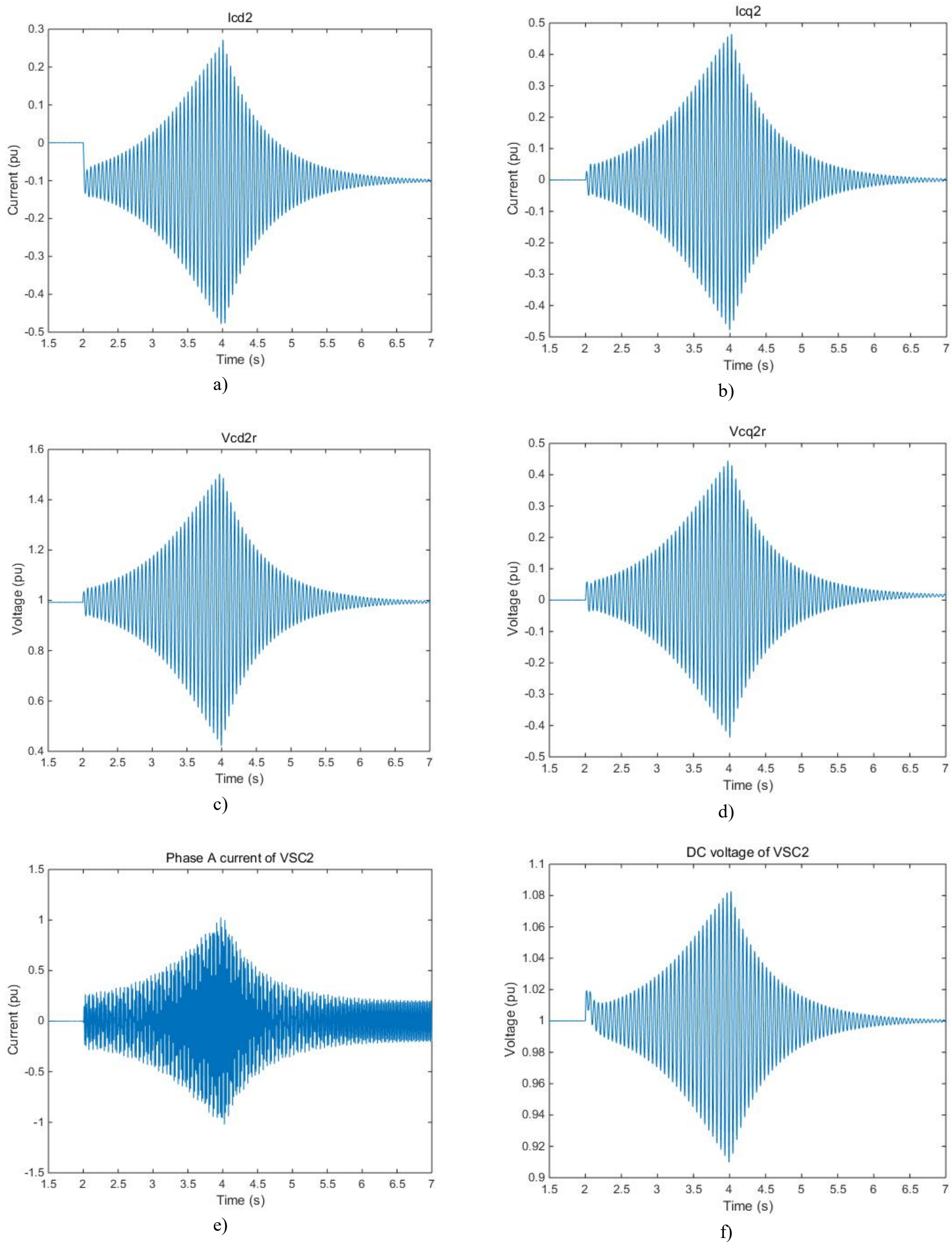

Fig. 5.18. Dynamics of the VSC2 in the time-domain simulation of case 1. a) *d*-axis component of current i_{cd2}. b) *q*-axis component of current i_{cq2}. c) *d*-axis component of reference voltage v_{cd2r}. d) *q*-axis component of reference voltage v_{cq2r}. e) Phase A current. f) DC voltage v_{dc2}.

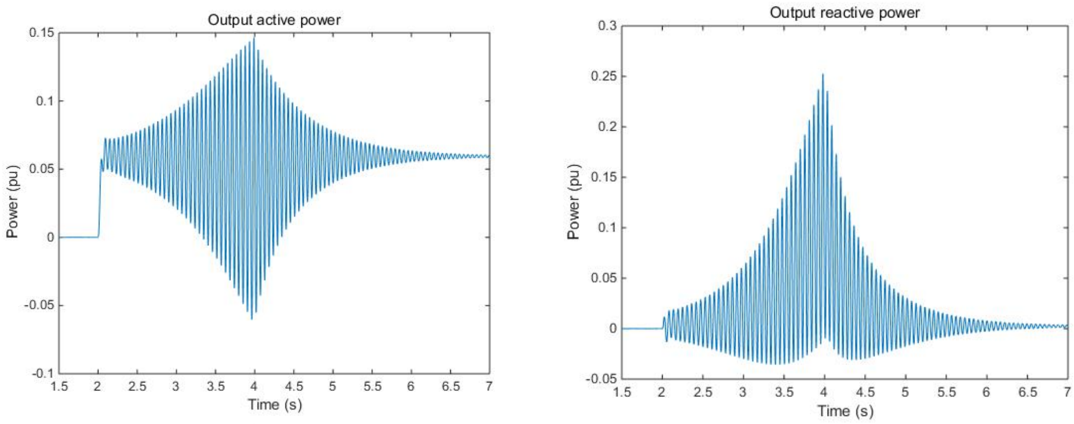

a) b)

Fig. 5.19. Dynamics of the main grid in the time-domain simulation of case 1. a) Output active power. b) Output reactive power.

2) Case 2

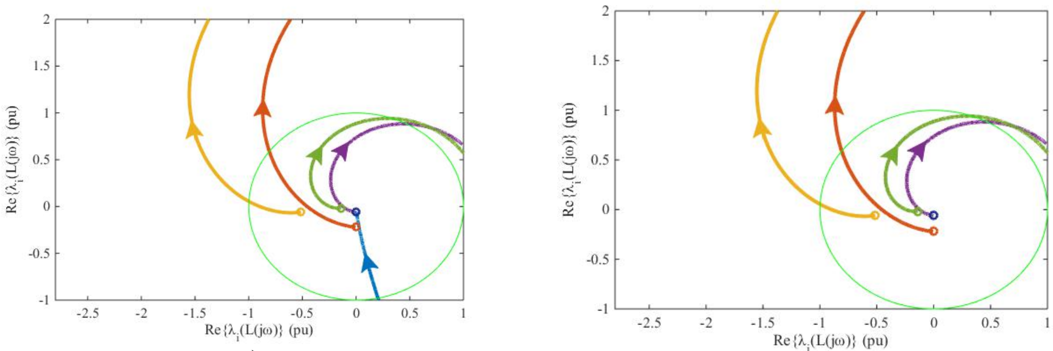

a) b)

Fig. 5.20. Stability studies: a) in GNC when N_1=400, N_2=150. b) in the new approach when N_1=400, N_2=150.

Fig. 5.20 a) and b) show the eigenvalues of the open-loop transfer function $\mathbf{L}(s)$ by GNC and the new approach respectively when numbers of connected WTG1s N_1=400 and numbers of connected WTG2s N_2=150. GNC verifies that the system is stable as shown in Fig. 5.21 a) because the curves of all eigenvalues do not enclose the (−1,0) point in a clockwise direction, and the new approach provides the same stable result as shown in Fig. 5.21 b). Compared with the unstable result in the base case, it indicates that the increment of the numbers of connected VSCs will decrease the system stability.

Dynamics of the VSC1, VSC2 and AC grid in the time-domain simulation of the case with different N_1 and N_2 are shown in Fig. 5.21, Fig. 5.22 and Fig. 5.23. Initially, 400 WTG1s and 150 WTG2s are connected to the AC grid. $P_{WTG1}$and P_{WTG2} are raised from zero to 10% of each rated power respectively at 2 s, it can be seen that the system is stable between 2s to 4s. At 4s, N_2 is increased to 230, then all signals in VSC1, VSC2 and AC grid oscillate which indicating that the system is unstable. At 6.5s, N_2 is decreased to 200, the system oscillates sustainably with a constant amplitude due to reaches the upper hard limit of VSC, but the maximum amplitude of oscillation decreases obviously. The simulation results validated the stability analysis results in Fig. 5.20.

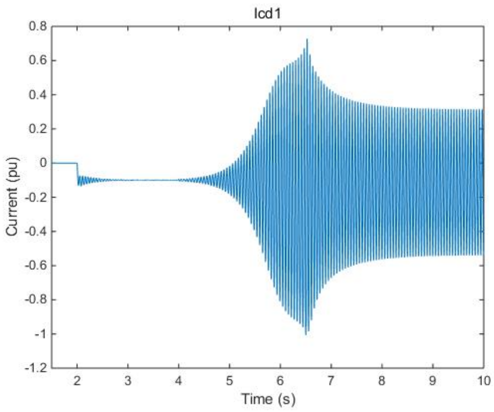

a)

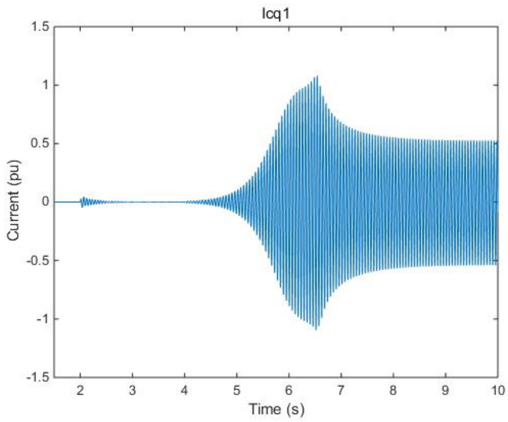

b)

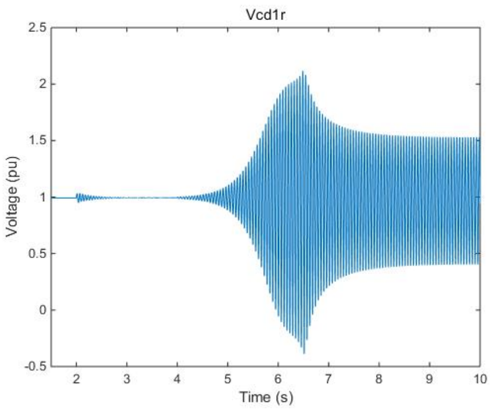

c)

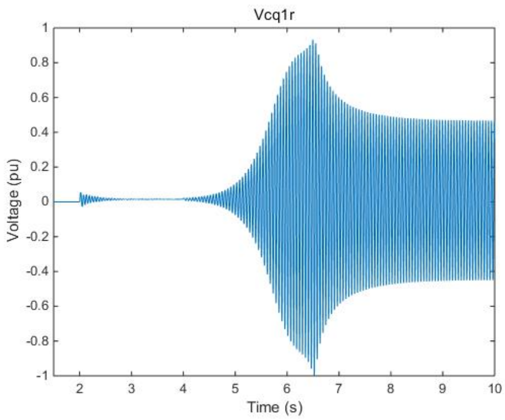

d)

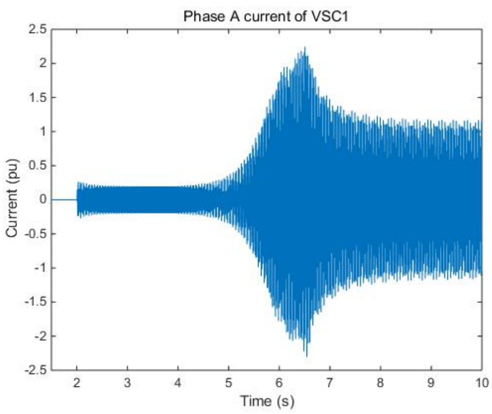

e)

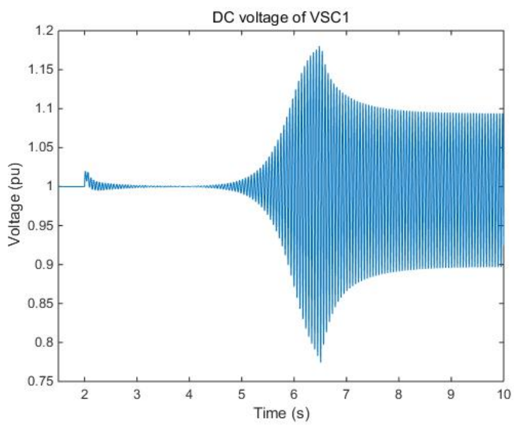

f)

Fig. 5.21. Dynamics of the VSC1 in the time-domain simulation of case 2. a) d-axis component of current i_{cd1}. b) q-axis component of current i_{cq1}. c) d-axis component of reference voltage v_{cd1r}. d) q-axis component of reference voltage v_{cq1r}. e) Phase A current. f) DC voltage v_{dc1}.

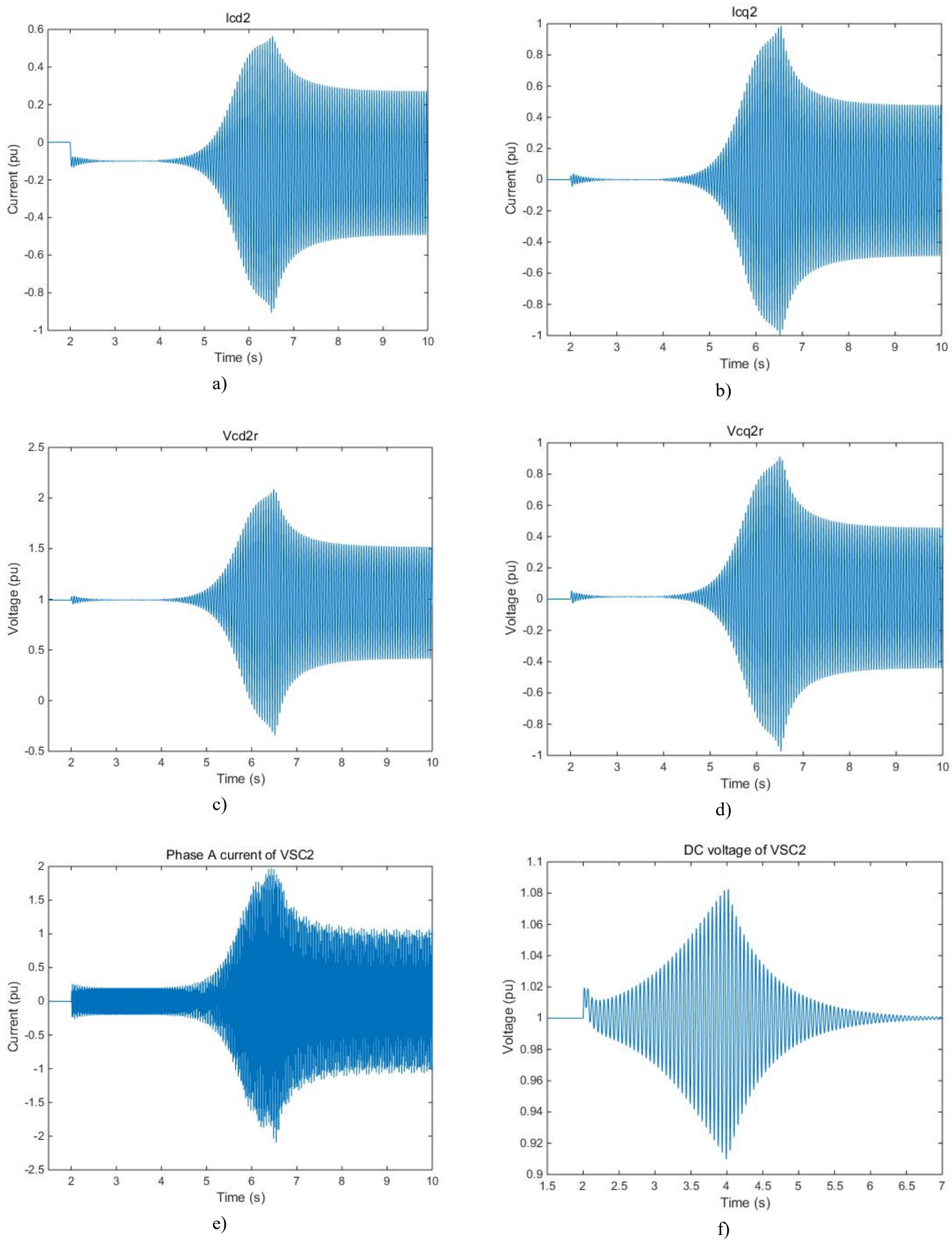

Fig. 5.22. Dynamics of the VSC2 in the time-domain simulation of case 2. a) d-axis component of current i_{cd2}. b) q-axis component of current i_{cq2}. c) d-axis component of reference voltage v_{cd2r}. d) q-axis component of reference voltage v_{cq2r}. e) Phase A current. f) DC voltage v_{dc2}.

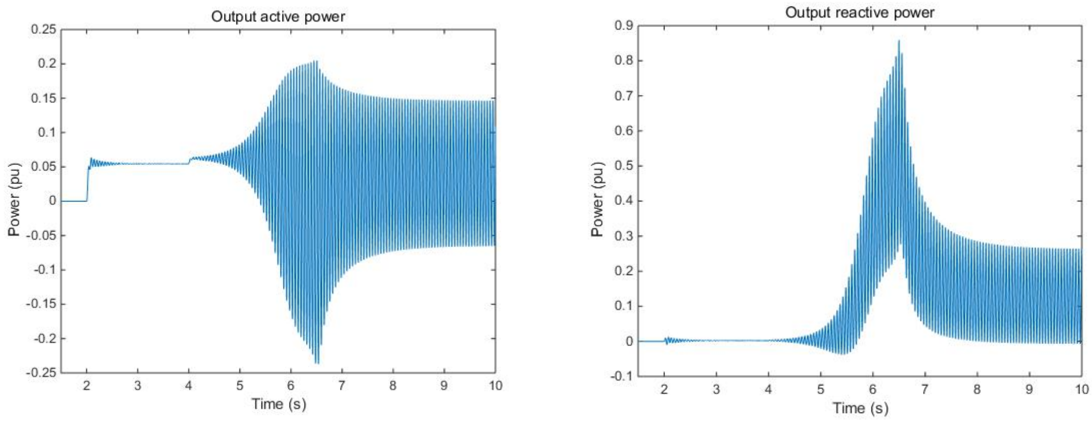

a) b)

Fig. 5.23. Dynamics of the main grid in the time-domain simulation of case 2. a) Output active power. b) Output reactive power.

5.4.3 Changing line reactance

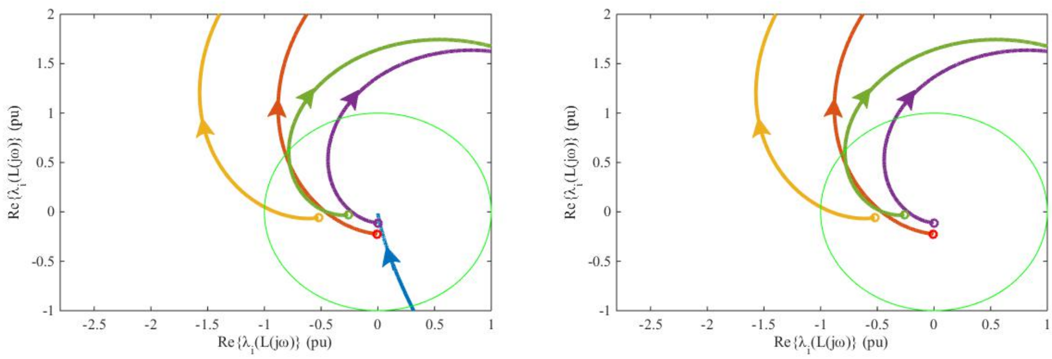

a) b)

Fig. 5.24. Stability studies: a) GNC when F_X=0.9. b) in the new approach when F_X=0.9.

Fig. 5.24 a) and b) show the eigenvalues of the open-loop transfer function $\mathbf{L}(s)$ by GNC and the new approach respectively when F_X (coefficient of line reactance) is equal to 0.9 which is lower than the $F_X = 1$ in the base case. GNC and the new approach verify that the system is stable because the curves of all eigenvalues do not enclose the (−1,0) point in a clockwise direction. Compared with the unstable results in the base case, it indicates that the increment of line reactance will decrease the system stability.

Dynamics of the VSC1, VSC2 and AC grid in the time-domain simulation of the case with different F_X are shown in Fig. 5.25, Fig. 5.26 and Fig. 5.27. In this case, 400 WTG1s and 200 WTG2s are connected to the AC grid. P_{WTG1} and P_{WTG2} are raised from zero to 10% of each rated power at the same time at 2 s and F_X=0.9 initially, it can be seen that the system is stable between 2s to 4s. At 4s, F_X is increased to 1.1, then all signals in VSC1, VSC2 and AC grid oscillate which indicating that the system is unstable. At 6.5s, F_X is decreased to 1, the system oscillates sustainably with a constant amplitude due to reaches the upper hard limit of VSC, but the maximum amplitude of oscillation decreases obviously. The simulation results validated the stability analysis results that the increment of the numbers of connected VSCs will decrease the system stability.

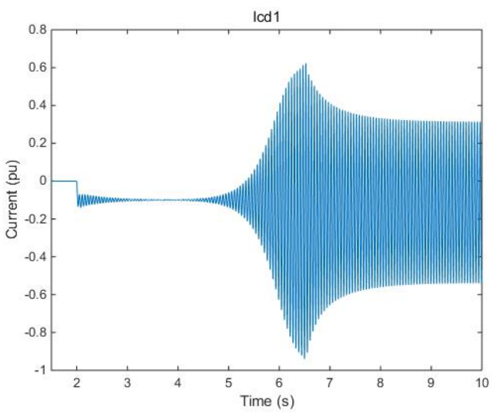

a)

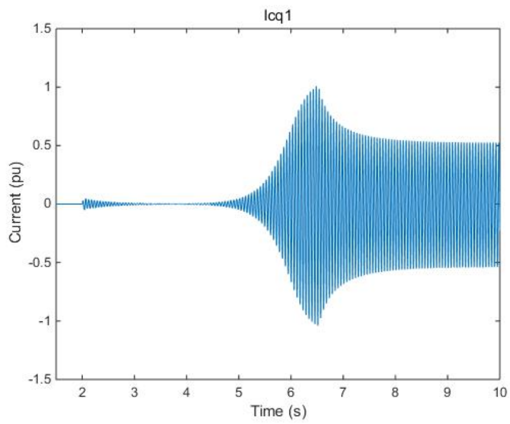

b)

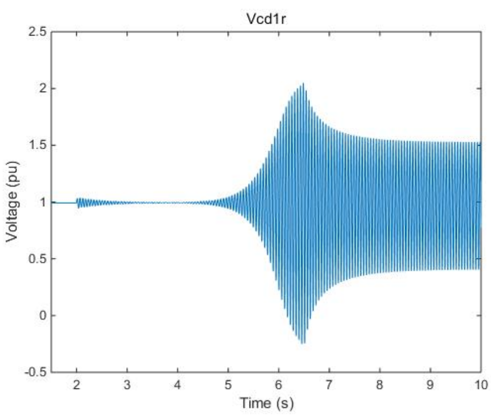

c)

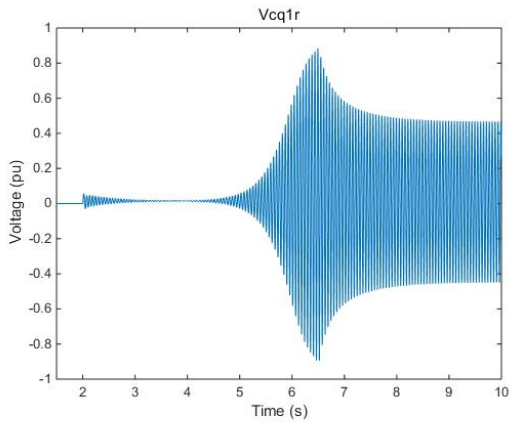

d)

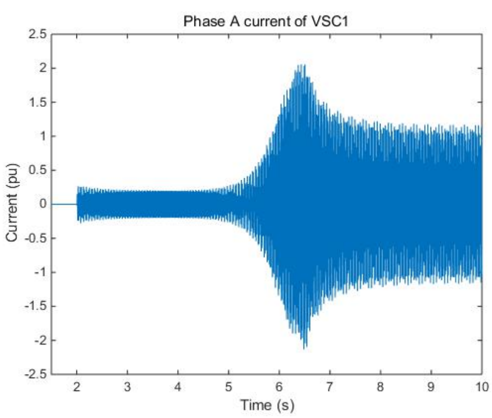

e)

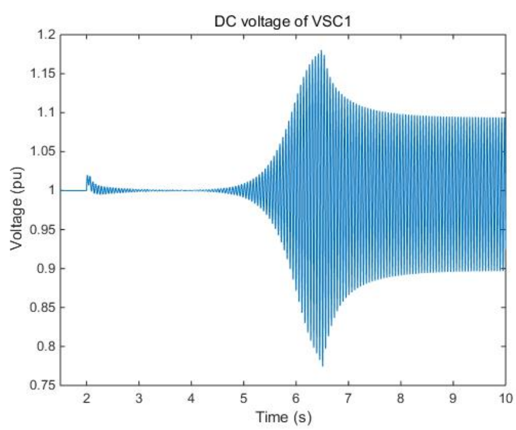

f)

Fig. 5.25. Dynamics of the VSC1 in the time-domain simulation when changing line reactance. a) d-axis component of current i_{cd1}. b) q-axis component of current i_{cq1}. c) d-axis component of reference voltage v_{cd1r}. d) q-axis component of reference voltage v_{cq1r}. e) Phase A current. f) DC voltage v_{dc1}.

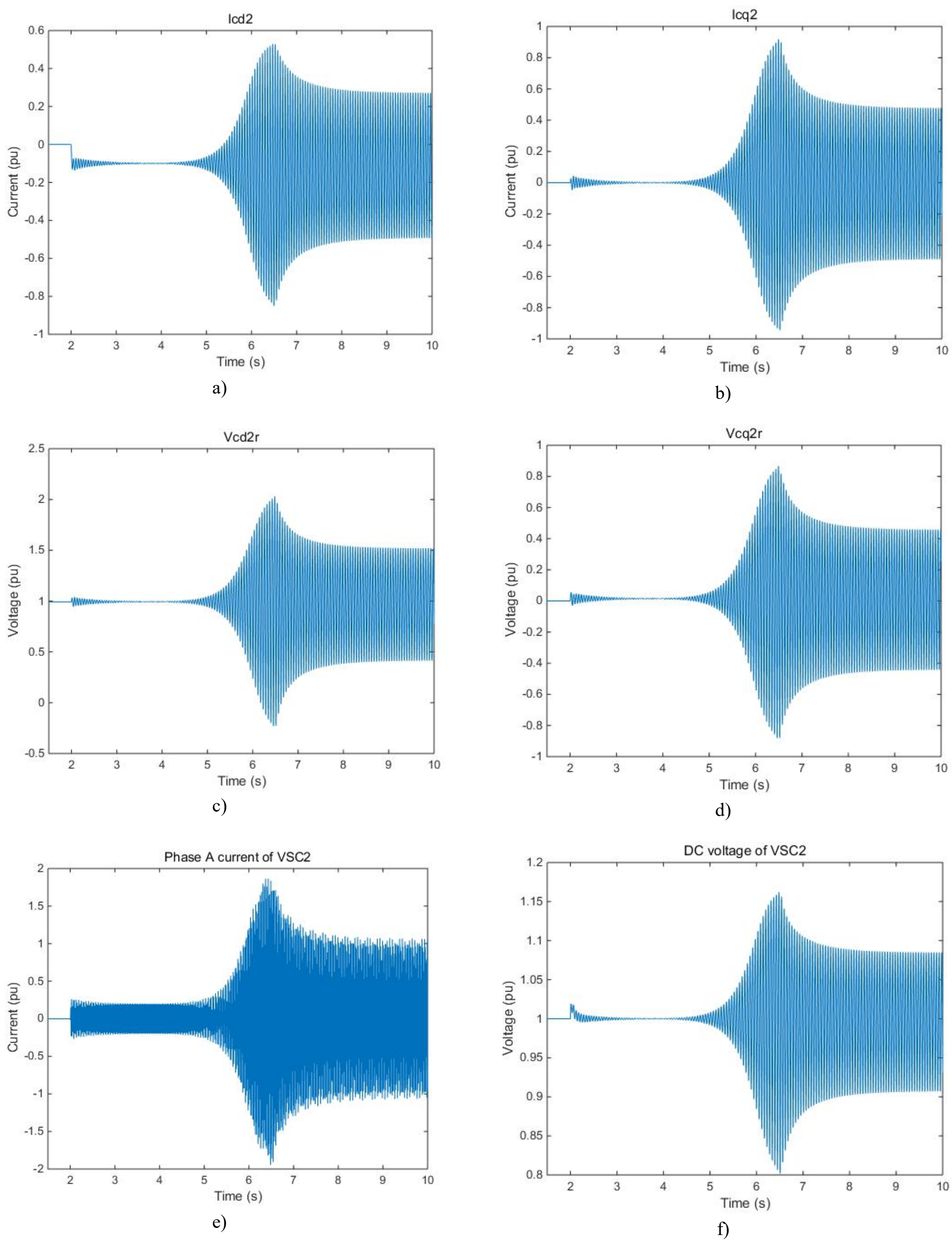

Fig. 5.26. Dynamics of the VSC2 in the time-domain simulation when changing line reactance. a) d-axis component of current i_{cd2}. b) q-axis component of current i_{cq2}. c) d-axis component of reference voltage v_{cd2r}. d) q-axis component of reference voltage v_{cq2r}. e) Phase A current. f) DC voltage v_{dc2}.

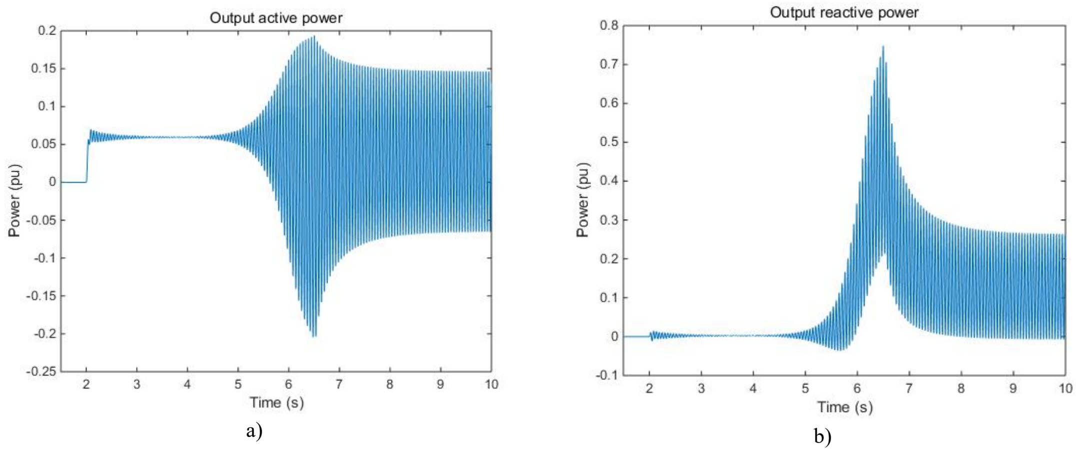

Fig. 5.27. Dynamics of the main grid in the time-domain simulation when changing line reactance. a) Output active power. b) Output reactive power.

5.5 Summary

In this chapter, a new VSC admittance-based model of multiple VSCs connected to an AC grid is proposed to study system stability. Based on the equivalent Norton admittance matrix, the proposed model characterises both the AC-side and DC-side dynamics by relating the AC-side and DC-side current and voltage. The proposed admittance matrix model can be extended for the modelling of large-scale hybrid AC/DC grids.

GNC and the determinant impedance-based stability criterion are usually used to assess system stability but the drawbacks of these two criteria are noticeable. GNC requires the admittance of all components in the system including main grids, AC transmission network and WTGs which is complicated when utilised in a large-scale system. And the impedance-based stability criterion is only feasible when the multiple VSCs connected to an AC grid observed from the VSC is passive which is not always true due to it contains the other VSCs. A new approach is proposed that overcoming these drawbacks. Compared to GNC, the new approach required fewer eigenvalues of the system open-loop transfer function which can simplify the calculation to assess system stability. Compared to the impedance-based stability criterion, the new approach ensures the accuracy in different scenarios.

An example system (two VSCs connected to an AC grid) is analysed using GNC, determinant impedance-based stability criterion and the new approach respectively. The results show the correctness of the new approach and indicate the inapplicability of the determinant impedance-based stability criterion under specific conditions.

The effects of the number of grid-connected WTGs and transmission line reactance on system stability are investigated. With the increment of the number of grid-connected WTGs and transmission line reactance, system stability will be decreased. When the total number of the grid-connected WTGs is constant, the increment of the proportion of VSCS with better control performance will enhance the system stability. Stability analysis results are verified by PSCAD/EMTDC time-domain simulations.

Chapter 6

Conclusions

6.1 General Conclusions

Increased application of VSC-based power electronic devices is foreseen in the future transmission grids. However, a new type of SSI may occur due to the interaction between VSC-based power electronic devices and its connected weak AC grid. The work in this thesis focuses on analysing the mechanism and characteristics of this new type of SSI.

6.1.1 Modelling of the single VSC connected to an AC grid

A system model of the single VSC connected to an AC grid was proposed. Based on the system structure, operation mode and control parameters, the state-space model and impedance model of the system model were established and compared. Compared with the impedance model, the state-space model requires detailed information for all elements in the system which is not always completely available so the impedance model in frequency-domain was finally utilised for the stability analysis. The correctness of the impedance model was verified in PSCAD time-domain simulation by applying an example system.

6.1.2 Stability analysis of the single VSC connected to an AC grid

Generalised Nyquist Criterion (GNC), eigenvalue analysis and determinant-impedance criterion were discussed and utilised to assess the system stability in Chapter 4, and the analysis results were verified by time-domain simulations. The effects of different factors on system stability were summarised as:

1) Low short circuit ratio (SCR) due to the increment of transmission line reactance or the number of online WTGs will decrease system stability. However, if line reactance and the number of connected WTGs both change, the status and modes of system stability are approximately the same as long as SCR (related to the product of line reactance and the number of connected WTGs) of the systems does not change.

2) Compared with the other researchers' methods, a larger frequency range of the bandwidths of VSC control loops was considered. With the increment of the bandwidth of feed-forward voltage low-pass filter ω_f, VSC outer loop ω_{dc} or PLL ω_{pll}, system stability will be decreased firstly and then be improved after a certain frequency. When

the bandwidth of the VSC inner loop ω_{cc} is increased, the system stability will be increased.

The mathematical mechanism of analysis of the newly found SSI was investigated. The oscillation mechanism is generally considered to be due to the negative resistance effect in most research. However, from the impedance-frequency curves of the determinant D(s) of the proposed system impedance model, the unstable system is equivalent to a capacitive impedance with a small positive resistance and then forms a resonant circuit with the power grid that leads to the risk of electrical resonance, which against the opinion that SSI is just caused of negative resistance effect. The physical mechanism of SSI was also illustrated from the Bode plots of the open-loop transfer function of the system. It showed that the disturbance signal would be amplified through the close-loop from VSC *q*-axis voltage v_{sq} to VSC *q*-axis current i_d which would lead to the system instability.

6.1.3 Stability analysis of the multiple VSCs connected to an AC grid

A VSC admittance-based model of multiple VSCs connected to an AC grid was proposed in Chapter 4 to analyse SSI in the multiple VSCs connected to an AC grid. The proposed model characterises both the AC-side and DC-side dynamics based on the equivalent Norton admittance method. The feasibility of GNC and the determinant impedance-based stability criterion in multiple VSCs connected to an AC grid were discussed. GNC requires the admittance of all components in the system including main grids, AC transmission network and WTGs which is complicated when utilised in a large-scale system. For impedance-based stability criterion, the limitation is that it is only feasible when the multiple VSCs connected to an AC grid observed from the VSC is passive which is not always true due to it contains the other VSCs. A new approach was proposed that overcoming the drawbacks of the other two criteria which requires fewer eigenvalues of the system open-loop transfer function than GNC and has better feasibility than impedance-based stability criterion. An example system of two VSCs connected to an AC grid was analysed using GNC, determinant impedance-based stability criterion and the new approach respectively. The stability analysis results illustrated the drawbacks of GNC, determinant impedance-based stability criterion and the advantages of the new approach. The effects of the number of grid-connected WTGs and transmission line reactance on system stability are investigated. With the increment of the number of grid-connected WTGs and transmission line reactance, system stability will be decreased. When the total number of the grid-connected WTGs is constant, the increment of the proportion of VSCs with better control performance will enhance the system stability. The stability analysis results are verified by PSCAD/EMTDC time-domain simulations.

6.2 Contributions of the research work

The main contributions of this thesis are summarised as follows:

- Implementation of impedance-based system model of the single VSC connected to an AC grid to analyse SSI characteristics.
- Investigated the effects of VSC control loops bandwidths on system stability considering a larger frequency range than most research.
- Studied the mathematical and physical mechanism of the SSI in the single VSC connected to an AC grid which was less studied in the previous research.
- Proposed a VSC admittance-based model of multiple VSCs connected to an AC grid and provided a systematic procedure based on the Norton admittance method.
- Designed a new approach which overcomes the drawbacks of traditional GNC and impedance-based stability criterion when analysing SSI in the multiple VSCs connected to an AC grid system.

6.3 Future work

The following future work is outlined:

- An experimental test-rig could be designed to further investigate the newly found SSI when relevant data can be obtained.
- Effects of different control modes of VSCs on system stability and the interactions among different VSCs could be further analysed.
- The proposed VSC admittance-based model of multiple VSCs connected to an AC grid could be extended to a more complicated model including multiple main grids to analyse SSI.
- Suppression methods of SSI could be designed.

- The system instability problems in other frequency ranges such as low frequency and high frequency could be studied.

Publications

1. **X. Li**, J. Liang, G. Li and T. Joseph, "Modeling and Stability Analysis of the Subsynchronous Interactions in Weak AC Grids with Wind Power Integration," *2018 53rd International Universities Power Engineering Conference (UPEC)*, Glasgow, UK, 2018, pp. 1-6. doi: 10.1109/UPEC.2018.8541852.
2. **X. Li**, A. Gayan, L. YAO, et al. Recent development and prospect of offshore wind power in Europe[J]. Journal of Global Energy Interconnection, 2019, 2(2): 116-126 (in Chinese).
3. **X. Li**, J. Liang, L. Sainz, G. Li, and G. Wu, " Stability Analysis of the Subsynchronous Interactions in wind farms connected to the Weak AC Grid," *to be submitted to CSEE Journal of Power and Energy Systems*.

References

[1] "IEEE Subsynchronous Resonance Working Group. Terms, definitions and symbols for subsynchronous oscillations," *IEEE Transactions on Power Apparatus and Systems*, 1985, 104(6): 1326-1334.

[2] C Concordia, G K Carter. "Negative damping of electrical machinery," *Transactions of the American Institute of Electrical Engineers*, 1941, 60(3): 116- 119.

[3] J W Butler, C Concordia. "Analysis of series capacitor application problems," *Transactions of the American Institute of Electrical Engineers*, 1937, 56(8): 975- 988.

[4] D N Walker, C E J Bowler, R L Jackson, et al., "Results of subsynchronous resonance test at Mohave," *IEEE Transactions on Power Apparatus and Systems*, 1975, 94(5): 1878-1889.

[5] N. Sönnichsen, "Installed wind power capacity - worldwide 2001-2019[Online]," https://www.statista.com/statistics/268363/installed-wind-power-capacity worldwide/#statisticContainer

[6] REN21, "Renewables 2016 - Global Status Report," 2016.

[7] M. D. Esteban, J. J. Diez, J. S. López, and V. Negro,"Why offshore wind energy, " *Renew. Energy*, vol. 36, no. 2, pp. 444–450, 2011.

[8] Global Wind Energy Council, "Offshore Wind," 2015.

[9] EWEA, "Wind energy scenarios for 2020," 2014.

[10] EWEA, "Wind energy scenarios for 2030," 2015.

[11] EWEA, "The European offshore wind industry - key 2015 trends and statistics," 2016.

[12] "Renewable Energy Capacity Statistics," *International Renewable Energy Agency (IRENA)*, March, 2020.

[13] "Renewables 2020 - Global Status Report," *Renewable Energy Policy Network for 21 stcentury (REN21)*, May, 2020.

[14] B. Kroposki, et al., "Achieving a 100% Renewable Grid: Operating Electric Power Systemswith Extremely High Levels of Variable Renewable Energy," *IEEE Power & Energy Mag*, vol.15, no. 2, pp. 61-73, April, 2017.

[15] D. van Hertem, O. Gomis-Bellmunt, and J. Liang (eds.), "HVDC Grids: For Offshore and Supergrid of the Future," USA: Wiley, 2017.

[16] Electricity Networks Strategy Group, "Our Electricity Transmission Network: A Vision for 2020," 2012.

[17] Available:https://assets.publishing.service.gov.uk/government/uploads/system/uploads/attachment_data/file/48274/4263-ensgFull.pdf.[Accessed:12-Feb-2014]

[18] ENTSO. E, "Technologies for transmission systems," *Ten-Year Network Development Plan (TYNDP)*, 2017. [Online], Available: http://tyndp.entsoe.eu/2016/insight-reports/technology/. [Accessed: 14-Jan-2017].

[19] M. P. Bahrman and B. K. Johnson, "The ABCs of HVDC transmission technologies," *IEEE Power & Energy Mag*, vol.5, no. 2, pp 32-44, 2007.

[20] D. Tiku, "dc Power Transmission: Mercury-Arc to Thyristor HVDC Valves [History]," *IEEE Power & Energy Mag*, vol.12, no. 2, pp 76 -96, 2014.

[21] D. Jovcic and K. Ahmed, "High Voltage Direct Current Transmission: Converters, Systems and DC Grids," Wiley-Blackwell, 2015.

[22] N. R. Chaudhuri, B. Chaudhuri. R. Majumder, and A. Yazdani, "Multi-terminal Direct Current Grids: Modeling, Analysis, and Control," *Wiley-IEEE Press*, Oct. 2014.

[23] M. Brien, et al. "New Zealand bipolar HVDC earth/sea return operation-environmental experiences," *CIGRÉ sessions 2006,* no. B4-206, 2006.

[24] R. Hong, "Architecture of Nan'ao multi-terminal VSC-HVDC system and its multi-functional control, "*CSEE Journal of Power and Energy Systems,* vol. 1, no.1, pp. 9-18, March 2015.

[25] E. Giraldo and A. Garces, "An adaptive control strategy for a wind energy conversion system based on PWM-CSC and PMSG," *IEEE Trans. Power Syst.*, vol. 29, no. 3, pp. 1446–1453, May 2014.

[26] K. W. Hu and C. M. Liaw, "Development of a wind interior permanent-magnet synchronous generator-based micro grid and its operation control," *IEEE Trans. Power Electron.*, vol. 30, no. 9, pp. 4973–4985, Sep. 2015.

[27] Y. Zhou and H. Nian, "Current zero crossing duration reduction of a semi-controlled open winding PMSG system based on third harmonic current injection," *IEEE Trans. Ind. Electron.*, vol. 63, no. 2, pp. 750–760,Feb. 2016.

[28] M. Zhao, X. Yuan, J. Hu and Y. Yan, "Voltage Dynamics of Current Control Time-Scale in a VSC-Connected Weak Grid," in *IEEE Transactions on Power Systems*, vol. 31, no. 4, pp. 2925-2937, July 2016.

[29] X. Xie, X. Zhang, H. Liu, H. Liu, Y. Li and C. Zhang, "Characteristic Analysis of Subsynchronous Resonance in Practical Wind Farms Connected to Series-Compensated

Transmissions," in *IEEE Transactions on Energy Conversion*, vol. 32, no. 3, pp. 1117-1126, Sept. 2017.

[30] G. Wu et al., "Analysis and design of vector control for VSC-HVDC connected to weak grids," in *CSEE Journal of Power and Energy Systems*, vol. 3, no. 2, pp. 115-124, June 2017.

[31] J. Lv, P. Dong, G. Shi, X. Cai, H. Rao, and J. Chen, "Subsynchronous oscillation of large DFIG-based wind farms integration through MMC-based HVDC," in *Proc. Int. Conf. Power System Technol.*, 2014, pp. 2401–2408.

[32] C. Zou et al., "Analysis of resonance between a VSC-HVDC converter and the AC grid,"in *IEEE Trans. Power Electron.*, vol. 33, no. 12, pp. 10157–10168, Dec. 2018.

[33] R.C. Wang, "Review on Countermeasures for Sub-Synchronous Oscillations in Power Systems," *Power System and Clean Energy*, vol. 27, no. 2, pp. 47-51, Feb. 2011.

[34] H. A. Mohammadpour, M. M. Islam, E. Santi and Y. J. Shin, "SSR Damping in Fixed-Speed Wind Farms Using Series FACTS Controllers," in *IEEE Transactions on Power Delivery*, vol. 31, no. 1, pp. 76-86, Feb. 2016.

[35] L. Wang, X. Xie, Q. Jiang, H. Liu, Y. Li, and H. K. Liu, "Investigation of SSR in practical DFIG-based wind farms connected to a series-compensated power system," *IEEE Trans. Power Syst.*, vol. 30, no. 5,pp. 2772–2779, Sep. 2015.

[36] H. Liu, X. Xie, C. Zhang, Y. Li, H. Liu and Y. Hu, "Quantitative SSR Analysis of Series-Compensated DFIG-Based Wind Farms Using Aggregated RLC Circuit Model," in *IEEE Transactions on Power Systems*, vol. 32, no. 1, pp. 474-483, Jan. 2017.

[37] M. A. Chowdhury, M. A. Mahmud, W. Shen and H. R. Pota, "Nonlinear Controller Design for Series-Compensated DFIG-Based Wind Farms to Mitigate Subsynchronous Control Interaction," in *IEEE Transactions on Energy Conversion*, vol. 32, no. 2, pp. 707-719, June 2017.

[38] J. Adams, V. A. Pappu, and A. Dixit, "ERCOT experience screening for sub-synchronous control interaction in the vicinity of series capacitor banks," in *Proc. IEEE Power & Energy Soc. General Meeting*, pp. 1–5, 2012.

[39] L. Fanand, Z. Miao, "Mitigating SSR using DFIG-based wind generation," in *IEEE Trans. Sustain. Energy*, vol. 3, no. 3, pp. 349–358, Jul. 2012.

[40] W. Ren and E. Larsen, "A refined frequency scan approach to subsynchronous control interaction (SSCI) study of wind farms,"in *IEEE Trans.Power Syst.*, vol. 31, no. 5, pp. 3904–3912, Sep. 2016.

[41] P. Huang, M. E. Moursi, W. Xiao and J. Kirtley, "Subsynchronous resonance mitigation for series-compensated DFIG-based wind farm by using two-degree-of-freedom control strategy," in *IEEE Trans. Power Syst.*, vol. 30, no. 3, pp. 1442–1454, May 2015.

[42] H. Mohammadpour and E. Santi, "SSR damping controller design and optimal placement in rotor-side and grid-side convertors of series-compensated DFIG-based wind farm," in *IEEE Trans. Sustain. Energy*, vol. 6, no. 2, pp. 388–399, Apr. 2015.

[43] ABB Inc., "ERCOT CREZ Reactive Power Compensation Study," Dec. 2010.

[44] Y. Li, H. Liu, X. Chen, J. Hao and L. Yu, "Impact of PMSG on SSR of DFIGs connected to series-compensated lines based on the impedance characteristics," in *The Journal of Engineering*, vol. 2017, no. 13, pp. 2184-2187, 2017.

[45] L. Wang, X. Xie, Q. Jiang, H. Liu, Y. Li and H. Liu, "Investigation of SSR in Practical DFIG-Based Wind Farms Connected to a Series-Compensated Power System," in *IEEE Transactions on Power Systems*, vol. 30, no. 5, pp. 2772-2779, Sept. 2015.

[46] J. Hu, H. Yuan and X. Yuan, "Modeling of DFIG-Based WTs for Small-Signal Stability Analysis in DVC Timescale in Power Electronized Power Systems," in *IEEE Transactions on Energy Conversion*, vol. 32, no. 3, pp. 1151-1165, Sept. 2017.

[47] Mitra and D. Chatterjee, "Active power control of DFIG-based wind farm for improvement of transient stability of power systems," in *IEEE Trans. Power Syst.*, vol. 31, no. 1, pp. 82–93, Jan. 2016.

[48] L. Fan and Z. Miao, "Mitigating SSR using DFIG-based wind generation," in *IEEE Trans. Sustain. Energy*, vol. 3, no. 3, pp. 349–358, Jul. 2012.

[49] L. Sainz, J. J. Mesas, L. Monjo, J. Pedra and M. Cheah-Mané, "Electrical resonance instability study in wind power plants," *2016 Electric Power Quality and Supply Reliability (PQ)*, Tallinn, 2016, pp. 139-144.

[50] F. Gao, Q. He, Z. Hao and B. Zhang, "The research of sub synchronous oscillation in PMSG wind farm," *2016 IEEE PES Asia-Pacific Power and Energy Engineering Conference (APPEEC)*, Xi'an, 2016, pp. 1883-1887.

[51] T. Bi, et al., "Study on response characteristics of grid-side converter controller of PMSG to sub-synchronous frequency component, " in *IET Renewable Power Generation*, vol. 11, no. 7, pp. 966-972, 2017.

[52] X. Zhu and Z. Pan, "Study on the influencing factors and mechanism of SSR due to DFIG-based wind turbines to a series compensated transmission system," in *Proc. 2017 IEEE 26th Int. Symp. Ind. Electron.*, Jun. 2017, pp. 1029–1034.

[53] M. A. Chowdhury and G. M. Shafiullah, "SSR mitigation of seriescompensated DFIG wind farms by a nonlinear damping controller using partial feedback linearization," in *IEEE Trans. Power Syst.*, vol. PP, no. 99, p. 1, 2017.

[54] C. V. Rohit, P. B. Darji and H. R. Jariwala, "Mitigation of IGE using STATCOM with DFIGs," *2018 IEEE International Conference on Power Electronics, Drives and Energy Systems (PEDES)*, Chennai, India, 2018, pp. 1-6.

[55] J. Kavil Kambrath, M. S. U. Khan, Y. Wang, A. I. Maswood and Y. Yoon, "A Novel Control Technique to Reduce the Effects of Torsional Interaction in Wind Turbine System," in *IEEE Journal of Emerging and Selected Topics in Power Electronics*, vol. 7, no. 3, pp. 2090-2105, Sept. 2019.doi: 10.1109/JESTPE.2018.2884407

[56] P. S. Zadehkhost, F. Howell, X. Lin and L. Wang, "Analyzing subsynchronous torsional interactions in large-scale power systems in frequency domain," *2017 IEEE Power & Energy Society Innovative Smart Grid Technologies Conference (ISGT)*, Washington, DC, USA, 2017, pp. 1-5.

[57] Velpula, R. Thirumalaivasan and M. Janaki, "Stability Analysis on Torsional Interactions of Turbine-Generator Connected With DFIG-WECS Using Admittance Model," in *IEEE Transactions on Power Systems*, vol. 35, no. 6, pp. 4745-4755, Nov. 2020.

[58] H. Baker, G. E. Boukarim, R. D'Aquila and R. J. Piwko, "Subsynchronous resonance studies and mitigation methods for series capacitor applications," *2005 IEEE Power Engineering Society Inaugural Conference and Exposition in Africa*, Durban, 2005, pp. 386-392.

[59] R. A. Achilles, "Predicting shaft torque amplification," in *IEEE Transactions on Power Systems*, vol. 10, no. 1, pp. 407-412, Feb. 1995.

[60] Y. Luo, T. Bi, T. Zhang and Q. Yang, "Impact of fault clearing time on shaft torque amplification in series compensated system," *2008 Third International Conference on Electric Utility Deregulation and Restructuring and Power Technologies*, Nanjing, China, 2008, pp. 709-713.

[61] P. Zhang, S. Xiao, T. Bi, W. Zheng and L. Kong, "Analysis of shaft torque amplification caused by interaction between AC and DC system," *2013 IEEE PES Asia-Pacific Power and Energy Engineering Conference (APPEEC)*, Hong Kong, China, 2013, pp. 1-5.

[62] Q. Li, Y. Hu, Y. Wang, C. Zhou, Y. Li and J. Han, "Design and Simulation of a Novel Subsynchronous Control Interaction Damping Controller," *2020 Asia Energy and Electrical Engineering Symposium (AEEES)*, Chengdu, China, 2020, pp. 391-395. doi: 10.1109/AEEES48850.2020.9121520

[63] M. Beza and M. Bongiorno, "On the Risk for Subsynchronous Control Interaction in Type 4 Based Wind Farms," in *IEEE Transactions on Sustainable Energy*, vol. 10, no. 3, pp. 1410-1418, July 2019.doi: 10.1109/TSTE.2018.2889181

[64] G. Revel and D. M. Alonso, "Subsynchronous control interactions in power systems with several wind farms," *2017 XVII Workshop on Information Processing and Control (RPIC)*, Mar del Plata, Argentina, 2017, pp. 1-6.

[65] L. Wang, Z. Lu, J. Peng and X. Sun, "Influences on subsynchronous control interaction from different wind turbine generators," *IECON 2017 - 43rd Annual Conference of the IEEE Industrial Electronics Society*, Beijing, China, 2017, pp. 4944-4948.

[66] A. R. Messina, S. C. A. Rivera, S. D. Olguin and V. D. Ruiz, "Development of advanced analytical techniques for the analysis of subsynchronous torsional interaction with FACTS devices," *PowerTech Budapest 99. Abstract Records. (Cat. No.99EX376)*, Budapest, Hungary, 1999, pp. 275-.

[67] S. Velpula, R. Thirumalaivasan and M. Janaki, "Stability Analysis on Torsional Interactions of Turbine-Generator Connected With DFIG-WECS Using Admittance Model," in *IEEE Transactions on Power Systems*, vol. 35, no. 6, pp. 4745-4755, Nov. 2020.

[68] P. S. Zadehkhost, F. Howell, X. Lin and L. Wang, "Analyzing subsynchronous torsional interactions in large-scale power systems in frequency domain," *2017 IEEE Power & Energy Society Innovative Smart Grid Technologies Conference (ISGT)*, Washington, DC, USA, 2017, pp. 1-5.

[69] R. Mahmud, A. Hoke and J. White, "Impact of Aggregated PV on Subsynchronous Torsional Interaction," *2020 47th IEEE Photovoltaic Specialists Conference (PVSC)*, Calgary, AB, Canada, 2020, pp. 0342-0347.

[70] X. Liu, L. Jiao and Q. Qi, "Analysis of subsynchronous torsional interactions with static Var Compensators," *Proceedings. International Conference on Power System Technology*, Kunming, China, 2002, pp. 1685-1689 vol.3.

[71] Y. Huang, X.Wang, K. Chen, et al., "SSI mechanism simulation validation and practical mitigation strategy of DFIG-based wind farms," in *Power System Technology*, 2016, 40 (8): 2364-2369.

[72] Y. Li, d. shu, F. Shi and z. yan, "A Multi-rate Co-simulation of Combined Phasor-Domain and Time-Domain Models for Large-scale Wind Farms," *2020 IEEE Power & Energy Society General Meeting (PESGM)*, Montreal, QC, Canada, 2020, pp. 1-1.

[73] D. Ning, R. Song, J, Chen, Z. Chen, C. Qin, "Online analysis and early-warning method of subsynchronous resonance based on time-domain simulation," *2015 18th International Conference on Electrical Machines and Systems (ICEMS)*, Pattaya, Thailand, 2015, pp. 2030-2033.

[74] Y. Cheng, S. Huang, J. Rose, V. A. Pappu and J. Conto, "ERCOT subsynchronous resonance topology and frequency scan tool development," *2016 IEEE Power and Energy Society General Meeting (PESGM)*, Boston, MA, USA, 2016, pp. 1-5.

[75] I. B. M. Matsuo, F. Salehi, L. Zhao, Y. Zhou and W. Lee, "Optimized Frequency Scanning of Nonlinear Devices Applied to Subsynchronous Resonance Screening," in *IEEE Transactions on Industry Applications*, vol. 56, no. 3, pp. 2281-2291, May-June 2020.

[76] N. Johansson, L. Ängquist and H. Nee, "A Comparison of Different Frequency Scanning Methods for Study of Subsynchronous Resonance," in *IEEE Transactions on Power Systems*, vol. 26, no. 1, pp. 356-363, Feb. 2011.

[77] M. Elfayoumy and C. G. Moran, "A comprehensive approach for subsynchronous resonance screening analysis using frequency scanning technique," *2003 IEEE Bologna Power Tech Conference Proceedings,*, Bologna, Italy, 2003, pp. 5 pp. Vol.2-.

[78] S. Gupta, A. Moharana and R. K. Varma, "Frequency scanning study of sub-synchronous resonance in power systems," *2013 26th IEEE Canadian Conference on Electrical and Computer Engineering (CCECE)*, Regina, SK, Canada, 2013, pp. 1-6.

[79] Y. Cheng, S. H. Huang and J. Rose, "A Series Capacitor Based Frequency Scan Method for SSR Studies," in *IEEE Transactions on Power Delivery*, vol. 34, no. 6, pp. 2135-2144, Dec. 2019.

[80] Z. Zhang, H. Wang, Z. Wang and G. Ding, "Subsynchronous Oscillation Suppression Measures for Doubly-fed Wind Turbine Based on Eigenvalue Analysis Method and Correlation Factor Method," *2019 6th International Conference on Systems and Informatics (ICSAI)*, Shanghai, China, 2019, pp. 234-238.

[81] L. Yang, Z. Yu, T. Xu, J. He, C. Wang and C. Pang, "Eigenvalue analysis of subsynchronous oscillation in grid-connected PV power stations," *2017 China International Electrical and Energy Conference (CIEEC)*, Beijing, China, 2017, pp. 285-290.

[82] E. H. Allen, J. W. Chapman and M. D. Ilic, "Eigenvalue analysis of the stabilizing effects of feedback linearizing control on subsynchronous resonance," *Proceedings of International Conference on Control Applications*, Albany, NY, USA, 1995, pp. 395-402.

[83] D. Kim, H. Nam and Y. Moon, "A Practical Approach to HVDC System Control for Damping Subsynchronous Oscillation Using the Novel Eigenvalue Analysis Program," in *IEEE Transactions on Power Systems*, vol. 22, no. 4, pp. 1926-1934, Nov. 2007.

[84] Z. Xu and Z. Feng, "A novel unified approach for analysis of small-signal stability of power systems," *2000 IEEE Power Engineering Society Winter Meeting. Conference Proceedings (Cat. No.00CH37077)*, Singapore, 2000, pp. 963-967 vol.2.

[85] D. Kim, Y. Moon and H. Nam, "SSR Small-Signal Stability Analysis Program of Power Systems and its Application to IEEE Benchmark Systems," *2007 IEEE Lausanne Power Tech*, Lausanne, Switzerland, 2007, pp. 161-166.

[86] J. Sun, M. Li, Z. Zhang, T. Xu, J. He, H. Wang, G. Li, "Renewable energy transmission by HVDC across the continent: System challenges and opportunities," in *CSEE Journal of Power and Energy Systems*, vol. 3,no. 4, pp. 353–364, Dec. 2017.

[87] X. Wang, L. Harnefors and F. Blaabjerg, "Unified impedance model of grid-connected voltage-source converters," in *IEEE Transactions on Industrial Electronics*, vol. 33, no. 2, pp. 1775-1787, Feb. 2018.

[88] H. Liu, X. Xie, J. He, T. Xu, Z. Yu, C. Wang, C. Zhang, "Subsynchronous interaction between direc-drive PMSG based wind farms and weak AC networks," in *IEEE Trans. on Power Syst.*, vol. 32, no. 6, pp. 4708–4720, Nov. 2017.

[89] M. Zhao, X. Yuan and J. Hu, "Modeling of DFIG Wind Turbine Based on Internal Voltage Motion Equation in Power Systems Phase-Amplitude Dynamics Analysis," in *IEEE Transactions on Power Systems*, vol. 33, no. 2, pp. 1484-1495, March 2018.

[90] S. Ren, S. Wang, Y. Zhu, Q.X. Wang and X.F. Huang, "A Blocking Filter design method of effective suppression of three forms of SSR," *2016 IEEE PES Asia-Pacific Power and Energy Engineering Conference (APPEEC)*, Xi'an, 2016, pp. 599-603.

[91] X. Xie, P. Liu, K. Bai and Y. Han, "Applying Improved Blocking Filters to the SSR Problem of the Tuoketuo Power System," in *IEEE Transactions on Power Systems*, vol. 28, no. 1, pp. 227-235, Feb. 2013.

[92] X. Dong, X. Wang and Y. Yang, "Suppression of sub-synchronous oscillation caused by HVDC using supplementary excitation damping controller," *2014 17th International Conference on Electrical Machines and Systems (ICEMS)*, Hangzhou, 2014, pp. 2431-2434.

[93] X. Xie, L. Wang and Y. Han, "Combined Application of SEDC and GTSDC for SSR Mitigation and Its Field Tests," in *IEEE Transactions on Power Systems*, vol. 31, no. 1, pp. 769-776, Jan. 2016.

[94] X. Zhao and S. Gao, "Damping subsynchronous oscillation by static VAR compensator," *CICED 2010 Proceedings*, Nanjing, 2010, pp. 1-5.

[95] T. Fei, B. Chen, D. Liu, F. Dong, Y. Yang and L. Yu, "Research of control strategy of SVC on subsynchronous oscillation suppression," *2014 International Symposium on Power Electronics, Electrical Drives, Automation and Motion*, Ischia, 2014, pp. 62-65.

[96] H. Xie and M. M. de Oliveira, "Mitigation of SSR in presence of wind power and series compensation by SVC," *2014 International Conference on Power System Technology*, Chengdu, 2014, pp. 2819-2826.

[97] L. Piyasinghe, Z. Miao, J. Khazaei and L. Fan, "Impedance Model-Based SSR Analysis for TCSC Compensated Type-3 Wind Energy Delivery Systems," in *IEEE Transactions on Sustainable Energy*, vol. 6, no. 1, pp. 179-187, Jan. 2015.

[98] R. K. Varma, Y. Semsedini and S. Auddy, "Mitigation of subsynchronous oscillations in a series compensated wind farm with Thyristor Controlled Series Capacitor (TCSC)," *2007 Power Systems Conference: Advanced Metering, Protection, Control, Communication, and Distributed Resources*, Clemson, SC, 2007, pp. 331-337.

[99] A. D. Falehi and A. Mosallanejad, "Neoteric HANFISC–SSSC based on MOPSO technique aimed at oscillation suppression of interconnected multi-source power systems," in *IET Generation, Transmission & Distribution*, 2016, pp. 1728-1740.

[100] K. Rachananjali, N. Pavani, S.Suman and D. V. S. B. Chaitanya, "Damping of subsynchronous resonance using SSSC with hysteresis current control," *2014 International Conference on Green Computing Communication and Electrical Engineering (ICGCCEE)*, Coimbatore, 2014, pp. 1-5.

[101] R. Thirumalaivasan, M. Janaki and N. Prabhu, "Damping of SSR Using Subsynchronous Current Suppressor With SSSC," in *IEEE Transactions on Power Systems*, vol. 28, no. 1, pp. 64-74, Feb. 2013.

[102] A. Moharana, R. K. Varma and R. Seethapathy, "SSR Alleviation by STATCOM in Induction-Generator-Based Wind Farm Connected to Series Compensated Line," in *IEEE Transactions on Sustainable Energy*, vol. 5, no. 3, pp. 947-957, July 2014.

[103] A. Moharana, R. K. Varma and R. Seethapathy, "SSR mitigation in wind farm connected to series compensated transmission line using STATCOM," *2012 IEEE Power Electronics and Machines in Wind Applications*, Denver, CO, 2012, pp. 1-8.

[104] G. D. Irwin, A. K. Jindal and A. L. Isaacs, "Sub-synchronous control interactions between type 3 wind turbines and series compensated AC transmission systems," *2011 IEEE Power and Energy Society General Meeting*, San Diego, CA, 2011, pp. 1-6.

[105] L. Wang, X. Xie, Q. Jiang and X. Liu, "Centralised solution for subsynchronous control interaction of doubly fed induction generators using voltage-sourced converter," in *IET Generation, Transmission & Distribution*, vol. 9, no. 16, pp. 2751-2759, Aug. 2015.

[106] A. E. Leon and J. A. Solsona, "Sub-Synchronous Interaction Damping Control for DFIG Wind Turbines," in *IEEE Transactions on Power Systems*, vol. 30, no. 1, pp. 419-428, Jan. 2015.

[107] R. K. Varma, S. Auddy and Y. Semsedini, "Mitigation of Subsynchronous Resonance in a Series-Compensated Wind Farm Using FACTS Controllers," in *IEEE Transactions on Power Delivery*, vol. 23, no. 3, pp. 1645-1654, July 2008.

[108] H. A. Mohammadpour and E. Santi, "Sub-synchronous resonance analysis in DFIG-based wind farms: Mitigation methods — TCSC, GCSC, and DFIG controllers — Part II," *2014 IEEE Energy Conversion Congress and Exposition (ECCE)*, Pittsburgh, PA, 2014, pp. 1550-1557.

[109] H. A. Mohammadpour, M. M. Islam, E. Santi and Y. J. Shin, "SSR Damping in Fixed-Speed Wind Farms Using Series FACTS Controllers," in *IEEE Transactions on Power Delivery*, vol. 31, no. 1, pp. 76-86, Feb. 2016.

[110] B.F. Gao, J. Liu, R. Li, S.Q. Zhao, "Studies of Sub-Synchronous Control Interaction in Wind Turbine Generators",*Transactions of China Electrotechnical Society*, vol. 30, no. 16, pp. 154-161, Aug. 2015.

[111] G. D. Irwin, A. Isaacs and D. Woodford, "Simulation requirements for analysis and mitigation of SSCI phenomena in wind farms," *PES T&D 2012, Orlando, FL*, 2012, pp. 1-4.

[112] K. Li, X.Y. L, S. Chen, M. Miao, X. Wang, "Analysis on Feasibility of Damping HVDC-included Subsynchronous Oscillation by Photovaltic Grid-connection," *Electric Power Automation Equipment*, vol. 35, no.3, pp. 41-46, March. 2015.

[113] T. Rauhala and P. Järventausta, "On feasibility of SSDC to improve the effect of HVDC on subsynchronous damping on several lower range torsional oscillation modes," *IEEE PES General Meeting, Minneapolis*, MN, 2010, pp. 1-8.

[114] L. Zhang, L. Harnefors, and H. Nee, "Power-synchronization control of grid-connected voltage-source converters," in *IEEE Transactionson Power Systems*, vol. 25, no. 2, pp. 809–820, May 2010.

[115] M. F. M. Arani and Y. A.-R. I. Mohamed, "Analysis and performance enhancement of vector-controlled VSC in HVDC links connected to very weak grids," in *IEEE Transactions on Power Systems*, vol. 32, no. 1, pp. 684–693, Jan. 2017.

[116] J. Zhou and A. M. Gole, "VSC transmission limitations imposed by AC system strength and AC impedance characteristics," *10th IET International Conferernce on AC and DC Power Transmission (ACDC 2012)*, Dec. 2012, pp. 1–6.

[117] J. Zhou, H. Ding, S. Fan, Y. Zhang, and A. M. Gole, "Impact of short-circuit ratio and phase-locked-loop parameters on the small-signal behavior of a VSC-HVDC converter," in *IEEE Transactions on Power Delivery*, vol. 29, no. 5, pp. 2287–2296, Oct. 2014.

[118] M. Davari and Y. A.-R. I. Mohamed, "Dynamics and robust vector control of a very weak grid-connected voltage-source converter considering the phase locked loop dynamics," in *IEEE Transactions on Power Electronics*, vol. 32, no. 2, pp. 977–994, Feb. 2017.

[119] K. M. Alawasa, Y. A. I. Mohamed, and W. Xu, "Modeling, analysis, and suppression of the impact of full-scale wind-power converters on subsynchronous damping," in *IEEE Syst. J.*, vol. 7, no. 4, pp. 700–712, Dec. 2013.

[120] K. M. Alawasa, Y. A. I. Mohamed, and W. Xu, "Active mitigation of subsynchronous interactions between PWM voltage-source converters and power networks," in *IEEE Trans. Power Electron.*, vol. 29, no. 1, pp. 121–134, Jan. 2014.

[121] L. Harnefors, M. Bongiorno, S. Lundberg, "Input-admittance calculation and shaping for controlled voltage-source converters, " in *IEEE Trans. on Industrial Electronics*, vol. 54, no. 6, pp. 3323-3334, Dec. 2007.

[122] L. Sainz, M. Cheah-Mane, L. Monjo, J. Liang and O. Gomis-Bellmunt, "Positive-Net-Damping Stability Criterion in Grid-Connected VSC Systems," in *IEEE Journal of Emerging and Selected Topics in Power Electronics*, vol. 5, no. 4, pp. 1499-1512, Dec. 2017.

[123] D. G. Holmes, T. A. Lipo, B. P. McGrath and W. Y. Kong, "Optimized Design of Stationary Frame Three Phase AC Current Regulators," in *IEEE Transactions on Power Electronics*, vol. 24, no. 11, pp. 2417-2426, Nov. 2009.

[124] L. Dong, J. Kong, J. Feng and Y. Zhang, "Subsynchronous Resonance Mitigation for Series Compensation Transmission System of DFIG Based on PR Control," *2019 IEEE 10th International Symposium on Power Electronics for Distributed Generation Systems (PEDG)*, Xi'an, China, 2019, pp. 734-738.

[125] C. Zhang, X. Cai, Z. Li , "Stability Criterion and Mechanisms Analysis of Electrical Oscillations in the Grid-tied VSC System," in *CSEE Journal of Power and Energy Systems*, vol. 42,no. 9, pp. 2768–2777, July. 2018.

[126] J. Lyu, X. Cai and M. Molinas, "Frequency Domain Stability Analysis of MMC-Based HVdc for Wind Farm Integration," in *IEEE Journal of Emerging and Selected Topics in Power Electronics*, vol. 4, no. 1, pp. 141-151, March 2016.

[127] J. Lyu and X. Cai, "Impact of controller parameters on stability of MMC-based HVDC systems for offshore wind farms," *International Conference on Renewable Power Generation (RPG 2015)*, Beijing, 2015, pp. 1-6.

[128] L. Harnefors, "Modeling of Three-Phase Dynamic Systems Using Complex Transfer Functions and Transfer Matrices," in *IEEE Transactions on Industrial Electronics*, vol. 54, no. 4, pp. 2239-2248, Aug. 2007.

Appendix A

The deductions of $T_{abc\text{-}dq}$ and $T_{dq\text{-}abc}$ are shown as follows:

$$\mathbf{T}_{\mathrm{abc}-\alpha\beta} = \frac{2}{3}\begin{bmatrix} 1 & -\frac{1}{2} & -\frac{1}{2} \\ 0 & \frac{\sqrt{3}}{2} & -\frac{\sqrt{3}}{2} \end{bmatrix} \tag{A-1}$$

$$\mathbf{T}_{\alpha\beta-\mathrm{dq}} = \begin{bmatrix} \cos\theta_{\mathrm{pll}} & \sin\theta_{\mathrm{pll}} \\ -\sin\theta_{\mathrm{pll}} & \cos\theta_{\mathrm{pll}} \end{bmatrix} \tag{A-2}$$

$$\mathbf{T}_{\mathrm{abc}-\mathrm{dq}} = \mathbf{T}_{\alpha\beta-\mathrm{dq}}\mathbf{T}_{\mathrm{abc}-\alpha\beta} = \frac{2}{3}\begin{bmatrix} \cos\theta_{\mathrm{pll}} & \cos\left(\theta_{\mathrm{pll}}-\frac{2\pi}{3}\right) & \cos\left(\theta_{\mathrm{pll}}+\frac{2\pi}{3}\right) \\ -\sin\theta_{\mathrm{pll}} & -\sin\left(\theta_{\mathrm{pll}}-\frac{2\pi}{3}\right) & -\sin\left(\theta_{\mathrm{pll}}+\frac{2\pi}{3}\right) \\ \frac{1}{2} & \frac{1}{2} & \frac{1}{2} \end{bmatrix} \tag{A-3}$$

$$\mathbf{T}_{\mathrm{abc}-\mathrm{dq}}^{-1} = \mathbf{T}_{\mathrm{abc}-\mathrm{dq}}^{\mathrm{T}} = \begin{bmatrix} \cos\theta_{\mathrm{pll}} & -\sin\theta_{\mathrm{pll}} & 1 \\ \cos\left(\theta_{\mathrm{pll}}-\frac{2\pi}{3}\right) & -\sin\left(\theta_{\mathrm{pll}}-\frac{2\pi}{3}\right) & 1 \\ \cos\left(\theta_{\mathrm{pll}}+\frac{2\pi}{3}\right) & -\sin\left(\theta_{\mathrm{pll}}+\frac{2\pi}{3}\right) & 1 \end{bmatrix} \tag{A-4}$$

Appendix B

The parameters of the example system utilised in Chapter 3 and Chapter 4 are shown in Tables B-1 and B-2.

Table B-1. Parameters of the lines and transformers in Chapter 3 and Chapter 4

Parameter	Value(pu)	Parameter	Value(pu)
r_{L1}	0.02	r_{L2}	0.05
x_{L1}	0.12	x_{L2}	0.65
x_{L3}	0.08	x_{T1}	0.06
x_{T2}	0.07	x_{T3}	0.15

Table B-2. 1.5 MW WTG Parameters (50 Hz base frequency)

	Parameters	Values
VSC input voltage	v_{sd0} (pu)	1
WTG output active power	P_{WTG} (pu)	0.1
Rated power of one WTG	$P_{WTG, rated}$ (MW)	1.5
Output L-filter	R_f, L_f (pu)	0.015,0.15
DC Capacitance	C (pu)	13
Current controller (CC) ($k_{p\_cc} = \omega_{cc} L_f$, $k_{i\_cc} = \omega_{cc} R_f$)	f_b (pu)	50
	$\omega_{cc, ref}$ (pu)	3.4
	$\omega_{f, ref}$ (pu)	0.34
DC-link voltage controller (DVC) ($k_{p\_dc} = \omega_{dc} C$, $k_{i\_dc} = k_{p\_dc}/25$)	$\omega_{dc, ref}$ (pu)	0.68
Phase-locked loop (PLL) ($k_{p\_pll} = \omega_{pll}/v_{sd0}$, $k_{i\_pll} = k_{p\_pll}/10$)	$\omega_{pll, ref}$ (pu)	0.25

The symblols in single VSC connected systems in Chapter 3 and Chapter 4 are shown in Table B-3.

Table B-3. Symblols in single VSC connected systems in Chapter 3 and Chapter 4

Symbols	Meaning
i_{cd}，i_{cq}	d-and q-axis component of VSC output current
v_{sd}，v_{sq}	d-and q-axis component of VSC output voltage
i_{cdr}，i_{cqr}	Reference values of i_{sd}，i_{sq}
v_{gd}，v_{gq}	d-and q-axis component of the grid output voltage
v_{dc}，v_{dcr}	DC voltage and its reference value
P_{WTG}	WTG output active power
k_{p_cc} / k_{p_dc} / k_{p_pll}	Proportional gains of inner current control loop, outer control loop and PLL
k_{p_cc} / k_{p_dc} / k_{p_pll}	Integral gains of inner current control loop, outer control loop and PLL
ω_f, ω_{cc}, ω_{dc}, ω_{pll}	Bandwidths of feed-forward voltage low-pass filter, current loop, outer loop and PLL

The parameters of the example system utilised in Chapter 5 are shown in Table B-4.

Table B-4. Parameters of the lines and transformers in Chapter 5

Parameter	Value(pu)	Parameter	Value(pu)
R_g	0.008	X_g	0.08
R_1	0.05	X_1	0.65
X_{T1}	0.15	X_{T2}	0.07
R_2	0.02	X_2	0.12
R_{v1}	0.015	X_{v1}	0.15
R_{v2}	0.015	X_{v2}	0.15
X_{T3}	0.06	X_{T4}	0.06

The symblols in multiple VSCs connected systems in Chapter 5 are shown in Table 5.

Table B-5. Symbols in multiple VSCs connected systems in Chapter 5

Symbols	Meaning
i_{cd1}，i_{cq1}	d-and q-axis component of VSC1 output current
v_{cdr1}，v_{cqr1}	Reference values of d-and q-axis component of VSC1 output voltage
i_{cdr1}，i_{cqr1}	Reference values of i_{sd}，i_{sq}
v_{dc1}，v_{dcr1}	DC voltage and its reference value in WTG1

P_{WTG1}	WTG1 output active power
i_{cd2}，i_{cq2}	*d*-and *q*-axis component of VSC2 output current
v_{cdr2}，v_{cqr2}	Reference values of *d*-and *q*-axis component of VSC1 output voltage
v_{gd}，v_{gq}	*d*-and *q*-axis component of the grid output voltage
v_{dc2}，v_{dcr2}	DC voltage and its reference value in WTG2
P_{WTG2}	WTG2 output active power
ω_{f1}, ω_{cc1}, ω_{dc1}, ω_{pll1}	Bandwidths of feed-forward voltage low-pass filter, current loop, outer loop and PLL of VSC1
ω_{f2}, ω_{cc2}, ω_{dc2}, ω_{pll2}	Bandwidths of feed-forward voltage low-pass filter, current loop, outer loop and PLL of VSC2

Appendix C

The MATLAB code of the stability analysis in Chapter 4 is shown as follows:

```
function SSO

close all

clc

N = 600;

fb = 50;
wb = 2*pi*fb;

Ubac = 620;
Ubdc = 2*Ubac;
Sb_red = 1500e6;
Ib_red = Sb_red/Ubac;
Zb_red = Ubac^2/Sb_red;
Sb = 1.5e6;
Ib = Sb/Ubac;
Zb = Ubac^2/Sb;
Zbdc = Ubdc^2/Sb;

s=tf('s'); % Definition of the Laplace space variable
FX = 1.0; % Parameter to fix SCR

Zgrid = FX*(0.02+0.05 + (s/wb)*(0.12+0.65+0.08+0.06/N+0.07+0.15));

Zgrid_dq = FX*(wb/wb)*(0.12+0.65+0.08+0.06/N+0.07+0.15);

SCR = (1500e6/(FX*(0.12+0.65+0.08+0.06/N+0.07+0.15)))/(N*1.5e6)

Cte_R = 10;
Lf_pu = 0.15;
Rf_pu = Lf_pu/Cte_R;
Lf = Lf_pu*Zb/wb;
Rf = Rf_pu*Zb;


Cdc = 40e-3;
Cdc_pu = Cdc*(Zbdc*wb)

%
% Definition of power from DC to AC
%
Po_pu = 0.1;
Po = Po_pu*Sb;  % WTGs supplying 10% of their rated power
%
%
Vg_pu = 1.0;  Vg = Vg_pu*Ubac;
%
% Steady state calculation
```

```
%
Rg_pu = FX*(0.02+0.05);
Xg_pu=FX*(0.12+0.65+0.08+0.06/N+0.07+0.15);
Po_puT = Po_pu*1.5e6*N/1500e6

if ((2*Po_puT*sqrt(Rg_pu^2+Xg_pu^2))/(Vg_pu^2+2*Po_puT*Rg_pu) < 1)
    Eo_pu = sqrt((Vg_pu^2+2*Po_puT*Rg_pu +
sqrt((Vg_pu^2+2*Po_puT*Rg_pu)^2 - 4*(Rg_pu^2+Xg_pu^2)*Po_puT^2))/2)
    Eo = Eo_pu*Ubac;
    delta = asin(Po_puT*Xg_pu/(Vg_pu*Eo_pu)) % Condition:
Po_puT*Xg_pu/(Vg_pu*Eo_pu) < 1 (if never reach to 90)
    delta_gr=delta*180/pi
    IdoT_c_pu = -Po_puT/Eo_pu;  IdoT_c = IdoT_c_pu*Ib_red
    Ido_c_pu = -Po_pu/Eo_pu;  Ido_c = Ido_c_pu*Ib
    Iqo_c_pu = 0;  Iqo_c = Iqo_c_pu*Ib;
else
    display('Too much power demanded. Total power limit and WT power
limit')
    display('Exact value:')
    Pot_pu_Lim = (4*Vg_pu^2*Rg_pu +
4*Vg_pu^2*sqrt(Rg_pu^2+Xg_pu^2))/(8*Xg_pu^2);
    Po_pu_Lim = [Pot_pu_Lim Pot_pu_Lim*1500e6/(N*1.5e6)]
    display('Approximated value:')
    Pot_pu_Lim_apr = Vg_pu^2/(2*Xg_pu);
    Po_pu_Lim_apr = [Pot_pu_Lim_apr Pot_pu_Lim_apr*1500e6/(N*1.5e6)]
    display('Voltage value with power limit [Exact Approximated]:')
    EoLim_pu = sqrt((Vg_pu^2+2*Pot_pu_Lim*Rg_pu +
sqrt((Vg_pu^2+2*Pot_pu_Lim*Rg_pu)^2 -
4*(Rg_pu^2+Xg_pu^2)*Pot_pu_Lim^2))/2);
    EoLim_aprox_pu = sqrt((Vg_pu^2 + sqrt((Vg_pu^2)^2 -
4*(Pot_pu_Lim_apr*Xg_pu)^2))/2);
    Eo_pu_Lim = [EoLim_pu EoLim_aprox_pu]
    return
end

Qo_pu = 0.0;
Vdc_pu = 1; Vdc = Vdc_pu*Ubdc;

alfac_pu = 3.38; alfac = alfac_pu*wb; % CC bandwidth
%
% Feed-forward filter Hf bandwidth
%
incrHf = 1;
alfaf = incrHf*0.1*alfac; % Bandwidth of the grid voltage feedforward
low pass filter
alfap = 0.075*alfac; % Bandwidth of the outer PLL control
alfad = 0.234*alfac; % Bandwidth of the outer direct voltage control
%
% Inner current control
%
incrCC = 1;
Kp = incrCC*alfac*Lf;
Ki = incrCC*alfac*Rf;
FPI = Kp + Ki/s; % Inner current control

%
% Outer direct voltage control (Vdc).
%
incrDVC = 1;
Kpdc = incrDVC*10;
```

```
Kidc = Kpdc/25
Kpdc_pu = Kpdc*Zbdc;
Kidc_pu = Kidc*Zbdc/wb;
Fdc = Kpdc + Kidc/s; % Outer direct voltage control
%
% Outer PLL control.
%
incrPLL = 1;
KpPLL = incrPLL*alfap/Vg;
KiPLL = KpPLL/10
FPLL = KpPLL + KiPLL/s; % Outer PLL control
GPLL = minreal(FPLL/(s + Eo*FPLL)); % Outer PLL control [GPLL1 =
(alfap/Eo)/(s + alfap)]


Zf = Rf+Lf*s+1j*wb*Lf;
D=1; %D = exp(-Td*s); Time delay
Hf = alfaf/(s+alfaf); % Grid voltage feedforward low pass filter
%
% Current control expressions
%
gcc = (D*FPI)/(Zf+D*(FPI-1j*wb*Lf));
Ycc = ((1-D*Hf)/(Zf+D*(FPI-1j*wb*Lf)));

Gdc_d = -(Ycc*Eo^2 - Po)*Fdc/(Eo*(s*Cdc*Vdc + Eo*gcc*Fdc)); % Control
Vdc (power from DC to AC)
Gdc_q = Iqo_c*Fdc/(Eo*(s*Cdc*Vdc + Eo*gcc*Fdc)); % Control Vdc (power
from DC to AC)

Yvsc_dd_ve = ss(Ycc + gcc*Gdc_d);
Yvsc_dd_ve = minreal(Yvsc_dd_ve);
Yvsc_dq_ve = ss((1 - Eo*GPLL)*gcc*Gdc_q - Iqo_c*GPLL);
Yvsc_dq_ve = minreal(Yvsc_dq_ve);
Yvsc_qq_ve = ss(Ycc*(1 - Eo*GPLL) + Ido_c*GPLL);
Yvsc_qq_ve = minreal(Yvsc_qq_ve);

%
% Study with matrix
%
YvscM_ve = minreal([Yvsc_dd_ve Yvsc_dq_ve; 0 Yvsc_qq_ve]);
ZvscM_ve = (1/YvscM_ve)*1500/(N*1.5)/Zb;
ZgridM_ve = ss([Zgrid -Zgrid_dq; Zgrid_dq Zgrid]);
ZtM_ve = ZgridM_ve + ZvscM_ve;
%
% Determinant study
%
aux_ve = minreal(1/(ZtM_ve(1,1)*ZtM_ve(2,2) -
ZtM_ve(1,2)*ZtM_ve(2,1)));
Det_ZtM_ve = 1/aux_ve;
Det_ZtM = tf(Det_ZtM_ve);

[Zcc,Pcc,K] = zpkdata(Det_ZtM);
Zcc{1}

% Pcc{1}
% G = zpk(Zcc, Pcc, K)

%%%%%%%%%%%%%%%%%%%%%%%%%%%%%%%%%%%%%%%%%%%%%%%%%%%%%
%
% Frequency study
```

```
%
%%%%%%%%%%%%%%%

f_pu = [5:0.01:45]/50;
s_pu = 1i*f_pu; % wpu = fpu
s = s_pu*wb;


Zgrid = FactX*(0.02+0.05 + (s/wb)*(0.12+0.65+0.08+0.06/N+0.07+0.15));
Zgrid_dq = FactX*(wb/wb)*(0.12+0.65+0.08+0.06/N+0.07+0.15);

FPI = Kp + Ki./s; % Inner current control
Fdc = Kpdc + Kidc./s; % Outer direct voltage control

FPLL = KpPLL + KiPLL./s; % Outer PLL control
GPLL = FPLL./(s + Eo*FPLL); % Outer PLL control [GPLL1 = (alfap/Eo)/(s
+ alfap)]

Zf = Rf + Lf*s + 1j*wb*Lf;

D=1; % Time delay D = exp(-Td*s)
Hf = alfaf./(s + alfaf); % Grid voltage feedforward low pas filter
Hdc = alfad./(s + alfad); % Power low pass filter

gcc = (D.*FPI)./(Zf+D.*(FPI-1j*wb*Lf));
Ycc = ((1-D.*Hf)./(Zf+D.*(FPI-1j*wb*Lf)));

Gdc_d = -(Ycc*Eo^2 - Po).*Fdc./(Eo*(s*Cdc*Vdc + Eo*gcc.*Fdc)); % %
Control Vdc (power from DC to AC)
Gdc_q = Iqo_c*Fdc./(Eo*(s*Cdc*Vdc + Eo*gcc.*Fdc)); % Control Vdc
(power from DC to AC)

Yvsc_dd = Ycc + gcc.*Gdc_d;
Yvsc_dq = (1 - Eo*GPLL).*gcc.*Gdc_q - Iqo_c*GPLL;
Yvsc_qq = Ycc.*(1 - Eo.*GPLL) + Ido_c*GPLL;

%
% Matrix calculations
%
for k = 1:length(s)
%
% Harnefors expressions
%
    YvscM = [Yvsc_dd(k) Yvsc_dq(k); 0 Yvsc_qq(k)];
    ZpmsgM = (eye(2)/YvscM)*1500/(N*1.5)/Zb;
    Zpmsg_dd(k) = ZpmsgM(1,1);
    Zpmsg_qq(k) = ZpmsgM(2,2);
    ZgridM = [Zgrid(k) -Zgrid_dq; Zgrid_dq Zgrid(k)];
    ZtM = ZgridM + ZpmsgM;
%
% Eigenvalues of inv(ZpmsgM)*ZgridM
%
    Ls = inv(ZpmsgM)*ZgridM;

    Ls11(k) = Ls(1,1);
    Ls21(k) = Ls(2,1);
    Ls12(k) = Ls(1,2);
    Ls22(k) = Ls(2,2);
    vaps(k,:) = eig(Ls);
```

```
    vaps2b = (Ls(1,1)+Ls(2,2))/2 + sqrt( ((Ls(1,1)-Ls(2,2))/2)^2 +
Ls(1,2)*Ls(2,1) );
    vaps2a = (Ls(1,1)+Ls(2,2))/2 - sqrt( ((Ls(1,1)-Ls(2,2))/2)^2 +
Ls(1,2)*Ls(2,1) );
    vaps2(k,:) = [vaps2a; vaps2b];

    DetZtM(k) = det(ZtM);
end

f_pu = f_pu*fb;

figure(1)
subplot(2,1,1),
plot(f_pu, real(DetZtM), 'b')
hold on
plot([f_pu(1) f_pu(end)], [0 0], '--c')
subplot(2,1,2),
plot(f_pu, imag(DetZtM), 'r')
hold on
plot([f_pu(1) f_pu(end)], [0 0], '--c')

figure(2)
plot(f_pu, real(Zgrid+Zpmsg_dd).*real(Zgrid+Zpmsg_qq)-
imag(Zgrid+Zpmsg_dd).*imag(Zgrid+Zpmsg_qq), 'b')
hold on
plot(f_pu, -Zgrid_dq.^2, 'r')
plot([f_pu(1) f_pu(end)], [0 0], '--c')

figure(3)
plot(real(vaps2(:,1)),imag(vaps(:,1)), 'r','LineWidth',2)
hold on
plot(real(vaps2(:,2)),imag(vaps(:,2)), 'b','LineWidth',3)
plot(real(vaps2(1,1)),imag(vaps(1,1)), 'ro','LineWidth',3)
plot(real(vaps2(1,2)),imag(vaps(1,2)), 'bo','LineWidth',3)
plot(cos(2*pi*f_pu),sin(2*pi*f_pu), '--g')


figure(6)
subplot(2,1,1),
plot(f_pu, real(Zgrid+Zpmsg_dd).*real(Zgrid+Zpmsg_qq), 'b')
hold on
xlim([15 45])
subplot(2,1,2),
plot(f_pu, imag(Zgrid+Zpmsg_dd).*imag(Zgrid+Zpmsg_qq), 'b')
hold on
xlim([15 45])

figure(8)
subplot(2,2,2),
plot(f_pu, real(Zpmsg_dd), 'r', f_pu, real(Zpmsg_qq), 'k')
hold on
xlim([15 45])
subplot(2,2,4),
plot(f_pu, imag(Zpmsg_dd), 'r', f_pu, imag(Zpmsg_qq), 'k')
hold on
xlim([15 45])
subplot(2,2,1),
plot(f_pu, real(Zgrid+Zpmsg_dd).*real(Zgrid+Zpmsg_qq), 'b')
hold on
xlim([15 45])
```

```
subplot(2,2,3),
plot(f_pu, imag(Zgrid+Zpmsg_dd).*imag(Zgrid+Zpmsg_qq), 'b')
hold on
xlim([15 45])
figure(9)

XR2=real(ans);YI2=imag(ans)./(2*pi);
% subplot(1,2,2);
plot(XR2,YI2,'kx');grid on;hold on;
save_XR2(:,i)=XR2;
save_YI2(:,i)=YI2;
end
```

Appendix D

The deductions of the block diagram of the studied system in Chapter 3 and Chapter 4 as well as the bandwidth of feed-forward voltage low-pass filter, current loop, outer loop and PLL of the VSCs are presented as follows:

1) Inner control loop

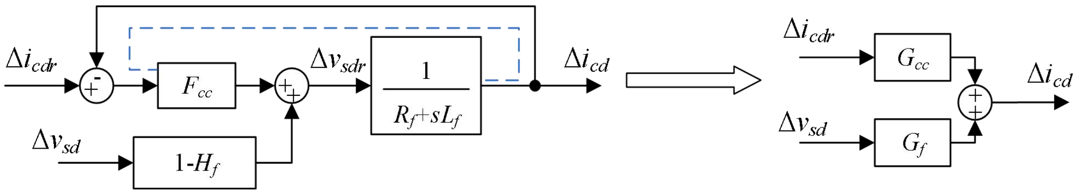

Fig. D.1. Small-signal model block diagram of inner loop d-axis control of the VSC.

Fig. D.1 shows the block diagram of the inner loop d-axis control of the VSC. The equations of the output AC voltage v_s in the inner current control loop (CC) can be expressed with complex transfer functions

$$\boldsymbol{i}_{\mathrm{c}} = \underbrace{\frac{F_{cc}(s)}{R_f+L_fs+F_{cc}(s)}}_{G_{cc}(s)}\boldsymbol{i}_{cr} + \underbrace{\frac{1-H_f(s)}{R_f+L_fs+F_{cc}(s)}}_{G_f(s)}\boldsymbol{v}_s \tag{D-1}$$

where

$$G_{cc}(s) = \frac{k_{p\_cc}+k_{i\_cc}/s}{L_fs+R_f+k_{p\_cc}+k_{i\_cc}/s} \approx \frac{k_{p\_cc}}{L_fs+k_{p\_cc}} = \frac{k_{p\_cc}/L_f}{s+k_{p\_cc}/L_f} = \frac{\omega_{cc}}{s+\omega_{cc}} \tag{D-2}$$

$$\begin{aligned} G_f(s) &= \frac{s(1-H_f(s))}{L_fs^2+(R_f+k_{p\_cc})s+k_{i\_cc}} = \frac{s^2}{(L_fs^2+(R_f+k_{p\_cc})s+k_{i\_cc})(s+\omega_f)} \\ &\approx \frac{s}{(L_fs+k_{p\_cc})(s+\omega_f)} = \frac{s}{L_f(s+\omega_{cc})(s+\omega_f)} \end{aligned} \tag{D-3}$$

In the base case in Chapter 4, $k_{i\_cc} / k_{p\_cc} = R_f/L_f$, since $R_f << L_f$, so $k_{i\_cc}/s << k_{p\_cc}$ in the SSI frequency range, and $\omega_{cc} \approx k_{p\_cc}/L_f$.

2) Outer control loop

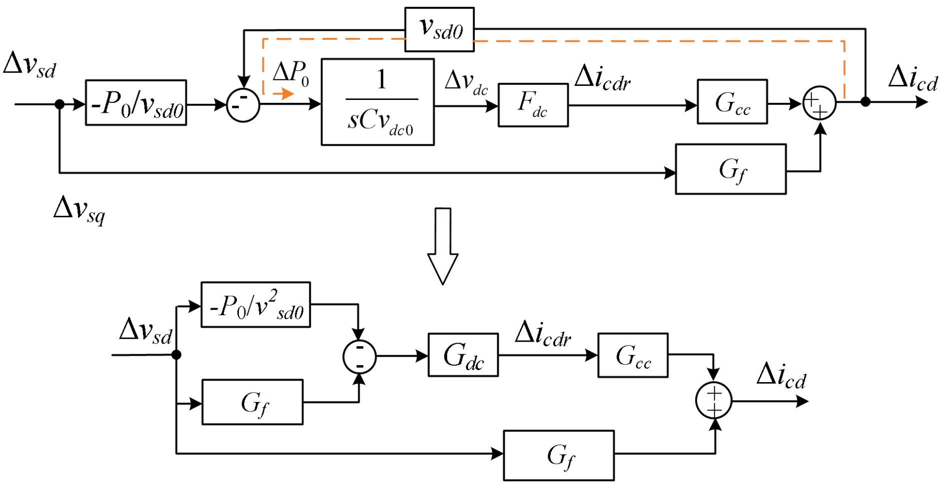

Fig. D.2. Small-signal model block diagram of outer loop control of the VSC.

The block diagram of the VSC outer loop control is shown in Fig. D.2. When considering the outer loop as well, the models of the outer loop and the power flows in the AC grid are

$$\begin{aligned} i_{cdr} &= F_{dc}(s)(v_{dcr} - v_{dc}) \\ P_s &= P_L - \left(\frac{C}{2}\frac{dv_{dc}{}^2{}_s}{dt}\right) \\ P_g &=- (v_{sd}i_{cd} + v_{sq}i_{cq}) \end{aligned} \tag{D-4}$$

where C is the DC capacitance. The variables P_s and P_g are the steady-state operation points of DC output power and the power of the AC transmission line. And the small-signal models of the models above can be expressed as:

$$\begin{aligned} &\Delta i_{cdr} =- F_{dc}(s)\Delta v_{dc} \\ &\Delta i_{cqr} = 0 \\ &\Delta P_s =- sCv_{dc0}\Delta v_{dc} \\ &\Delta P_g =- (v_{sd0}\Delta i_{cd} + i_{sd0}\Delta v_{sd} + v_{sq0}\Delta i_{cq} + i_{cq0}\Delta v_{sq}) \end{aligned} \tag{D-5}$$

From (D-5), (D-6) can be derived as

$$\begin{aligned} &\Delta v_{dc} = \frac{v_{sd0}G_f(s)+i_{cd0}}{sCv_{dc0}+v_{sd0}G_{cc}(s)F_{dc}(s)}\Delta v_{sd} \\ &\Rightarrow \ \Delta i_{cdr} =- F_{dc}(s)\Delta v_{dc} =- \underbrace{\frac{F_{dc}(s)(v_{sd0}G_f(s)+i_{cd0})}{sCv_{dc0}+v_{sd0}G_{cc}(s)F_{dc}(s)}}_{G_{dc}(s)}\Delta v_{sd} \end{aligned} \tag{D-6}$$

where

$$\begin{aligned} G_{dc}(s) &= \frac{(k_{p\_dc}s+k_{i\_dc})v_{sd0}}{s^2Cv_{dc0}+v_{sd0}G_{cc}(s)(k_{p\_dc}s+k_{i\_dc})} \approx \frac{k_{p\_dc}v_{sd0}}{sCv_{dc0}+k_{p\_dc}v_{sd0}G_{cc}(s)} \\ &= \frac{k_{p\_dc}v_{sd0}/Cv_{dc0}}{s+k_{p_{dc}}v_{sd0}G_{cc}(s)/Cv_{dc0}} = \frac{\omega_{dc}}{s+\omega_{dc}G_{cc}(s)} \end{aligned} \tag{D-7}$$

In the base case in Chapter 4, k_{i_dc} / k_{p_dc} =25, since $R_f << L_f$, so $k_{i\_dc} /s << k_{p\_dc}$ in the SSI frequency range, and $\omega_{dc} \approx k_{p\_dc}\, v_{sd0}/C\, v_{dc0}$.

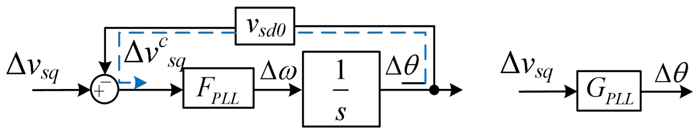

Fig. D.3. Small-signal model block diagram of PLL of the VSC.

The block diagram of the VSC outer loop control is shown in Fig. D.3. The transfer function of PLL can be expressed as

$$\begin{aligned} G_{pll}(s) &= \frac{k_{p\_pll}+k_{i\_pll}/s}{s+v_{sd0}(k_{p\_pll}+k_{i\_pll}/s} \approx \frac{k_{p\_pll}}{s+v_{sd0}k_{p\_pll}} \\ &= \frac{v_{sd0}k_{p\_pll}}{v_{sd0}(s+v_{sd0}k_{p\_pll})} = \frac{\omega_{pll}}{v_{sd0}(s+\omega_{pll})} \end{aligned} \tag{D-8}$$

In the base case in Chapter 4, $k_{i\_pll} / k_{p\_pll} = R_f/L_f$, since $R_f << L_f$, so $k_{i\_pll}/s << k_{p\_pll}$ in the SSI frequency range, and $\omega_{pll} \approx v_{sd0}k_{p\_pll}$.